HOLOGRAPHIC IN-SITU STRESS MEASUREMENT IN GEOPHYSICS

Thesis by

Stephen Norfleet Cohn

In Partial Fulfillment of the Requirements

for the Degree of

Doctor of Philsophy

California Institute of Technology

Pasadena, California

1983

(Submitted September 28, 1982)

ACKNOWLEDGEMENTS

With pleasure I thank the faculty, students and staff of the Seismological Laboratory and the Division of Geological and Planetary Sciences for sharing their insight, knowledge, and company with me during my years as a graduate student. I am particularly grateful to Tom Ahrens, who provided me with the opportunity to work on the holographic stressmeter and then supervised and supported my efforts, and to Clarence Allen, Don Helmberger, Kerry Sieh, and Lee Silver whose stimulating instruction and ideas in other areas helped broaden my interests.

Many individuals helped me during the course of this project. I thank Bill Barber, Mott Hudson, Elmer Steffanson, and Dick Wickes for their help in designing and fabricating components for the stressmeter, Papo Gelle and Mike Long for patience and a wide range of technical assistance, and Lt. Cmdr. Clevin, Richard Carlson, and Joe Lacomb, who made our experimental deployment at the Nevada Test Site possible. I am also very grateful to Warren Ginn who worked especially hard in the final stages of the project and was instrumental in orchestrating our borehole trials of the stressmeter.

This research was supported by the National Science Foundation in grant Nos. EAR77-23179 and EAR79-19740.

ABSTRACT

A new and still experimental method for measuring the absolute in-situ stress field in crustal rocks offers several advantages compared to existing in-situ stress measurement techniques. It employs optical holography to record strain-relief displacements in a borehole environment. We call the prototype instrument the holographic stressmeter. It operates in an uncased borehole where it drills strain-relieving side holes into the borehole wall. An interference holographic recording system records the resulting displacements onto film. The reconstructed interference holograms contain sufficient information in their fringe patterns to determine the three-dimensional vector displacements due to strain relief at every point surrounding the side hole. Assuming isotropic, homogeneous, linearly elastic rock, these displacements define the three stresses acting at the borehole wall at a single point. The three non-vanishing stresses acting at each of three points, distributed azimuthally, on the borehole wall provide sufficient constraint to determine all six components of the desired far-field or virgin-rock stress tensor.

The holographic stressmeter employs an on-board side hole drilling system to produce strain relief. Thus it should be economical to operate and it is not restricted to shallow depths as are overcoring techniques. Furthermore, recording the whole displacement field resulting from drilling the side hole reduces the potential

contamination of the measurement by residual stress mechanisms which often affect point strain measurements using foil resistance gauges.

To date a complete stress determination in the field has not been attempted. However, a prototype stressmeter has demonstrated repeatedly that the stability necessary to conduct the measurment using this approach is attainable. Results from field deployment show that the stressmeter can make qualitatively correct measurements at one azimuth in a borehole. Modifications to make measurements at the three azimuths required for a complete determination of the stress tensor components should be easily achieved. We propose additional improvements to permit measuring rock elastic properties in situ to enable accurate, quantitative stress determinations. The theoretically predicted precision of the stress component magnitudes using this measurement approach is estimated at 20%.

TABLE OF CONTENTS

CHAPTER 1

In-Situ Stress Measurement: Motivations and Techniques

Introduction

This thesis reports on the development of a new instrument for measuring in-situ stress which we call the holographic stressmeter. In theory, this technique determines all six independent values required to define the stress tensor and furthermore it is free of many of the limitations which constrain existing stress-measurement methods.

A prototype holographic stressmeter, which operates in a borehole drilled into virgin rock, has been designed, constructed, and deployed in the field. To date, this prototype has not successfully achieved a complete measurement of the state of stress in rock. Nevertheless, with this prototype I have demonstrated that the measurement approach can be realized in a field-viable instrument. Furthermore, laboratory control experiments show that the measurements made in the field reflect the in-situ stress state rather than misunderstood failures of the stress measuring technique to perform according to the underlying theory. Thus I believe this instrument promises to evolve into a beneficial tool for measuring in-situ stress, recognizing, however, that appreciable developments still separate the current prototype from that goal.

We seek to measure the state of stress in crustal rock for a wide range of purposes classifiable into two areas. On the one hand, faced

by evidence of tectonic activity including earthquakes, plate motions, mountain building, etcetera, which are obviously driven by stresses even if the origin of those stresses is poorly understood, we conclude that knowledge of the stresses would help to explain and perhaps even to predict the occurrence of some of those processes. On the other hand, as we exploit the resources lodged within the earth's crust we dig, tunnel, and drill many kilometers into rock which is stressed. Frequently, this stress seriously constrains how man-made excavations may be achieved efficiently and safely, making prior knowledge of the in-situ stress state essential.

Numerous techniques have been invented to measure stress in crustal rocks. All were developed for or resulted as a byproduct of mining and drilling associated with exploitation of natural resources. Stress, by its very nature is a difficult quantity to measure in a solid. It can only be measured directly at a surface, but simply creating a surface disturbs the virgin state. None of the existing techniques for measuring stress in-situ in rocks combines all of the desirable features one would select given the choice. Each offers characteristic assets coupled with intrinsic limitations. Six components define the stress field. Each stress measuring approach yields measurements related to at least some of these components. The various limitations include expense, maximum operating distance from the surface, requirements for auxiliary information, and ambiguity in interpretation. We present here the results of our search for a better method to measure in-situ stress.

This chapter provides a background on the motivations for measuring

in-situ stress and a brief summary of the existing techniques for doing so. The ensuing three chapters discuss respectively, the underlying elastic problem and its solution, the theory behind and physical realization of the prototype holographic stressmeter, and experimental deployments in the field and associated interpretation of the resulting data which demonstrates that the instrument successfully measures stress.

Motives for Measuring In-Situ Stress

The stress field in crustal rocks consists of several superimposed components. At sites where in-situ stress measurements can be conducted the principal components contributing to the stress field are as follows:

1. Tectonic stress is the stress producing or resulting from current tectonic deformation. Locally it reflects equilibrium adjustments within coherent structural elements of the crust to loads and tractions on their boundaries.

2. Local stress fields originate from several mechanisms, all applicable and relevant on a local scale, but independent of the tectonic stress. These include: gravitational stress, due to the weight of overlying rock, perturbed by existing topography; thermal stress resulting from differential thermal expansion in regions of thermal gradients or possibly large scale variation in coefficients of thermal expansion; and stress perturbations resulting from loading or unloading of local surfaces by natural or man-made events, such as

glaciation, mining, or impounding a reservoir.

3. Residual stress encompasses any stress remaining in rock when all of the bounding surfaces are freed of loads and tractions (Friedman, 1972). Residual stresses are entirely self-equilibrated (i.e. they are balanced along any surface area through the rock, whether or not it is a free surface, as long as the area is larger than the characteristic dimensions of the residual stresses), and can develop on many different scales ranging from microscopic to tens of meters. They can form by thermal mechanisms, thermodynamic phase changes, including weathering, or from a change in the ambient in-situ stress state when structural elements of the rock are characterized by differing elastic properties.

This categorization is not unique (e.g. Pincus et al., 1982), but it yields a division of the contributing components which corresponds to the applications of in-situ stress measurements. However, separating these components when, for example, only one is desired while two or possibly all three may have contributed to the values measured, is often possible only by introducing other geophysical observations (Ranalli, 1975), and even then irresolvable ambiguities may persist. Despite the difficulty isolating these components of stress, in-situ stress measurements are employed widely in geological engineering and tectonics modelling efforts. Local stress fields are studied by engineers in the course of designing and constructing dams, tunnels and mines. The tectonic stress interests geologists and geophysicists endeavoring to explain plate-tectonic motions, as failure to explain the driving mechanism persists as a major unachieved objective in developing the

theory of plate tectonics.

Attempting to model plate motions using a variety of plate-driving mechanisms Richardson et al. (1976), Solomon et al. (1980), and Hager and O'Connell (1981) each conclude that calculated mid-plate tectonic stresses reflect the model boundary conditions and therefore measured tectonic stresses should help constrain models representing the driving mechanism. Richardson et al. (1979) conclude that models incorporating ridge push and asthenospheric drag on the lithosphere yield stress distributions which match observed mid-plate in-situ stresses better than alternate model configurations. Thus in-situ stress measurements promise to guide investigations into the mechanisms producing the earth's most significant tectonic processes.

The remaining body of interest in the in-situ stress state focuses on smaller regions where local contributions to the stress field become relevant. Consequently, the stress field influencing the response of rock results from the superposition of the tectonic stress field and local components of the stress field. In this case measurement of in-situ stress need only distinguish between the stress available to do work and the self-equilibrated residual stress. In general this is an easier task than a complete decomposition of the stress contributions as residual stress can be measured independently.

Prediction of earthquakes is an obvious application of in-situ stress measurement. Demonstrating the utility of in-situ stress measurements for predicting naturally occurring earthquakes is difficult, however, in various places man effects perturbations on the

stress field, thereby inducing earthquakes and those events can be anticipated with knowledge of the pre-existing state of stress. The classic example is the seismic swarm induced by pumping water into the Rangely, Colorado oil field (Raleigh et al., 1972). They report that the in-situ stress state was sufficiently well described to calculate the pore pressure required to initiate seismic activity. The actual value which stimulated earthquakes was close to the value predicted. Filling a man-made reservoir simultaneously increases the lithostatic load and the pore pressure, thus perturbing the stress field in predictable ways which might either induce of prevent earthquakes. Zoback and Hickman (1982) illustrate this by employing in-situ stress measurements to predict the seismic response to impounding the Monticello reservoir in South Carolina. Presumably a lithostatic state of stress (zero deviatoric stress) could be identified by in-situ stress measurements. Such a site cannot generate an earthquake (assuming one may rule out purely volumetric strain sources), because it is completely free of shear strain energy. Hence such sites would be good candidates for sensitive, earthquake vunerable projects, or for activities likely to generate stresses which might induce earthquakes in a stressed region. Radioactive waste disposal is an example of such an activity. The substantial heat produced by nuclear waste can potentially perturb the surrounding stress field (Hood, 1979; Hardy et al., 1979; Pratt et al., 1979), but if natural shear stress is absent, the threat of generating damaging earthquakes is much diminished.

In addition to the significance of in-situ stress to explaining

tectonic processes, a whole family of problems associated with exploitation of the earth's resources depends critically on the state of stress affecting man-made structures in the earth's crustal rocks. These appear in mining, drilling, and in fracturing rock.

Hydraulic fracturing is widely employed to increase production of energy from wells drilled into the earth's crust. Hubbert and Willis (1957) concluded that the local state of stress controls the direction hydraulic fractures propagate. Subsequent studies, aimed at developing hydraulic fracturing as a stress measuring technique, have repeatedly confirmed their result (Kehle, 1964; Haimson and Fairhurst, 1970; Zoback and Pollard, 1978). Predicting the size, shape and location of the fractures generated by hydraulic fracturing is critical for designing efficient approaches to exploit underground reservoirs.

This applies to secondary recovery from oil fields (Hubbert and Willis, 1957), to production from low-permeability gas formations (Smith et al., 1978; Hansen and Shaffer, 1979), and to geothermal energy development in hot dry rock regions (Murphy et al., 1981). In water flooding operations to increase production from an oil field the strategy is to move the oil toward a production well by injecting water in a nearby well. To increase the volume of oil captured the injection well is hydraulically fractured to enlarge the area flooded by the injected water. Hence the well geometry must be laid out so that the fractures produced from the injection well do not short circuit to a production well abandoning deposits of oil in between. The opposite situation occurs in developing closed loop geothermal systems. Water

injected through one well into a body of hot rock ideally travels along fractures directly to a production well where it is pumped out, relieved of its absorbed heat, and reinjected. Losses of the fluid to the rock must be minimized, thus accurate determination of the propagation of hydraulic fractures is essential to forming the loop initially and assuring that it remains closed to outside fluid loss. Prediction of the formation of massive hydraulic fractures used to produce gas from low-permeability gas-bearing formations is critical as the fractures are often propagated more than a kilometer from the injection well (Smith et al., 1978; Hansen and Shaffer, 1979). Two issues are important. First, that the fracture propagate within the confines of the gas-bearing body, and second, that the fracture does not provide alternate routes for the gas to escape the formation without flowing to the production well. Consequently, measuring the in-situ state of stress, the dominant influence over the direction of hydraulic fracture propagation is essential to modelling hydraulic fracturing and hence designing the most efficient course for developing an underground reservoir.

In mining applications the superposition of the local stress, the tectonic stress, and perturbations to the sum imposed by existing mine structures influence the behavior of the surrounding rock. The goal underlying designing the excavations for a mine is to remove as much ore, or in the case of tunnels built for access or transportation, to create the desired passage, as cheaply as possible, consistent with safe and sound structures. Many factors contribute to the stability of the

ultimate structure including its shape, the properties of the supporting rock, and the stresses acting upon the structure. Of the site properties the pre-excavation stress field is the most difficult to measure. However, the virgin rock stress field is concentrated by the mine excavation. Depending on the design of the tunnels and vaults this stress concentration can be maintained within acceptable limits, or if unheeded, may induce failure and possibly collapse. Hence the in-situ stress must be determined prior to designing the tunnels, pillars and rooms comprising a mine and furthermore, must be measured as mining progresses to insure that initial determinations are consistent with subsequent developments (Myrvang, 1979; Hiltscher et al., 1979; Dhar et al., 1979). One serious type of failure, rockbursts, can be identified as a potential problem early along from in-situ stress information, thus permitting incorporation of special designs to alleviate the threat posed by these dangerous events (Lee et al., 1979; Broch and Nilson, 1979).

One final application of in-situ stress information relates to drilling oil wells in tectonically active and consequently stressed regions. During drilling of an oil well the volume surrounding the drill string is filled with drilling mud circulated down through the hollow drill pipe to cool the drill bit and transport the cuttings to the surface. However, the mud also keeps the hole from collapsing onto the drill string by exerting pressure on the inside of the borehole. The drilling engineer controls the magnitude of this pressure by varying the mud density. Excessive pressure is as hazardous as insufficient

pressure as it may produce unintended hydraulic fracturing of the well bore which leads to loss of the coolant and possibly collapse of the hole. In a low horizontal stress environment such as the Gulf Coast, these scenarios occur rarely, however in high horizontal stress regimes, as the Gulf of Alaska, the high horizontal stress differences aggravate both problems due to the stress concentration at the borehole wall, making borehole stability a serious concern (Hottman, et al., 1979). This becomes particularly significant when drilling offshore where lost time is extraordinarily costly. To avoid borehole instability, drilling plans include casing the open part of the hole more frequently to reduce the range of mud pressures along the open part of the hole allowing closer tailoring of the mud weights to the pressure conditions required to prevent sloughing into the hole and still avoid fracturing and losing coolant. Accurate measurements of the in-situ stress state responsible for the complications are essential to design the appropriate drilling program.

In-Situ Stress Measuring Techniques

Excellent reviews and comparisons of the instrumental techniques for measuring stress are available in the current linterature (McGarr and Gay, 1978; Jaeger and Cook, 1979; Pincus et al., 1982) obviating the need to do so again here. Furthermore, each individual technique is thoroughly described in the separate reports referenced in the above-mentioned reviews. Consequently I will discuss the various approaches for measuring in-situ stress only briefly, primarily to

indicate their limitations, thereby explaining our motivation in developing a new instrument directed at the same goal.

Stress measuring techniques can be classified into two categories, those that measure stress and those that record strain relief to infer stress. These are also referred to as active and passive techniques respectively. The two principal techniques that measure stress directly are the flatjack (Jaeger and Cook, 1979), and hydraulic fracture (Hubbert and Willis, 1957; Haimson and Fairhurst, 1970; Zoback and Pollard, 1978). The advantage of measuring stress directly is its independence from the elastic properties of the rock. However, multiply oriented boreholes for hydraulic fracture and multiple mine faces for the flatjack are required to completely determine all components of the in-situ stress tensor.

Many techniques rely on measuring strain relief from a known disturbance of the in-situ rock. These include: the "doorstopper" (Leeman, 1969), the C.S.I.R. triaxial strain cell (Leeman and Hayes, 1966), the U.S.B.M. deformation gage (Hooker et al., 1974) and the holographic stressmeter. Then using elastic properties of the rock, determined separately, and solutions for stress concentrations in an elastic solid due to appropriate instrument-specific configurations, various components of the in-situ stress tensor may be calculated. The main drawback of all of these techniques, except for the holographic stressmeter, is the necessity of overcoring the recording device in the borehole which presupposes a drill rig and its associated expense. Furthermore, overcoring is generally limited to depths of 50 meters or

less, although Hiltscher et al. (1979) report successful deployment of the triaxial strain cell to depths of several hundred meters. In addition, only the holographic stressmeter and the triaxial strain cell record sufficient information to determine all six independent components of the stress tensor.

The anticipated advantages of the holographic stressmeter compared to hydraulic fracturing are ease and inexpensive deployment for a larger amount of information. Hydraulic fracturing requires multiple entries into a borehole with a drill string. In contrast, the holographic stressmeter operates on a wireline, at virtually any depth, at least in theory. However, hydraulic fracturing operates successfully in deep mud-filled boreholes, while the holographic stressmeter has been tested only in dry boreholes and boreholes filled with clear water. For additional discussion of the operating characteristics of the various stress measuring instruments I recommmend the review articles or individual reports already mentioned.

In summary, many pursuits require information on the state of stress in-situ in rocks. The situations where in-situ stress must be determined encompass a wide range of environments, from dry, hard-rock mines to beneath the sea floor, however, even under ideal conditions measuring the absolute state of stress is intrinsically difficult. Consequently the search for better approaches to measuring stress continues. We present the holographic stressmeter, described here, as a promising, though as yet unproven, contribution toward this goal.

CHAPTER 2

Elastostatic Relationships Underlying Borehole Stress Measurements

Introduction

The goal behind developing an instrument to measure in-situ stress is to discover the virgin, or far-field stress acting deep within crustal rocks. Simply drilling a borehole into some stressed rock mass of interest seriously perturbs (or concentrates) the stress field, particularly near the surface of the borehole. The approach adopted in developing the holographic stressmeter is to sample the stress field at the borehole wall. Then, using known relationships for the stress concentration due to the borehole, assuming rock behaves elastically, we can relate our measured values to the far-field stress values which we wish to determine. This chapter discusses the relevant elastostatic problem, its solution, and how it contributes to interpreting borehole in-situ stress measurements.

The problem we wish to solve is as follows: given an infinite solid containing an infinite cylindrical hole, the borehole, what information about the stresses on the surface of the hole is necessary to determine the stress in the infinite solid if without the hole we knew the stress would be uniform throughout. This is the appropriate formulation as we wish to determine the far-field stresses affecting a virgin volume of rock before introducing the borehole and its associated

perturbations. Since we assume the solid is isotropic, and we assume the two elastic constants describing its elastic properties are known, we are looking for six values, the six independent components of the unknown far-field stress tensor.

Instead, we will examine the problem from the point of view of determining the stresses acting at the surface of an infinite cylindrical hole emplaced in an infinite solid with a prior-existing, arbitrary, but uniform stress field. By Saint Venant's principle this is equivalent to solving the problem of the stress distribution in an infinite solid containing a cylindrical hole with arbitrary, but uniform stresses applied at infinity. This problem has been solved by Hiramatsu and Oka (1962), but because it is derived using principal stress magnitudes and direction cosines to principal axes, we will reproduce an equivalent solution, presented by Leeman and Hayes (1966), in terms of arbitrary tensor stresses represented in a cylindrical coordinate system tied to the borehole. In this form the solution is much simpler, and as the stresses are related by the usual tensor transformations to their forms when stated in a coordinate system related to the natural directions on the earth, this framework is convenient. We will then show that the solutions applied to the surface of the hole may be algebraically inverted to yield the desired far-field stress in terms of stresses at the hole surface.

Since the analysis comprising this chapter forms the foundation of the approach to measuring stress utilized in the holographic stressmeter it is appropriately treated first, deferring the detailed discussion of

the theory and operation of the instrument to Chapter 3. However, a basic understanding of how the instrument actually makes its measurements is desirable for motivating and focusing this analysis.

Stressmeter Operation

The instrument operates in a cylindrical borehole contained in the volume of rock of interest. It could be an abandoned oil well, water well, or hole specially drilled to measure stress. At any particular point along the borehole the exposed rock surface is called the borehole wall. The instrument drills a small strain-relieving hole, the side-core hole, into the borehole wall. This causes the remaining wall rock surrounding the side-core hole to readjust slightly as it reequilibrates to the new boundary contitions.

We illustrate these motions, very much exaggerated, in figure 2-1. The holographic stressmeter employs optical holography to record these minute strain-relief displacements occurring on the exposed surface of the borehole wall surrounding the side-core hole. The relationship between these displacements, the properties of the rock, and the far-field stresses acting on the rock and penetrating borehole are examined below.

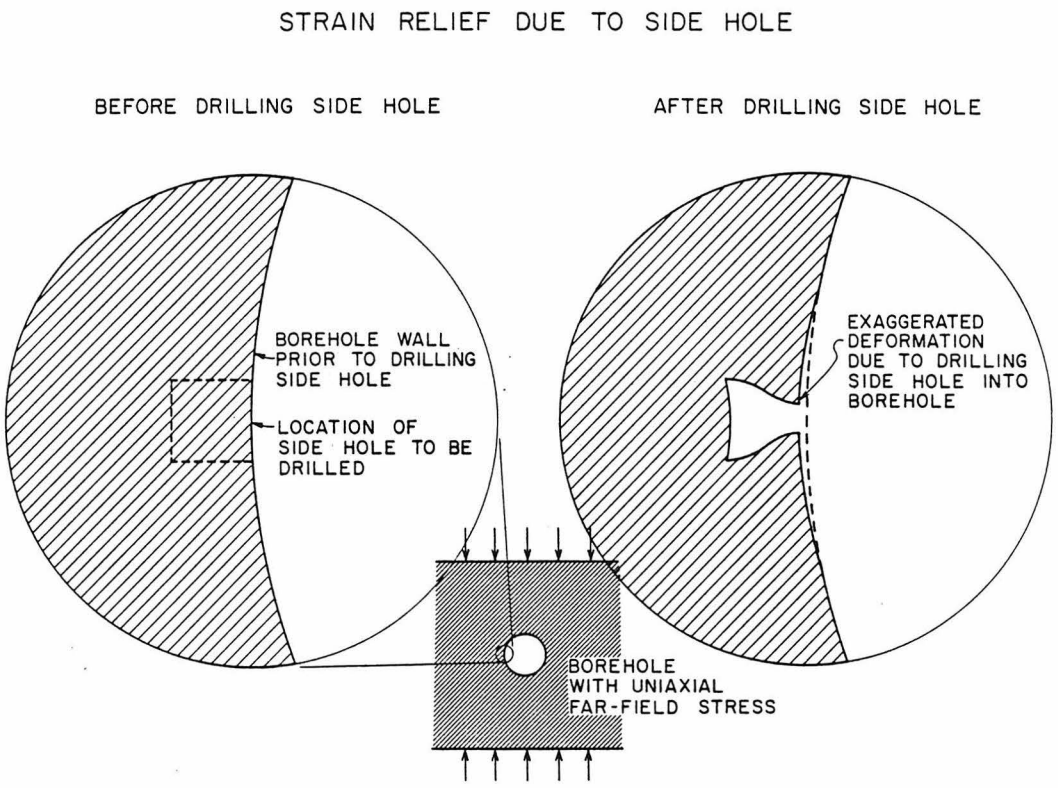

Figure 2-1 Cartoon showing exaggerated strain-relief deformation produced by drilling a side-core hole into the borehole wall when borehole is subjected to uniaxial far-field compression.

Assumptions and Definitions

Several assumptions must be stated at this stage before embarking on such an analysis. First, that the rock being studied behaves as a linear elastic solid. In other words, stress in the rock is proportional to its strain. In fact, most rocks do approximate linear elastic response up to the point of brittle failure (Jaeger and Cook, 1979, p. 78) so we are justified in making this assumption. Second, we assume that the rock is isotropic. Most rocks, particularly thin-bedded sedimentary rocks under low confining pressures, exhibit measurable anisotropy (Birch, 1966). However, this anisotropy is seldom large enough to introduce serious differences between elastostatic analysis assuming isotropy and analysis which takes elastic anisotropy into account (Jaeger and Cook, 1979, p. 137). We will assume for this analysis that rock does behave isotropically, while keeping in mind that under the circumstance of pronounced anisotropy this analysis is invalid and consequently may yield incorrect interpretations.

A third assumption we must make is that the rock and stress field we are sampling is homogeneous. This actually implies several assumptions, each applicable to a particular length scale. On the scale of tens of meters to kilometers, or whatever distance over which we wish to assign a uniform value of stress, we must assume that the stress field in the rock is fairly constant, though obviously varying with depth. If the stress state were to vary laterally in an irregular and substantial manner, point measurements would yield misleading information about the surrounding region unless sufficiently many were

made making statistical analysis appropriate. As boreholes are expensive, prohibiting high sampling density in more than one dimension, we assume for the present, and must demonstrate in the future, that a single borehole in a subregion of a geologically homogeneous terrain adequately samples the stress field in that subregion. This issue is closely related to the effect of residual stresses which are discussed in Chapter 4.

On the scale of the diameter of the borehole we must assume that the elastic properties, and hence the composition, are slowly varying spatially. Otherwise, variations in the elastic properties will seriously affect the concentration of stress around the borehole. This includes compositional deviations, stress-relieving joints, fractures, or bedding planes, et cetera. Clearly sampling the stress field in a cobble conglomerate (clasts 6-25 cm in size), with a 10-cm-diameter borehole is likely to yield diverse values depending upon which cobbles the borehole happens to penetrate, and whether one samples the cobbles or the surrounding matrix.

On the scale of the diameter of the strain-relieving side-core hole drilled to measure the stress, the same requirements for homogeneity must be met. Thus the grain size of the rock must be at least several times smaller than the diameter of the side-core hole, or possibly substantially larger.

The simplest solution is to assume perfect homogeneity of the elastic properties and stress field over all dimensions of interest. We will adopt that assumption for the following analysis, aware that when

actually applying the results of this analysis to observations made in the field, the validity of each of the assumptions so implied must be addressed.

In discussing stress and stress-strain relations several conventions and a set of units must be adopted. In the analysis that follows I have chosen the following. Tensor stresses and strains are used throughout. Hence, the shear components will refer to the off-diagonal (shear) values of the appropriate stress or strain tensor. I have arbitrarily selected positive strain to be extensional which leads directly to positive stress being tensional, the opposite of what is generally found in earth-sciences literature. Since the stresses in the earth are almost universally compressive, in this scheme, their values will be negative. (They must be entered as such into the codes written in association with this research.) However, in the figures included herein, where actual values of normal stress are indicated, the minus signs are omitted. It should be understood that all normal stresses denoted in figures are compressional and are usually so indicated by converging arrows. The cases selected for elucidation in figures are chosen for simplicity, and as a result of the nature of the relevant elastostatic solutions to be discussed below, shear stresses usually vanish. In the rare instances where shear stresses do appear, their directions of action are indicated and their signs are correct, even though the compressional normal stresses are indicated without sign.

Stress magnitudes are given in bars. One bar is equivalent to

10^5 Pascal (N/m^2), the unit of stress in the Système International (SI) arrangement of standard units. Lengths appear in the standard metric units with the exception of λ which represents one wavelength. As the recording technique employed in this project relies on He-Ne laser illumination, in what follows, λ represents the wavelength emitted by a He-Ne laser which is .0006328 mm, in the red region of the visible spectrum.

Coordinate Systems

Several different coordinate systems are used throughout the discussion of borehole stress concentration, stress measurement, and interpretation of the data recorded by the stressmeter. They are summarized here.

The geographic coordinate system is a cartesian coordinate system with the basis vectors aligned with the earth's local east, north, and up. Closely related is the geophysical coordinate system, a spherical coordinate system with the components: radius, declination (positive degrees east of north), and inclination (degrees from horizontal, positive up), which is most widely used to report the principal axes of stresses measured in the earth.

Since the far-field stress state is reported in terms of principal stresses and directions of principal axes in the geophyscal coordinate system, we need a coordinate system which relates the tensor representation of the stress state to the borehole to simplify the representation of the stress concentration of the borehole. This is the

first of two borehole coordinate systems, the borehole cartesian coordinates. It is a cartesian system with basis vectors X, Y, and Z. Z is oriented along the axis of the borehole from the origin toward the surface, or collar of the borehole. X is orthogonal to Z and is at the azimuth of the first side-core hole drilled at a particular level in the borehole. Y is orthogonal to X and Z and forms a right-handed reference frame. Figure 2-2 indicates this coordinate system in several places. Shown in the lower right-hand corner is a unit cube indicating the individual stress components of the far-field stress in this coordinate system.

We introduce the borehole cylindrical coordinate system, closely related to the borehole cartesian system, to most simply represent the stress concentration due to the borehole. This is a cylindrical coordinate system with the components: r (radius), θ (angle from X, positive from X to Y), and Z which is identical to Z in the borehole cartesian system. This coordinate system is also shown in figure 2-2 along with a unit cylindrical volume indicating, in this reference frame, the individual stress components of the stress field within the zone influenced by the borehole.

The last two coordinate systems are the side-core hole coordinates. Three of the cartesian side-core hole coordinate frames are shown in figure 2-3. One for each of the three side-core holes in the borehole wall. In the cartesian side-core hole coordinate system the three basis vectors x, y, and z are defined as follows: x is tangent to the borehole wall in the direction of positive θ; y is in the direction of

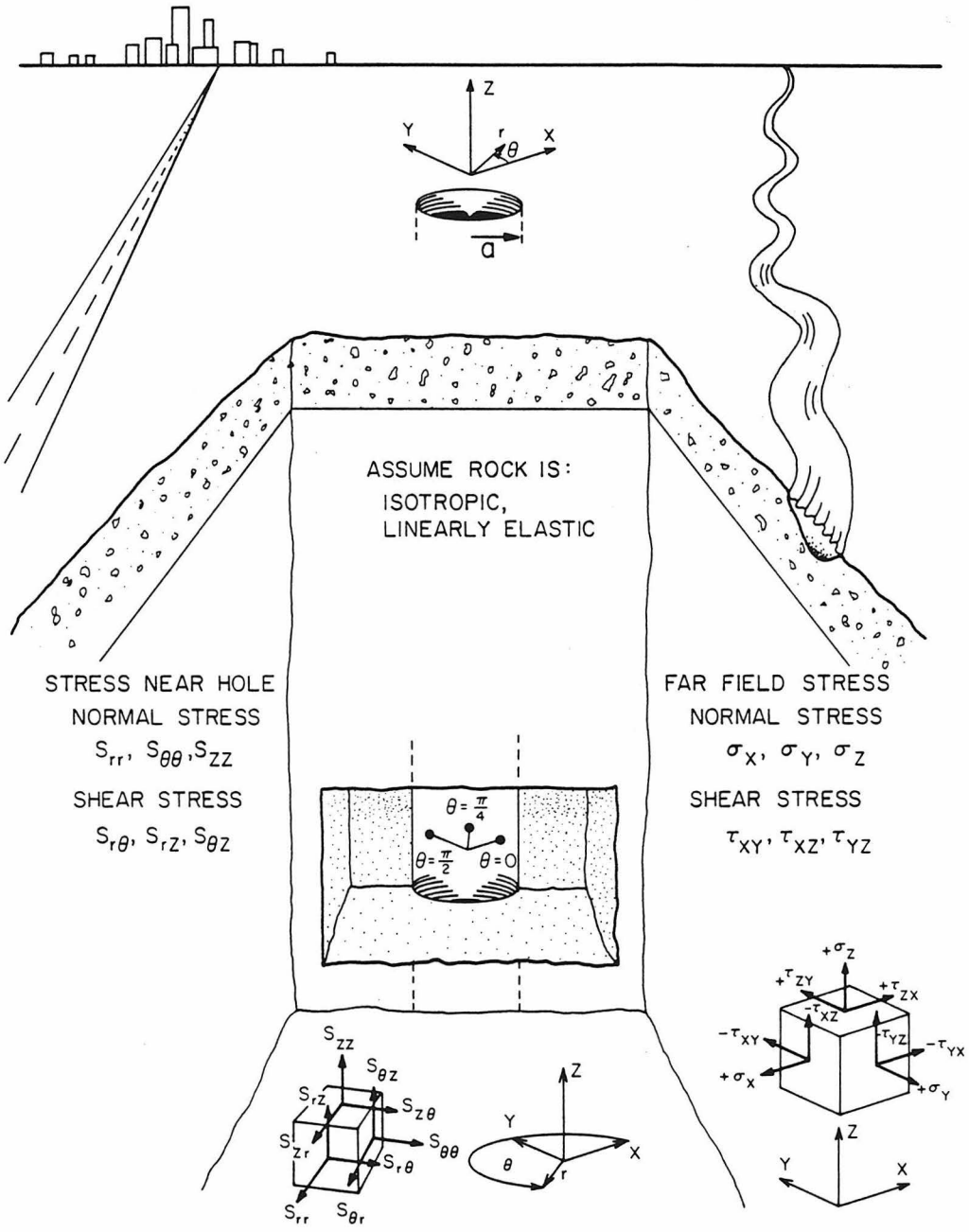

Figure 2-2 Relation between the borehole cartesian coordinate system and far-field stresses acting on a unit cube, shown at the right, and borehole cylindrical coordinates and stresses depicted on a unit cylindrical volume, for stresses near the borehole, shown in the center.

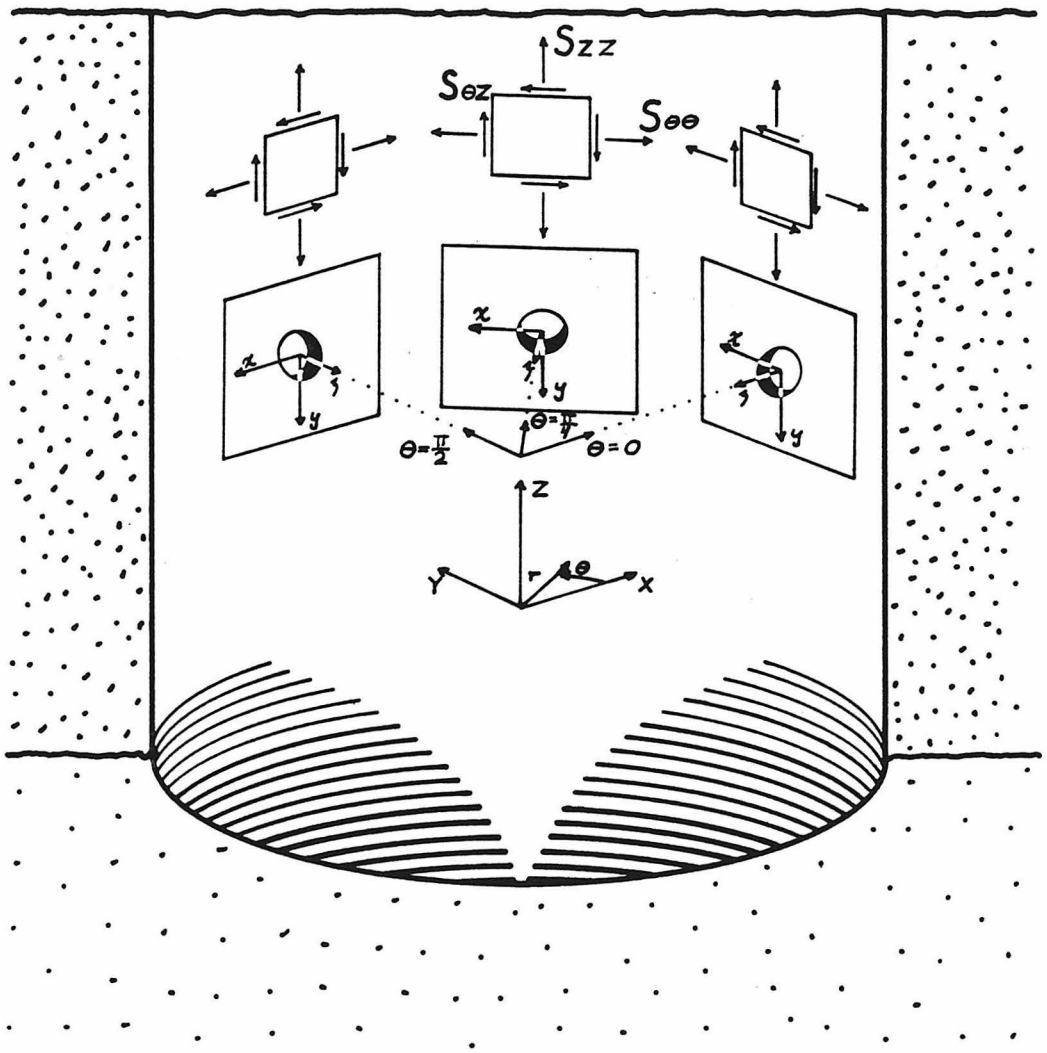

Figure 2-3 Three side-core holes into the borehole wall and the geometric relationship between the side-core-hole coordinate systems and the borehole coordinate system. Plane-stress configurations indicate the three non-vanishing stresses at each point on the borehole wall.

-Z; z is the local normal to the borehole wall, oriented in the -r direction. The origin is the center of the side-core hole at the surface of the borehole wall. This coordinate system is used to relate the stresses acting in the small region around the side-core hole to the stresses acting on the borehole wall.

The final coordinate system is the cylindrical side-core hole coordiate system, used in Chapter 4 in the analysis of the displacements on the surface of a stressed medium surrounding a hole drilled into it to relieve strain. It has the components ρ (radius from the center of the side-core hole), ϕ (angle from x, positive from x to y), and z which is identical to the z in the cartesian side-core hole coordinate system.

Introduction of all of these coordinate systems permits solution of the relevant elastostatic problems in the simplest form at each stage and indicates directly how information about the stress at one stage of analysis may be transmitted to the next.

Stress Concentration Due to a Borehole

The desired solution is schematically depicted in figure 2-2. Given an arbitrary far-field stress shown in terms of σ_{ij}, for the normal stress components, and τ_{ij}, for the shear components, acting on the unit cube in the borehole cartesian coordinate system (lower right corner of figure), what are the stress components S_{ij} in the borehole cylindrical coordinate system (lower center part of figure), as a function of r and θ. In the problem as stated, clearly they should be independent of Z and should tend to the far-field values in the limit of

large r.

The solutions for the stresses S_{ij} in the borehole cylindrical coordinate system (Leeman and Hayes, 1966), are given in equations 2-1 as a function of r and θ, in terms of σ_{ij} and τ_{ij}, the far-field stresses in the borehole cartesian reference frame. Notice that the solution scales as the diameter of the hole a, implying the peak stress perturbations are independent of the hole diameter, and also that the stresses depend on only one elastic constant, Poisson's ratio ν.

$$S_{rr} = \frac{\sigma_x + \sigma_y}{2}\left[1 - \frac{a^2}{r^2}\right] + \frac{\sigma_x - \sigma_y}{2}\left[1 + 3\frac{a^4}{r^4} - 4\frac{a^2}{r^2}\right]\cos 2\theta + \tau_{xy}\left[1 + 3\frac{a^4}{r^4} - 4\frac{a^2}{r^2}\right]\sin 2\theta \quad (2\text{-}1a)$$

$$S_{\theta\theta} = \frac{\sigma_x + \sigma_y}{2}\left[1 + \frac{a^2}{r^2}\right] - \frac{\sigma_x - \sigma_y}{2}\left[1 + 3\frac{a^4}{r^4}\right]\cos 2\theta - \tau_{xy}\left[1 + 3\frac{a^4}{r^4}\right]\sin 2\theta \quad (2\text{-}1b)$$

$$S_{zz} = -\nu\left[2(\sigma_x - \sigma_y)\frac{a^2}{r^2}\cos 2\theta + 4\tau_{xy}\frac{a^2}{r^2}\sin 2\theta\right] + \sigma_z \quad (2\text{-}1c)$$

$$S_{r\theta} = -\frac{\sigma_x - \sigma_y}{2}\left[1 - 3\frac{a^4}{r^4} + 2\frac{a^2}{r^2}\right]\sin 2\theta + \tau_{xy}\left[1 - 3\frac{a^4}{r^4} + 2\frac{a^2}{r^2}\right]\cos 2\theta \quad (2\text{-}1d)$$

$$S_{rz} = (\tau_{xz}\cos\theta + \tau_{yz}\sin\theta)\left[1 - \frac{a^2}{r^2}\right] \quad (2\text{-}1e)$$

$$S_{\theta z} = (-\tau_{xz}\sin\theta + \tau_{yz}\cos\theta)\left[1 + \frac{a^2}{r^2}\right] \qquad (2\text{-}1f)$$

The above expressions and the remainder of this analysis assumes insignificant fluid pressure acts on the borehole wall. This is appropriate for analysis of our data obtained in the field, and the modification required to include the effects of fluid pressure, while simple, does unnecessarily complicate the expressions. Thus the surface of the borehole is free of normal and shear stresses requiring S_{rr}, $S_{r\theta}$, and S_{rz} to vanish. When the Z-axis, the axis of the borehole, coincides with a direction of principal stress, the shear terms τ_{iz} of the far-field stress expressed in the borehole cartesian reference frame vanish. As a result, by examination of expressions 2-1, $S_{\theta z}$ and S_{rz} must vanish everywhere. The remaining two stresses S_{zz} and $S_{\theta\theta}$ are plotted in the upper part of figure 2-4 as a function of radial distance from the axis of the borehole, for a particular stress state, for the three different azimuths depicted in the lower part of the figure. (The stress state: 70 bars vertical, with 35 and 88 bar horizontal principal stresses was arbitrarily selected, as a representative stress state, to make this figure.) The lower diagram in figure 2-4 depicts a plan view of the borehole and the applied stress field. The two stress figures, connected to the plan view by dashed lines, are orthographic views (as in an engineering drawing), of the stresses which act on the borehole wall, and whose values are plotted in the graph above. Figure 2-4 demonstrates that while a stress concentration factor between two and three can readily occur, implying substantial stress perturbations near

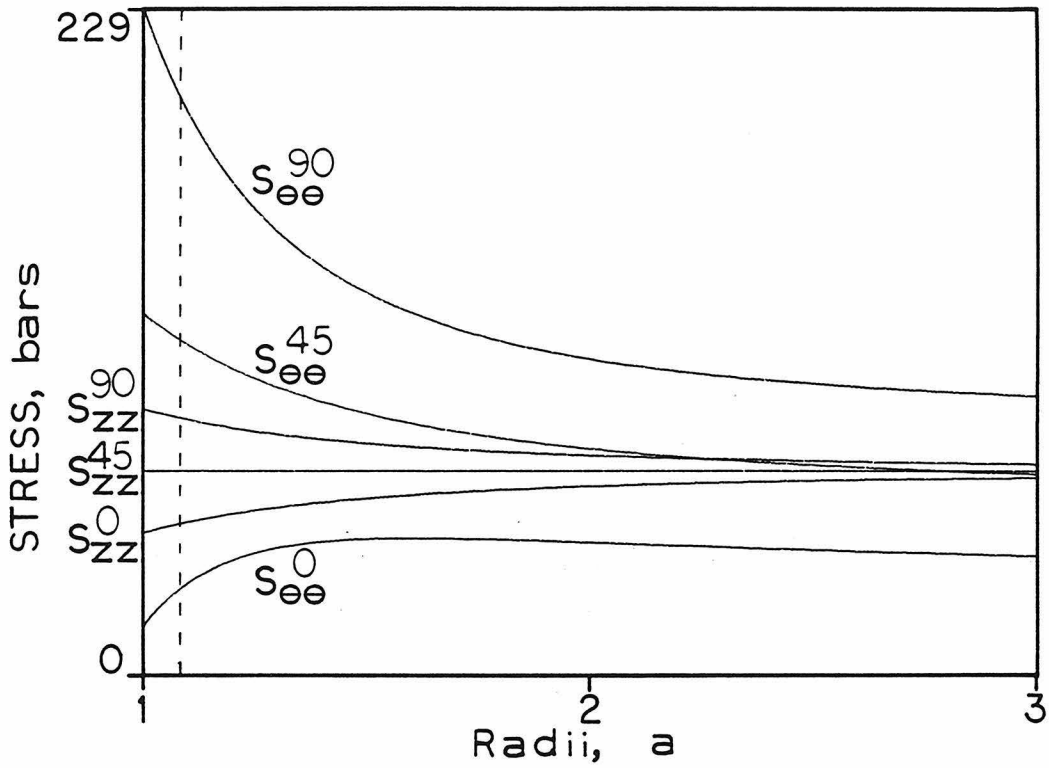

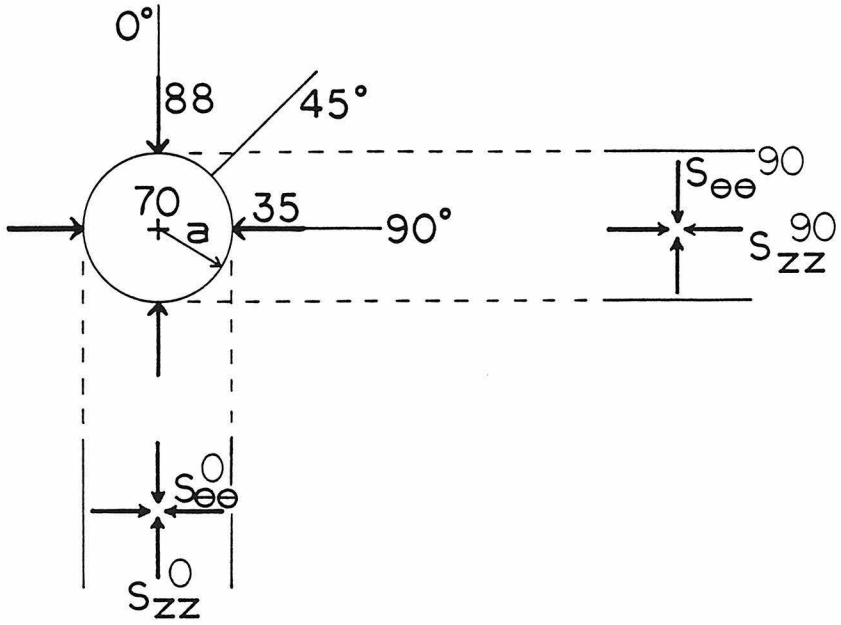

Figure 2-4 Concentration of axial and hoop stresses due to an infinite cylindrical borehole plotted as a function of borehole radius. Lower diagram is a three-view orthographic projection of borehole and stresses.

the borehole wall, within one diameter of the borehole surface the stress returns approximately to its far-field value.

However, because the holographic stressmeter samples the stress field at the borehole surface (In the NTS experiments the side-core holes penetrated to the nondimensional depth indicated on the upper part of figure 2-4 by the vertical dashed line.) our concern is with the values of the stresses at the borehole wall. Equating r and a in expressions 2-1 yields, as expected, only three non-vanishing stress components: $S_{\theta\theta}$, S_{zz}, and $S_{\theta z}$, in equations 2-2.

$$S_{\theta\theta} = \sigma_x + \sigma_y - 2\,(\sigma_x - \sigma_y)\cos 2\theta - 4\,\tau_{xy}\sin 2\theta \qquad (2\text{-}2a)$$

$$S_{zz} = -\,\nu\,[2\,(\sigma_x - \sigma_y)\cos 2\theta + 4\,\tau_{xy}\sin 2\theta] + \sigma_z \qquad (2\text{-}2b)$$

$$S_{\theta z} = -\,2\,\tau_{xz}\sin\theta + 2\,\tau_{yz}\cos\theta \qquad (2\text{-}2c)$$

These three expression can each be evaluated as a function of θ. Solving them sequentially for $\theta = 0$, $\pi/4$, and $\pi/2$ yields equations 2-3, 2-4, and 2-5. These solutions are also indicated in figure 2-5 in the corresponding locations around the borehole.

$\theta = 0$

$$S_{\theta\theta}\ (r=a,\ \theta=0) = -\sigma_x + 3\,\sigma_y \tag{2-3a}$$

$$S_{zz}\ (r=a,\ \theta=0) = -2\,\nu\,(\sigma_x - \sigma_y) + \sigma_z \tag{2-3b}$$

$$S_{\theta z}\ (r=a,\ \theta=0) = 2\,\tau_{yz} \tag{2-3c}$$

$\theta = \pi/4$

$$S_{\theta\theta}\left(r=a,\ \theta=\frac{\pi}{4}\right) = \sigma_x + \sigma_y - 4\,\tau_{xy} \tag{2-4a}$$

$$S_{zz}\left(r=a,\ \theta=\frac{\pi}{4}\right) = -4\,\nu\,\tau_{xy} + \sigma_z \tag{2-4b}$$

$$S_{\theta z}\left(r=a,\ \theta=\frac{\pi}{4}\right) = -\sqrt{2}\,(\tau_{xz} - \tau_{yz}) \tag{2-4c}$$

$\theta = \pi/2$

$$S_{\theta\theta}\left(r=a,\ \theta=\frac{\pi}{2}\right) = 3\,\sigma_x - \sigma_y \tag{2-5a}$$

$$S_{zz}\left(r=a,\ \theta=\frac{\pi}{2}\right) = 2\,\nu\,(\sigma_x - \sigma_y) + \sigma_z \tag{2-5b}$$

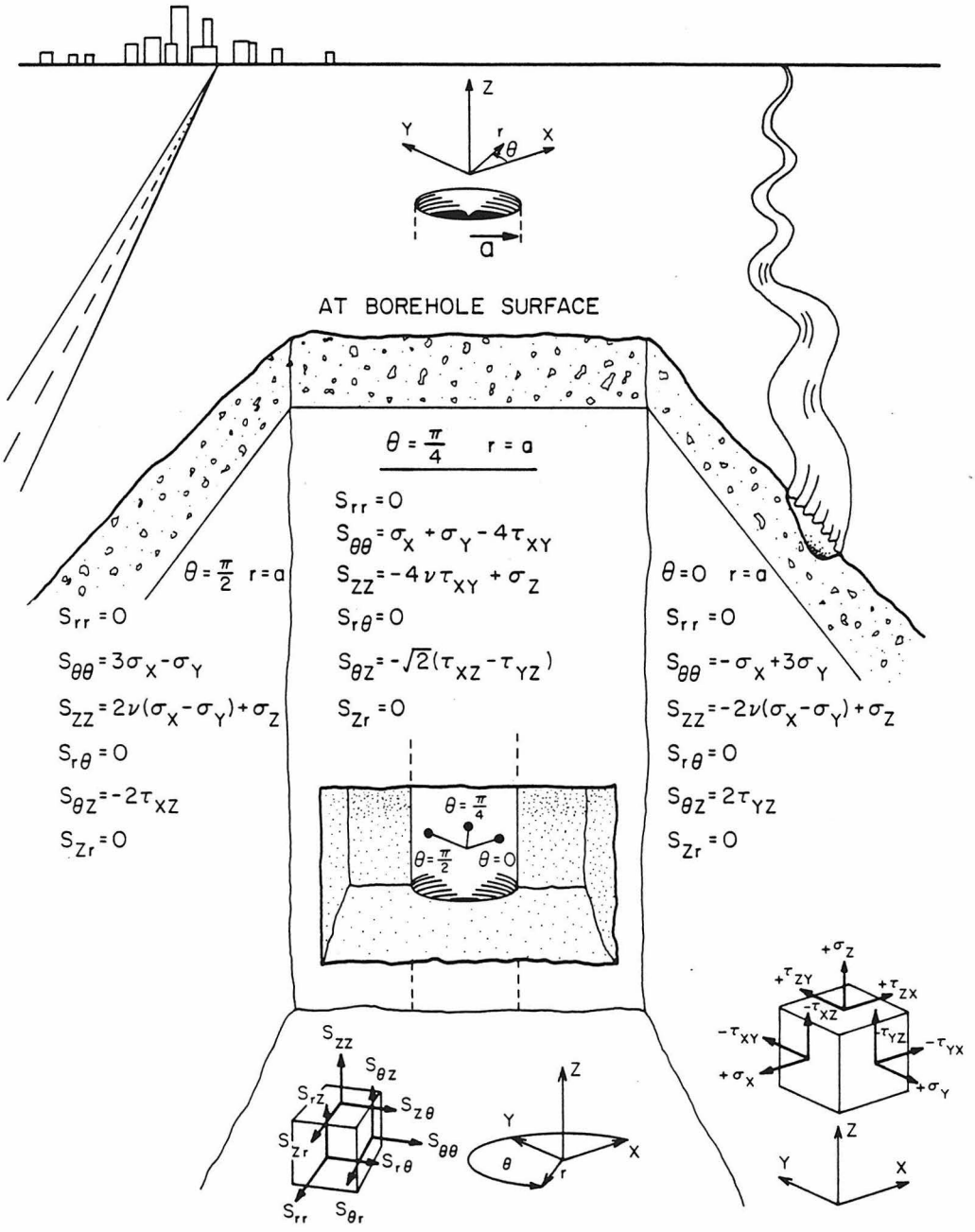

Figure 2-5 Stresses at borehole wall as a function of far-field stresses and azimuth.

$$S_{\theta z}\left(r=a,\ \theta=\frac{\pi}{2}\right)=-2\,\tau_{xz} \tag{2-5c}$$

Now, identifying each of these $S_{ij}(r=a,\theta)$ by a superscript indicating the value of θ, we will algebraically solve these nine equations 2-3 to 2-5 for the six far-field stresses σ_{ij} and τ_{ij} expressed in the borehole cartesian coordinate system, yielding the six equations 2-6.

$$\sigma_x=\frac{1}{8}\left(3S_{\theta\theta}^{\pi/2}+S_{\theta\theta}^{0}\right) \tag{2-6a}$$

$$\sigma_y=\frac{1}{8}\left(3S_{\theta\theta}^{0}+S_{\theta\theta}^{\pi/2}\right) \tag{2-6b}$$

$$\sigma_z=S_{zz}^{0}+\frac{\nu}{2}\left(S_{\theta\theta}^{\pi/2}-S_{\theta\theta}^{0}\right) \tag{2-6c}$$

$$\tau_{xy}=\frac{1}{8}\left(S_{\theta\theta}^{0}+S_{\theta\theta}^{\pi/2}-2S_{\theta\theta}^{\pi/4}\right) \tag{2-6d}$$

$$\tau_{yz}=\frac{1}{2}\,S_{\theta z}^{0} \tag{2-6e}$$

$$\tau_{xz}=-\frac{1}{2}\,S_{\theta z}^{\pi/2} \tag{2-6f}$$

The equations 2-6 imply that to determine all six components of the far-field stress tensor we must determine six components of stress acting at the borehole wall, distributed between three specific azimuths. Figure 2-6 shows the stresses which must be measured. At $\theta=0$, $S_{\theta\theta}$, S_{zz}, and $S_{\theta z}$ must be determined; at $\theta=\pi/4$, $S_{\theta\theta}$, and at $\theta=\pi/2$, $S_{\theta\theta}$ and $S_{\theta z}$ must be determined. The three values not required simply provide redundant information about the far-field stresses.

There is no particular advantage to selecting the azimuths in the approach above. There are many combinations of three azimuths which provide the same information and there may be instrument-design motivations to select a different combination. Nevertheless, it is clear that if you can measure the three stresses acting at the borehole wall at three azimuths, as shown in figures 2-3 and 2-6, then you obtain sufficient information to determine all six components of the far-field stress tensor.

Discussion and Conclusions

To apply the above elastostatic solutions to our rock-mechanics problem we require the rock be homogeneous, isotropic, and linearly elastic. Rocks encountered in the field often fail to meet at least one and more likely all three of these standards exactly. However, as stated above, most cold rocks are well characterized by linear elasticity up to the point of failure and while elastic anisotropy is common, it is generally of sufficiently small magnitude that solutions based on isotropy are satisfactory approximations. Homogeneity of a

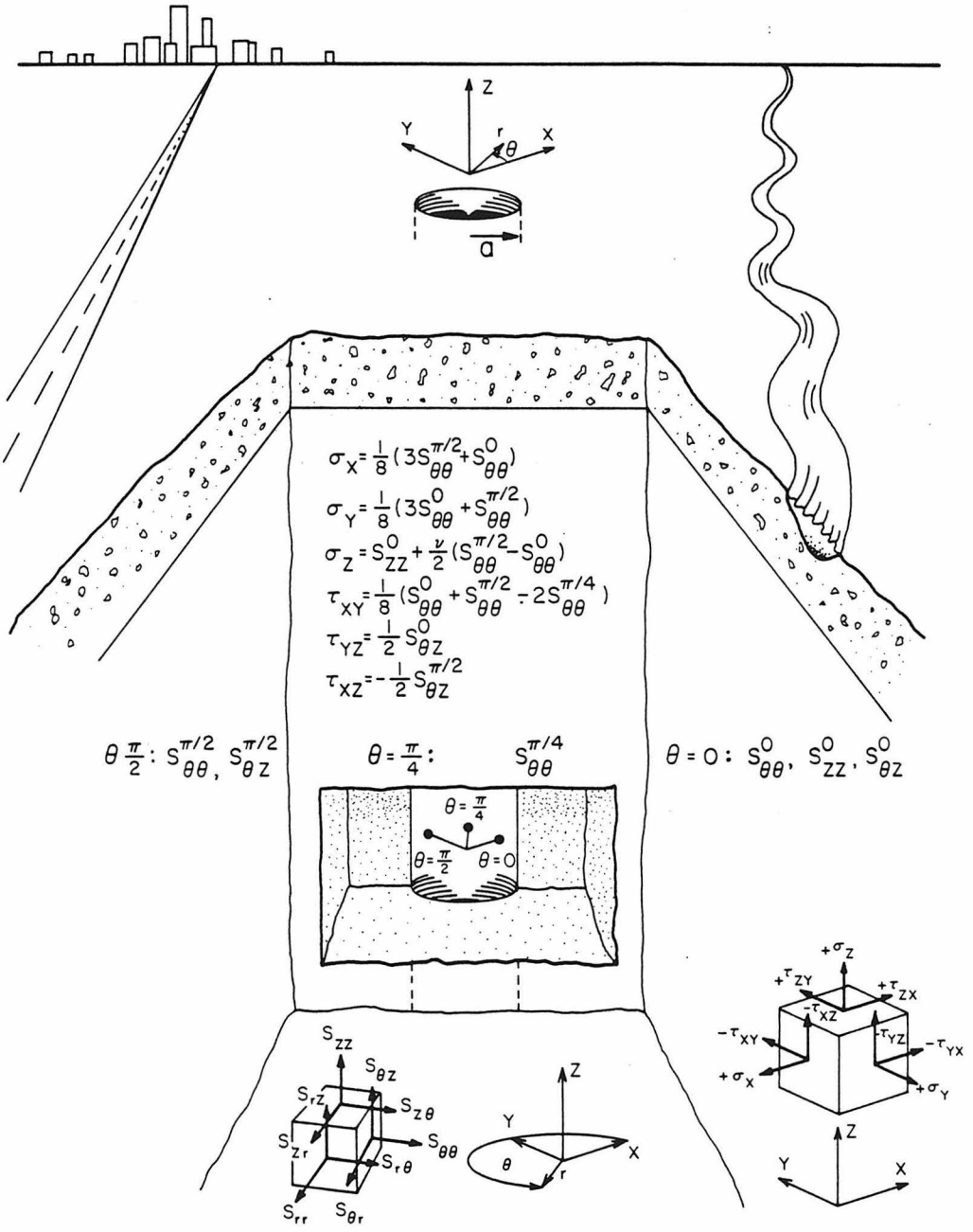

Figure 2-6 Far-field stresses in terms of stresses to be measured at the three required azimuths on the borehole wall.

rock mass can be judged from geologic investigations, including studies of structural elements such as fractures, joints and bedding, as well as lithology.

If the assumptions are valid in a particular situation then the problem of determining the far-field stress in a rock mass is reduced to finding six stresses acting at the surface of a borehole penetrating the rock mass. Notice that nowhere in this analysis were any constraints placed on the far-field stresses, such as alignment of the borehole with a principal stress axis. The solution is completely general, permitting determination of all six independent components of the far-field stress tensor regardless of the orientation of the principal stress axes.

CHAPTER 3

Holographic Stressmeter: Theory
Design and Operation

Introduction

We have developed the holographic stressmeter to make measurements of stress in crustal rocks at substantial distances (kilometers eventually) from the earth's surface, in uncased boreholes. It is intended to be an inexpensive tool to employ in the field. Consequently it has been designed to operate independently, without assistance from a drill rig, and to require only a single entry into a hole to do its sampling. The strain-relief drilling required for making each stress measurement is accomplished by an on-board drilling unit which offers two advantages. The first is saving the cost of operating a drill rig. The second is the freedom to work at depths beyond the range of overcoring techniques (the usual methods of strain relief) which are generally limited to 50 m from the free surface. Furthermore, the cost of operation is very much reduced by using existing drill holes, where possible.

The present field-prototype instrument was assembled and deployed experimentally in the course of this research. Previous successful utilization of this technique for rock stress measurement by Schmidt et al. (1974) and Ahrens et al. (1975) motivated this, the second stage of on-going development. The first-stage efforts included building

parts of a laboratory instrument which could be secured into an artificial, 23-cm-diameter, borehole constructed of concrete. A machined granite specimen, stressed uniaxially by a clamping device, was inserted through a port in the laboratory borehole and fastened in place. From the inside of the water-flooded borehole the granite was strain relieved by drilling a 6-mm-diameter side-core hole with a diamond core drill, while the associated deformations were recorded holographically. Their achievement of sufficient stability for the holographic recording system to function in the laboratory encouraged our designing and constructing an instrument capable of withstanding the rigors and irregularities associated with operating in the field environment. Although many of the active elements have been changed, parts of the original chassis for the drill and optics modules (Schmidt et al., 1974) were modified and integrated into the field version of the instrument. The entire laser and control modules, the film system, the locking mechanisms for both units, and the housing for the optics module were designed and built from scratch. The physical components that currently control the size of the instrument need not be as large as they are. With ingenuity they could easily be reduced in size by a factor of two. The current prototype of the stressmeter requires a 30-cm-diameter borehole. To take advantage of the substantial population of accessible boreholes, the next version of the stressmeter must be completely redesigned on a smaller scale.

This chapter discusses the theory behind the operation of the holographic stressmeter and how it actually conducts a stress

measurement. It then describes how these concepts are realized in the separate components that constitute the field prototype instrument. Finally we present some examples of data obtained during experimental field deployment of the stressmeter. Discussion and interpretation of these data are left to Chapter 4.

Holographic Interferometry

Holographic interferometry, or double exposure holography, relies entirely upon the capacity of holography to reconstruct, at some later time, the amplitude and phase of light radiated by a scene during the exposure producing the hologram. It appears frequently in the literature as a technique for studying deformation of materials (Haines and Hildebrand, 1966; Alexander and Bonch-Bruevich, 1967), and occasionally in the study of strain and thermal expansion in rocks (Heflinger et al., 1973). The reader unfamiliar with holography is encouraged to read Appendix A, Fundamentals of Holography, an easy tutorial on the basics of wavefront reconstruction, before proceeding further. Failing that, it is possible to understand the interferometric concepts discussed in this chapter by accepting that the holographically reconstructed wavefront, for all intents and purposes, is identical to the wavefront that the subject of the hologram would have radiated if it were positioned at the location of the reconstructed virtual image and illuminated with the same light source.

Interference holography is founded on the idea that two holographically reconstructed wavefronts can optically interfere with

each other in the same fashion that the reference and object beams interfere originally in forming the hologram (Brown et al., 1969). Recording a single exposure hologram of an object and then recording a second holographic exposure of the same object using the same reference beam and the same film plate achieves the desired result. When the holographic plate is processed and reconstructed, both the wavefront forming the virtual image of the first scene and the wavefront forming the virtual image of the second scene are reproduced simultaneously since they were both recorded using the identical reference beam. Both wavefronts are recreated with the correct amplitude and phase, thus they optically interfere. If the scenes for the two exposures are identical, then it is equivalent to one longer exposure and the two reconstructed wavefronts constructively interfere everywhere producing a virtual image of the original scene. However, if the scene changes slightly between the two exposures, by thermal expansion for example, then upon reconstruction the two wavefronts will interfere constructively in some places and destructively at others. Essentially the interference hologram permits the light from an object to optically interfere with light radiated from it during some prior state.

Upon reconstruction, the interference hologram produces the usual holographic three-dimensional virtual image of the original scene, but in addition, superimposed on the virtual image are a series of interference fringes. These appear as dark bands, and depending on the recording geometry they move about the surface of the virtual image as the point of observation shifts. The interference fringes correspond to

destructive interference, hence cancellation, between the two reconstructed wavefronts. The intervening bright zones indicate the constructive interference of the wavefronts. The patterns depicted by the fringes relate directly to the distribution of motions on the surface of the object.

These concepts are visualized in figure 3-1. Consider for the moment just a single point on the deforming surface, indicated in the figure. Suppose its motion between the two holographic exposures is defined by the vector $\vec{\Delta}$. The point scatters the light illuminating it from the laser source in all directions, but focus on only the light traveling from the point to the film plane along the direction of vector $\vec{O}$. The interference hologram will show a fringe at the point, as observed along the vector $\vec{O}$, only if the change in path length is a small odd number of half wavelengths so that the two rays of light destructively interfere. Otherwise, there will be constructive interference. If $\vec{L}$ and $\vec{O}$ are unit vectors in the direction from the point to the laser source and observation point respectively, then the change in path length is given by the left-hand side of equation 3-1.

$$\vec{\Delta} \cdot (\vec{L} + \vec{O}) = \frac{2n - 1}{2} \lambda \qquad (3\text{-}1)$$

In figure 3-1a the geometric relationships between $\vec{\Delta}$, $\vec{L}$, and $\vec{O}$ are configured so that the path-length change is zero because $\vec{\Delta}$ is orthogonal to the vector sum of $\vec{L}$ and $\vec{O}$. However, in figure 3-1b, identical to figure 3-1a except for the observation point, this no

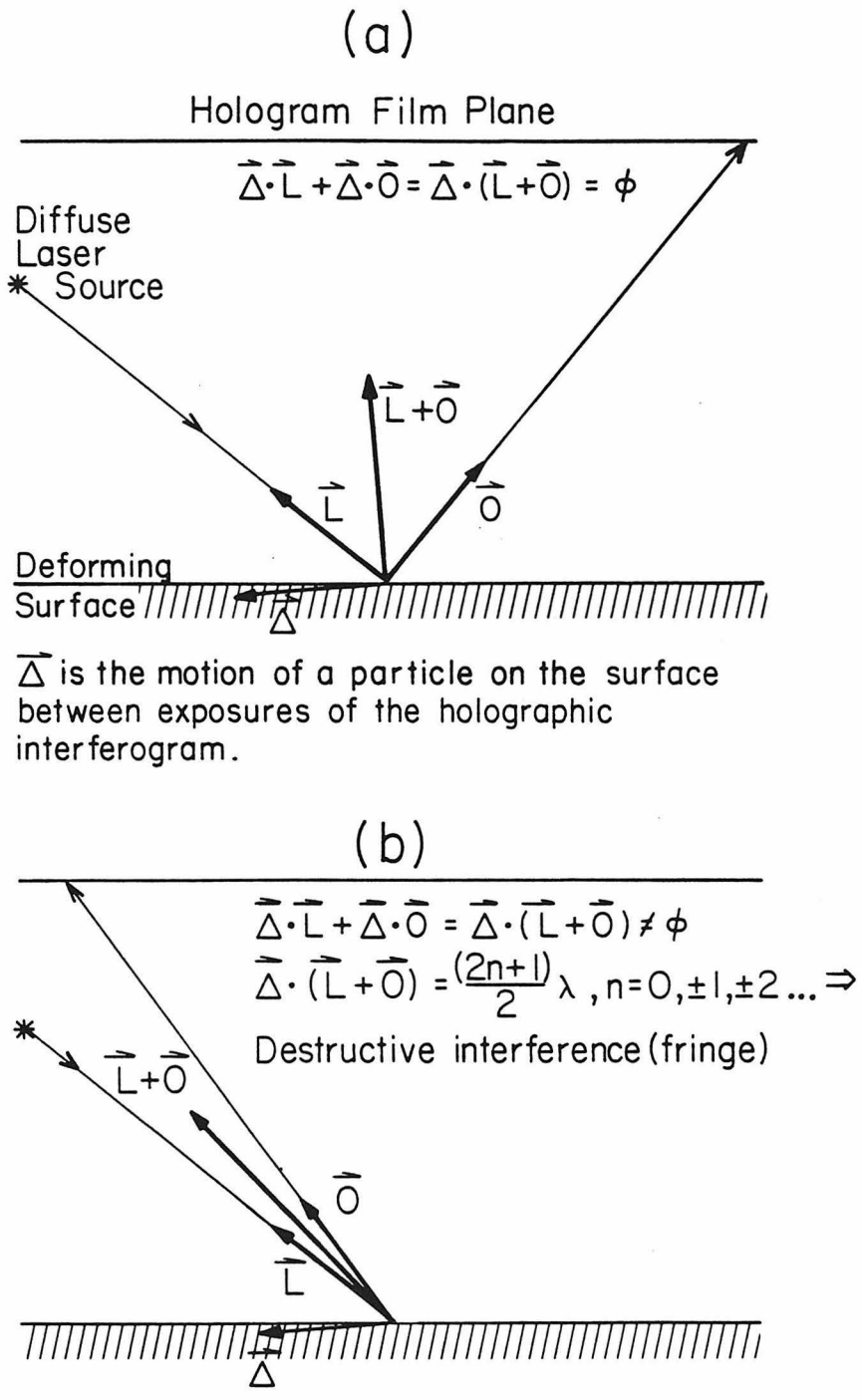

Figure 3-1 Illustrates formation of holographic interference fringes in two-dimensional case. L and O are unit vectors, ϕ represents zero. a) No change in path length due to displacement Δ because Δ is perpendicular to (L+O), hence no fringe. b) Observation points between those shown in a) and b) will produce fringes wherever the change in path length is an odd integral number of half wavelengths.

longer holds. In this two-dimensional example it is clear that as the observation point moves from right to left, the displacement $\vec{\Delta}$ of the point on the surface shortens the path length between the two exposures by increasing amounts. At some point to the left of the observation point in figure 3-1a the first fringe is encountered where the change in path length equals $\lambda/2$. This is the first-order fringe. The second-order fringe occurs where the observation point is such that $\vec{\Delta}$ changes the path length by $3\lambda/2$, and so on. Notice that for a fringe to form it does not matter whether the path length increases or decreases. This introduces a ubiquitous ambiguity in the sign of the displacement $\vec{\Delta}$ as $\vec{\Delta}$ and $-\vec{\Delta}$ have identical impacts on the fringe pattern. Equation 3-1 defines where the fringes occur. Notice also that the scheme is most sensitive if $\vec{\Delta}$ is normal to the surface as it affects both parts of the path with the same sign, and that purely normal motions will produce fringe patterns that are much less sensitive to the position of observation.

An example of the formation of interference fringes in double-exposure holography is shown in figure 3-2. In this case, rather than showing the existence or absence of a fringe at a particular point for many observation points, we show, in the upper part of the figure, a photograph of the reconstructed interference hologram which displays the fringe pattern for the whole surface as seen from one observation point. In the framework of figure 3-1, both $\vec{L}$ and $\vec{O}$ are varying. In this example the scene, a white paper target with an inked 1-cm grid, was displaced precisely .0056 mm to the right between the two exposures.

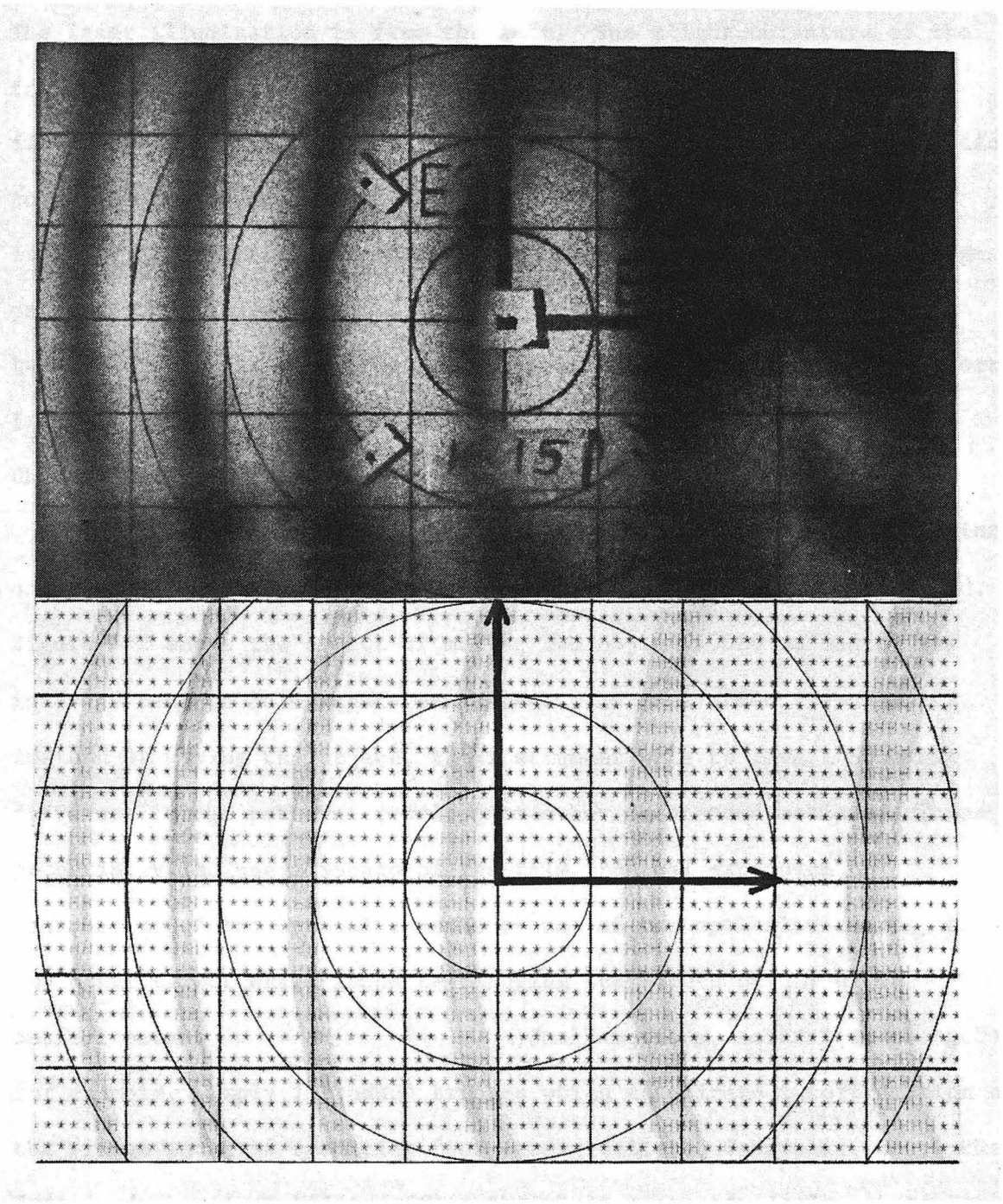

Figure 3-2 The upper figure is a photograph of the holographically reconstructed virtual image of a target surface with a 1-cm ruled grid. Superimposed on the virtual image are approximately linear fringes resulting from a .0056-mm displacement to the right between the two exposures comprising this interference hologram. The lower figure is a computer simulated fringe pattern, for the trial above, which agrees quite well.

The laser illumination is from the left. The slight curvature of the fringes results from using a spherical wave rather than a plane-wave illumination source, and from the spherical rather than plane projection to an observation point near the holographic plate rather than at infinity. The lower half of figure 3-2 is a computer-simulated fringe pattern for the experimental geometry stated above. The agreement between the two is considered excellent. A discussion on how to invert from a recorded fringe pattern to the displacements is left to Chapter 4.

The holographic recording technique imposes most severe constraints on the requirements for mechanical and thermal stability in the field. Figure 3-2 shows the effect of moving the object .0056 mm during the interval between holographic exposures. The same effect results, if instead of moving the object, the instrument were to move. Somewhat different fringe patterns result from other unintended motions. These potentially include slippage of the film, thermal expansion or contraction of the optical chassis or any of the optical elements, or any other effect which leads to changing the length of any of the optical paths. Small motions, several wavelengths for example, simply introduce fringes which complicate interpretation of the fringe patterns resulting from strain relief. Generally, since the fringes due to instability affect the whole scene similarly, these fringes are approximately linear and therefore identifiable.

Larger motions, .01 to .02 mm for example, produce such a high fringe density that the fringes are no longer resolvable. Motions of

this magnitude produce two reconstructed wavefronts that fail to interfere and appear, without fringes, as simply a single-exposure hologram. The two reconstructed virtual images are so similar that one doesn't even observe ghosting. If the motions are less than .1 mm it is hardly enough to observe, particularly with resolution lowered by laser speckle. There is, nevertheless, one benefit from this limitation on holographic interferometry. If the reconstructed interference hologram displays interference fringes, it assures that the requisite stability was maintained. Since the wavelength of the laser illumination is highly stable and well defined, there is really no calibration required for interpreting the data. If the fringes are recorded, they correspond to very specific motions.

Experimental Deployment

The holographic stressmeter operates in the field like a logging tool with the notable exception that it must stop its ascent and lock onto the borehole wall to do its sampling. Figure 3-3 diagrams field deployment of the stressmeter in a vertical borehole. As it is currently configured, the stressmeter is connected to the surface by a 1/4 inch steel cable to support its approxiamate 150 kg weight, a waterproof-jacketed 24-conductor Belden electrical cable to communicate with the control module, and three low-pressure polyethylene tubes to transmit nitrogen for operating the gas-cylinder control mechanisms, coolant, for the drilling operation, and exhaust gas, to maintain constant differential pressure to the gas control system. Notice that

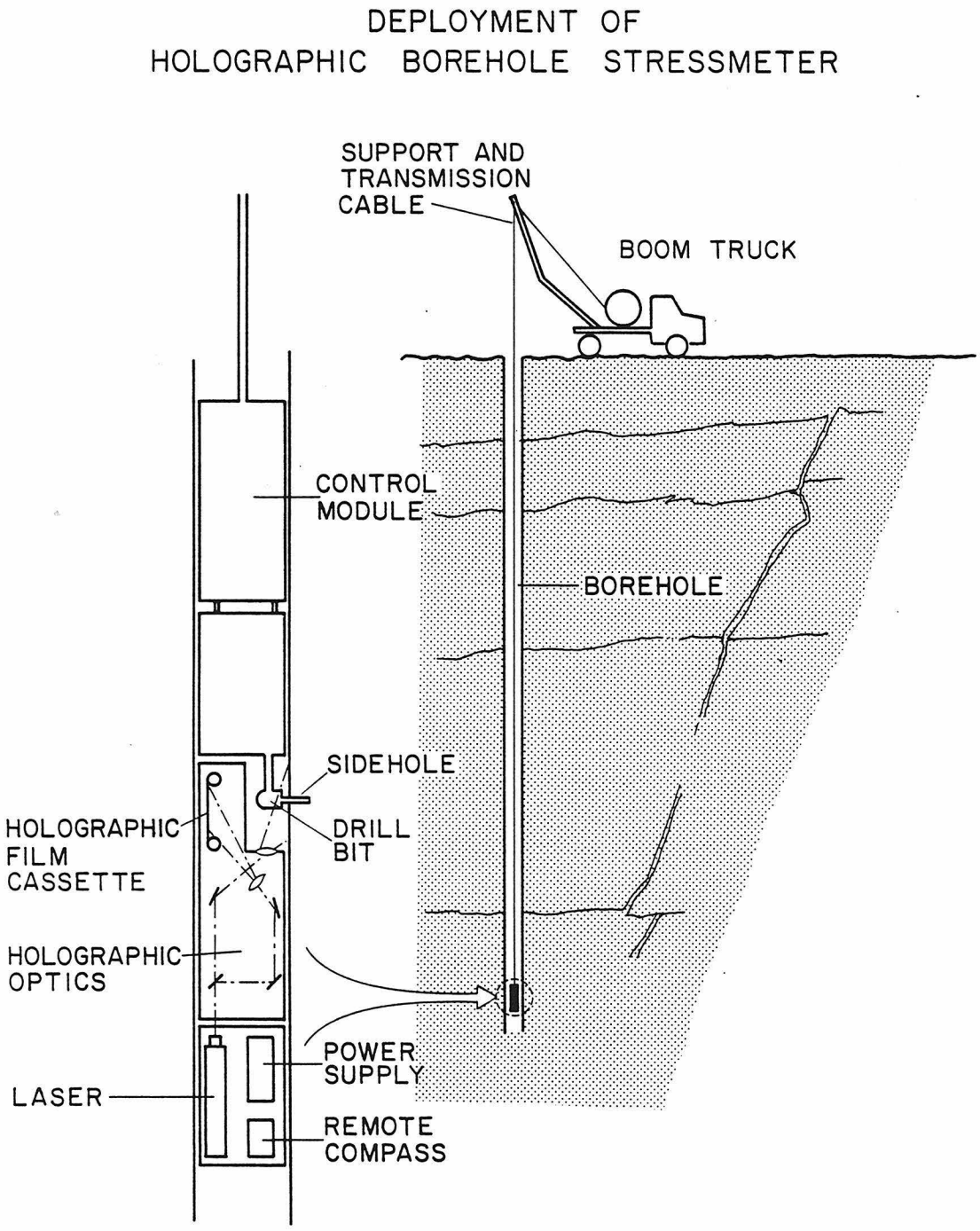

Figure 3-3 Diagram of the components comprising the holographic stressmeter as they are deployed in a vertical borehole and sectional sketch depicting actual field deployment supported only by a truck with a boom and hoist.

only a truck with a hoisting boom and winch is required to tend the instrument at the surface.

The borehole must be uncased, at least 30 cm in diameter to admit the stressmeter, and vary less than 3 cm in diameter to avoid exceeding the 3.8 cm range of the hole-locking mechanism. Certain minimal smoothness is also required for the instrument to move freely into and out of the hole.

The instrument itself is composed of two structurally independent units. The unit entering the hole first is composed of an optics module and a laser and compass module. The upper unit contains the drilling system for drilling the side-core hole and a control module which governs the gas distribution, self-pressurization, and electrical functions and also includes the connections for all of the cables and tubes linking the instrument to the surface. These two units must lock independently to the borehole wall and maintain mechanical isolation to prevent the vibrational energy generated by the drilling procedure, in the interval between exposures during a stress measurement, from disturbing the optics module. Each of these modules is discussed in greater detail below.

The assembled instrument, configured for a vertical hole, is shown in figure 3-4. The experimental deployment at NTS (discussed in Chapter 4) required modifications to operate in a horizontal hole. These changes are described later.

A sequence of three diagrams in figure 3-5 displays a crossectional view of the borehole and inserted stressmeter depicted at each of the

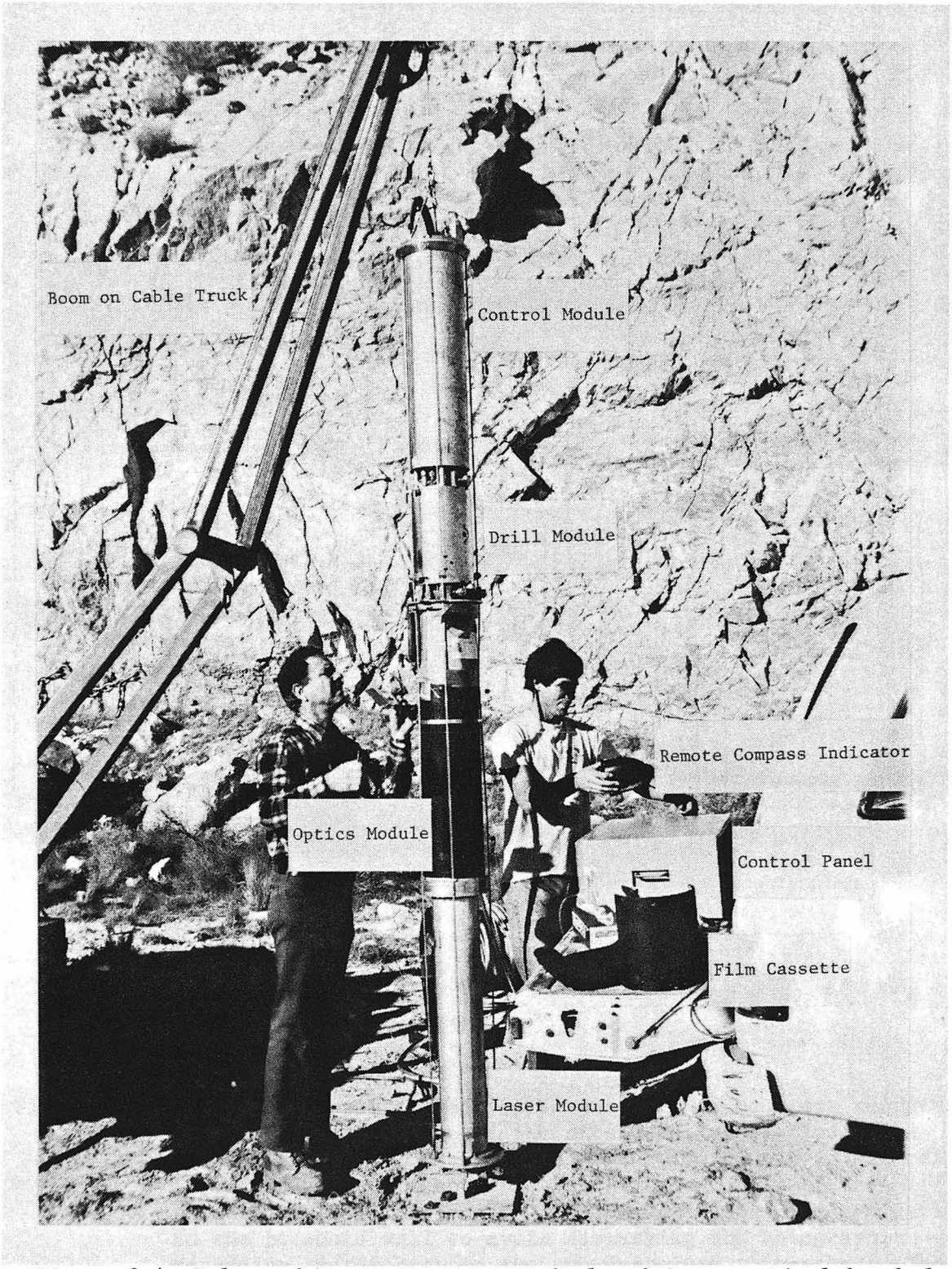

Figure 3-4 Holographic stressmeter as deployed in a vertical borehole. The four modules are paired into two mechanically isolated units to prevent the drilling proceedure from disturbing the stability of the holographic recording system and to introduce flexibility for navigating bends in the borehole.

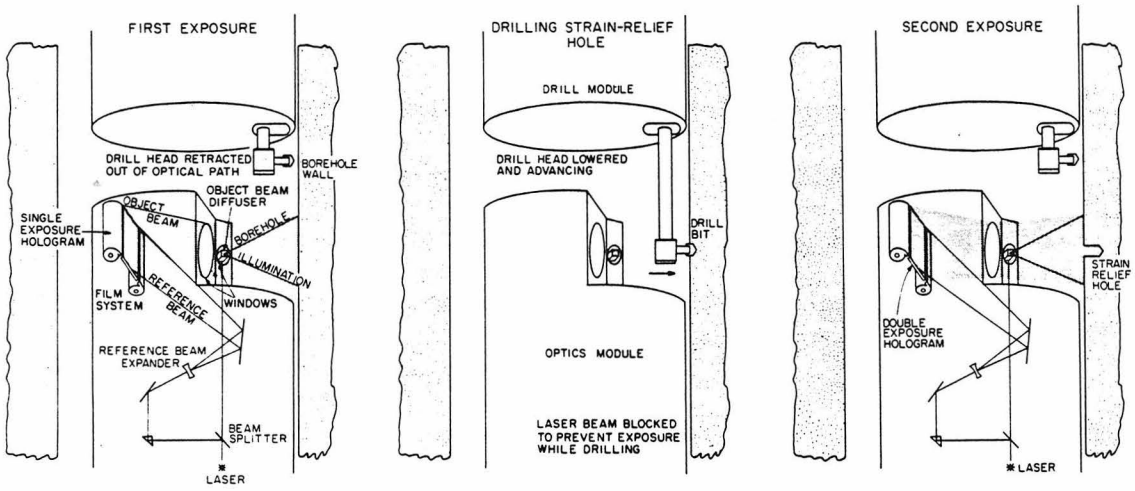

Figure 3-5 Each panel depicts one of a sequence of three steps required to holographically record the strain-relief displacements for one side-core hole. (left) The instrument is securely locked into the borehole and the first exposure of the borehole wall is made. The drill module locks independently to the borehole wall to avoid disturbing the holographic recording system between the two exposures. (center) The drill head extends into the field of view to drill the strain-relieving side-core hole. (right) The drill head retracts out of the field of view to permit the second holographic exposure of the surface, now deformed by the strain-relief hole.

stages required to make a stress measurement. The upper module is the drill module. Beneath it is the optics module which records the interference hologram. The sequence of events starts with the left-most diagram and proceeds to the right.

In the first step, labeled first exposure, both the optics and drill modules are locked independently onto the borehole wall at the desired orientation. The holographic recording film is advanced to expose a fresh length. When everything has stabilized the instrument takes the first exposure of the unperturbed, though previously cleaned borehole wall. The reference beam strikes the film directly. The object beam is diffused by the turning prism and illuminates the borehole wall where it scatters back through the main window to the film. The exposure lasts several seconds.

The middle diagram depicts the instant following the first exposure when the drill head is lowered into position to drill the strain-relief side-core hole in the middle of the field of view. With the drill bit turning and a cuttings removal system (not shown) operating, the drill head advances toward the wall drilling the strain-relief hole to the desired depth. Usually this means drilling to a depth at least the diameter of the side-core hole. The drill then backs out and the drill head is retracted to again permit an unobstructed view of the borehole wall through the main window. The whole drilling procedure takes approximately two minutes.

The right-most diagram shows the second exposure of the interference hologram being made of the borehole wall now with the

side-core hole in it. The side-core hole causes minute relaxing displacements of the borehole surface surrounding the hole, and these are recorded as interference fringes in the interference hologram. Throughout the two-minute drilling interval, shown in the middle diagram, the optics module is kept as motionless as possible to prevent introducing extraneous fringes due to static displacements of the instrument. Ideally, the interference fringes recorded result entirely from the strain-release displacements which we seek to measure. The second exposure is for the same period of time as the first so that the scenes recorded in each exposure are equally represented upon reconstruction. This assures that well-defined interference fringes form on the reconstructed virtual image.

After the second exposure, a single exposure hologram of the side-core hole is recorded to provide a photographic record of the location, possibly aiding in identifying crosscutting fractures or other heterogeneities which might introduce peculiar results. It is also possible to make a double-exposure hologram with an interval of five minutes, for example, between exposures to test the stability of the locking system at the particular site, or to check for time-dependent strain-relief or thermally-induced displacements occurring after the drilling and second exposure are complete. Finally the two modules are unlocked from the borehole and rotated to a new azimuth or moved to another level to start the process over again.

In general we allow the film to stabilize 2 minutes after advancing, which can be simultaneous with repositioning the instrument

for the first hologram at a particular site. The drilling process requires approximately 2 minutes. The exposures each last 5-7 seconds for a double-exposure hologram. Thus the whole measurement of strain relief for one side-core hole consumes about 3 minutes plus positioning time. Recording a single-exposure hologram of the strain-relieved borehole wall consumes an additional 2 minutes.

Stressmeter Components

The stressmeter is comprised of four independent modules physically connected in pairs into two mechanically isolated units attached by external cables. The position of each module in the instrument is shown in figure 3-4. This section describes the function and design of each module.

Laser module. The laser module houses the power supply and laser head (4.5 mw He-Ne laser, Spectra Physics model 135) for the holographic system, shown in the lower-left side of figure 3-6, and the remote-compass transmitter and its power supply (Pioneer Instruments, Bendix Aircraft, purchased surplus). The case is constructed of aluminum and being at the lowest end of the instrument it is the preferred spot for measuring the local magnetic field as it is least disturbed there. Other locations within the instrument are either adjacent to masses of steel or substantial electrical currents. The module is pneumatically isolated from the rest of the stressmeter, which self-pressurizes as ambient fluid pressure increases, so that the

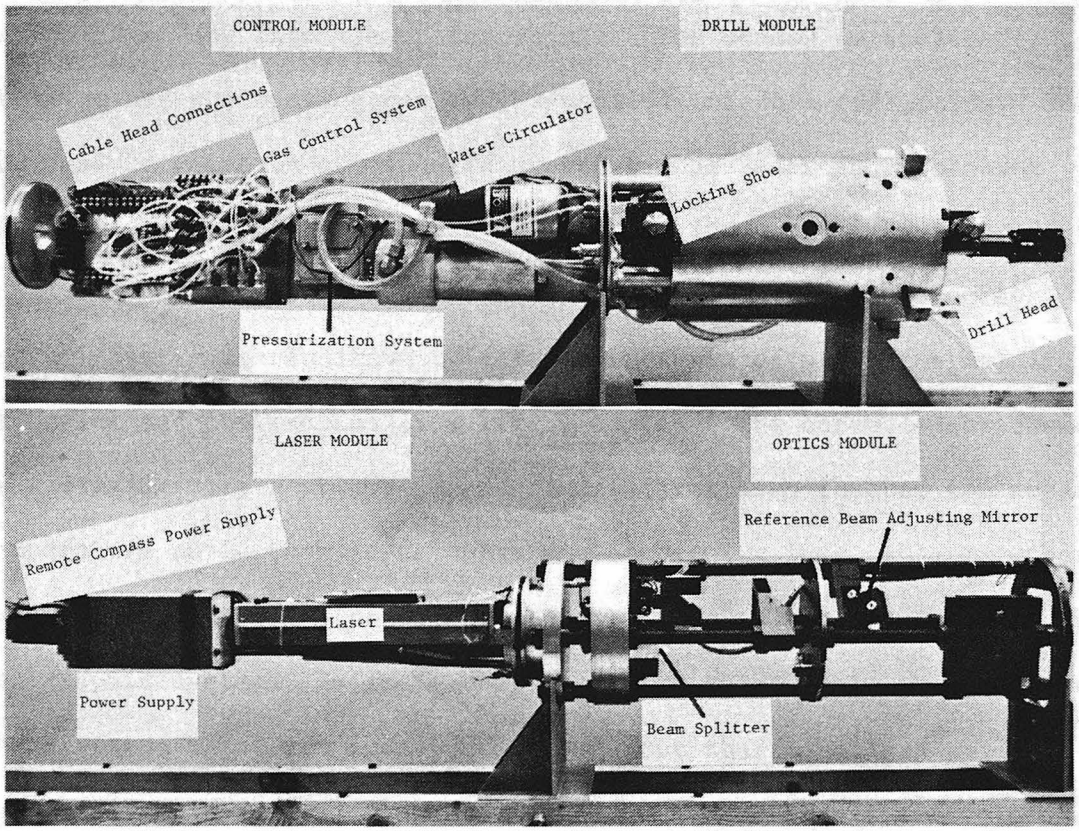

Figure 3-6 Internal views of the stressmeter components.

internal pressure in the laser module can be maintained at one atmosphere to protect the laser tube. The laser beam passes from the laser head through a solenoid-controlled sliding shutter to an inclined, gas-tight window into the optics module. The window is inclined to separate out the beams generated by partial internal reflection. Beside the need to maintain atmospheric pressure, the laser and its power supply represent the principal heat sources in the lower unit, radiating approximately 60 watts as heat. As explained above, the holographic optical system is sensitive to internal motions of which thermal expansion and contraction is a likely source. The borehole environment is thermally very stable so once the optical system reaches the ambient temperature no further adjustments should occur. Thus isolating these two heat sources from the optics chassis improves the stability of the holographic system. As it is only necessary to maintain the relative phase of the reference and object beams, not their absolute phase, for successful holography, small motions of the laser itself are tolerable as they only affect the beam prior to its division at the beam splitter, located safely within the optics module.

Optics module. The laser beam enters the optics module from the laser module and is split by a piece of thick plate glass which yields approximately the right distribution of energy between the reference beam (4 percent) and the object beam (96 percent). The reference beam is routed via a rotary variable attenuator, (continuously variable density neutral filter offering 1-96 percent transmission), to permit

adjustment of the relative intensity of the two beams when they strike the film, to an expanding lens (spaced pair of 8-mm-diameter double-concave lenses with -12 mm focal length). Then the diverging beam is multiply reflected by front-surface mirrors, finally to illuminate the film plane. We omit spatial filters, for cleaning up the laser beam, because of the sensitive and frequent adjustments they require, particularly when shaken and jarred as any logging instrument must be, traveling into and out of a borehole. Instead, we simply try to keep the optical elements clear of dust. This has proven satisfactory, but not ideal.

The object beam is delayed by an adjustable reflection leg and routed to a turning prism. The prism has a ground-glass diffusing surface which expands the beam and transmits it through a second ground-glass diffuser to refine the illumination. The diffused object beam passes through a side window and iluminates the borehole wall (see figure 3-5). The total path lengths of the two beams from the beam splitter to the film plane are adjusted to within 1 cm, substantially less than the variation in each one due to object depth and oblique reference ilumination of the film plane.

The film-transport cassette, shown in figure 3-7, carries two side-by-side rolls of 70 mm holographic film (Agfa-Gevaert Holotest 10E75) up to 10 m in length, rolled in reusable magazines (Hasselblad 70 mm cassette, #51039, Mfg. by Eastman Kodak Co.). The film is pressed by a fabric backing against a glass front plate through which the reference and object beams pass. The advance mechanism is driven by a

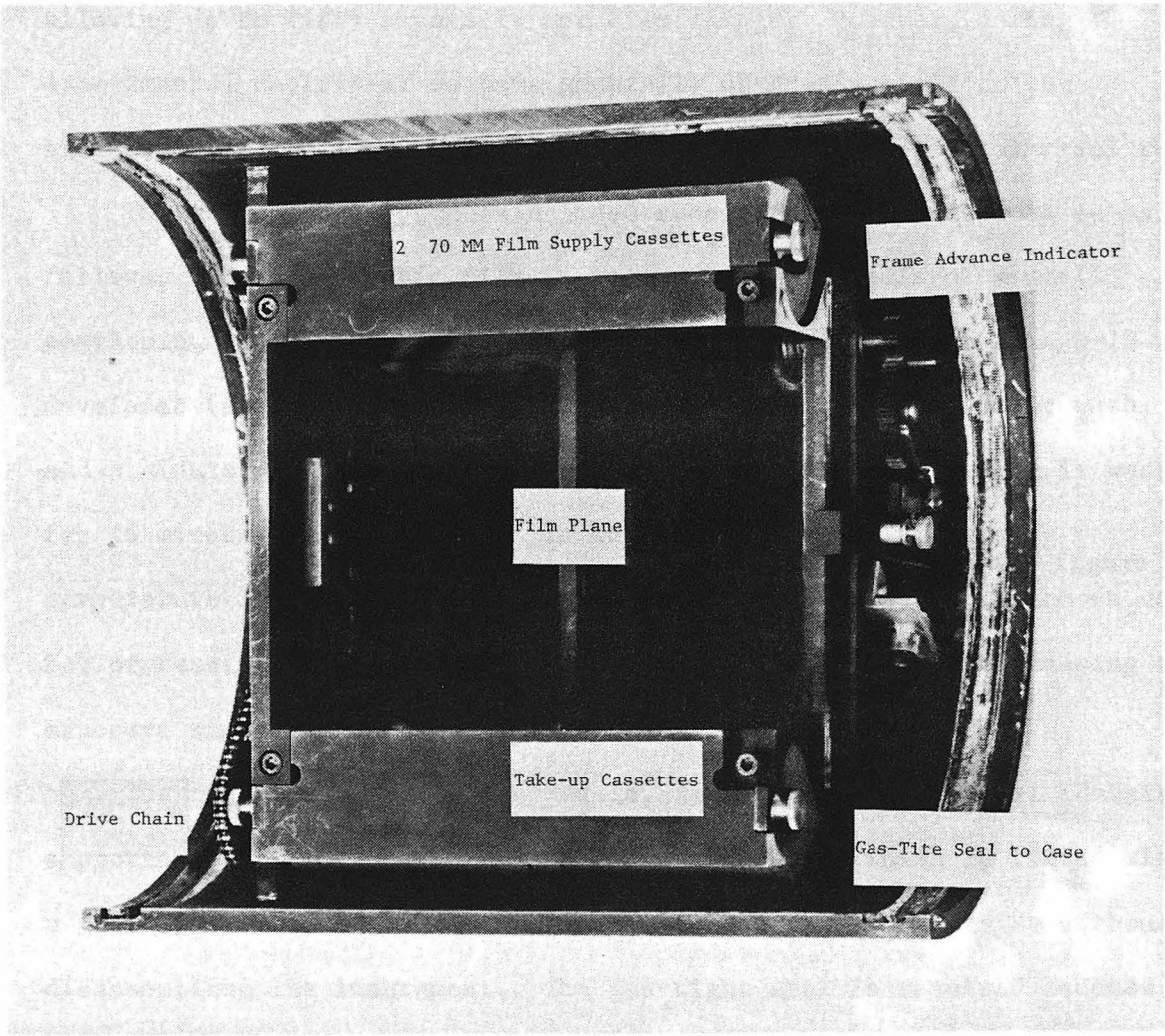

Figure 3-7 Film carrier and advance mechanism. The film carrier positively supports the film between the front glass plate and a fabric backing. The film is advanced by drawing it out of the supply cassettes, across the glass plate, and into the takeup cassettes.

24 VDC gear-head motor and uses about 18 cm of film per exposure, allowing up to fifty exposures per film change. However, during experimental deployment we have generally used only eight to ten exposures for the two or three strain-relief measurements per trial run.

The photographic processing used successfully in this work is as follows. The holographic film is rolled onto the reels of a small developing tank in darkness. It is then processed 5 minutes in D-19 developer (Eastman Kodak Inc.), 1 minute in a circulating-water wash, and 5 minutes in standard Fixer (Eastman Kodak Inc.). Then it is washed for 15 minutes and air dried. In the laboratory the processing temperature is 20° C. The water flowing from U12n.14UG-1/ (see figure 4-3) which we used for processing at NTS, was at 17.5° C. We compensated by increasing the exposure times and used the same processing schedule.

The housing of the optics module, rather than the optical chassis, supports the film cassette, allowing the cassette, which is fitted with a gas-tight seal, to be removed and installed from the outside without disassembling the instrument. The gas-tight seal is required because the optics module is pressurized approximately 6 PSI above ambient pressure to prevent deflection or breakage of the optical windows when operating under fluid pressure in a borehole.

Drill module. Strain relief of the borehole wall by drilling the side-core hole proceeds between the two exposures constituting the interference hologram. Thus the drill module must drill the hole without moving, shaking, or even contacting the optics module, and then

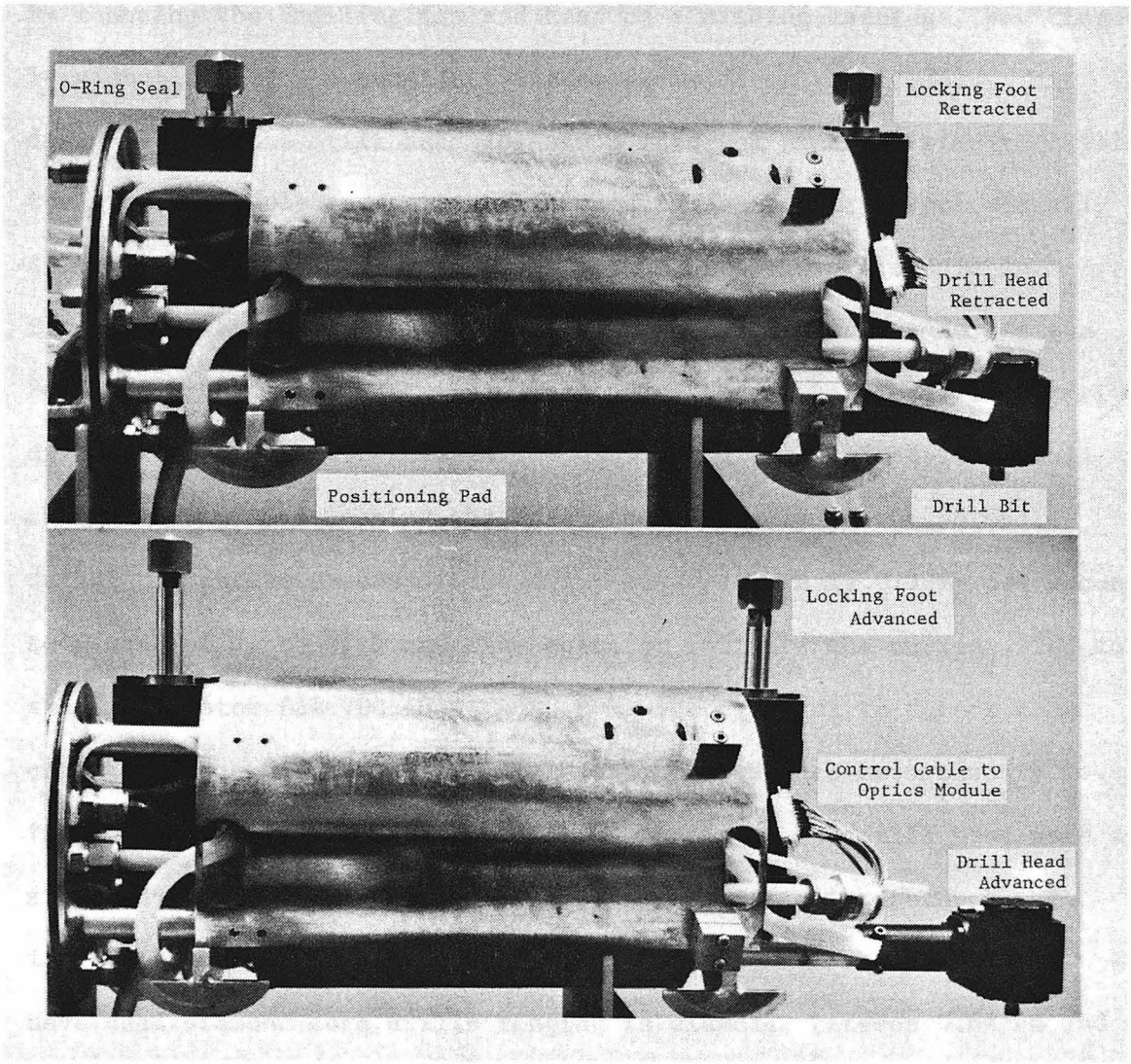

Figure 3-8 The drilling module shown from the side. In the upper view the locking pads and drill head are retracted. In the lower view both are extended.

withdraw out of the way to permit the second exposure. This is achieved by mounting the drilling arm and head on a sliding carriage, positioned by a double-acting pneumatic cylinder (Schmidt et al., 1974). This design allows the drill head to extend into the field of view to drill the side-core hole and retract at other times when it is not actually drilling. The top and bottom photographs of the drill module in figure 3-8 show these two positions of the drill head. A reversible 24 VDC gearhead motor driving a lead screw feeds the electrically-driven drill bit into the borehole wall by advancing the whole drill module chassis out of its housing which is secured firmly to the borehole during the entire process. The drill advance rate is 0.3 mm per second to a maximum depth of 3 cm. The operator monitors the current flow to the drill motor (24 VDC, 3 A, 4000 RPM without load) to detect the cutting torque and can arrest or reverse the advance as necessary to insure the drill cuts properly without binding. The drill head uses a sintered-diamond coring bit, cooled by a flow of water through the inside of the bit, simultaneously flushing away the drill cuttings. We have used diamond core drills ranging in diameter between 0.64 cm and 1.59 cm without other adjustments. We describe below some special modifications to this system for our deployment in a horizontal borehole at NTS.

Control module. This, the top-most module, shown in figure 3-6, serves as the stressmeter's nerve center. To permit easy disassembly the plumbing and electrical links to the surface terminate at the control module with watertight connectors. The 24 conductor electrical cable is potted through a gas-tight bracket which attaches to the control module case with an O-ring seal, making the connection gastight. The electrical contacts are made inside the module with a Bendix multi-connector plug and socket. The three tubes fasten to Swagelok bulkhead connectors mounted on the end of the control module with O-ring seals. The module contains all of the interconnections between the various modules and to the surface, including both gas and electric lines, and the rack of solenoid gas valves (Clippard Minimatic 3-way valves, #EVO-3) which control the gas flow to the pneumatic cylinders used in the hole-locking mechanisms and for positioning the drill head. Solenoid valves to control the drill-cooling fluid as well as a circulation system (Flojet model 2000 Duplex Diaphragm pump and filter housing with stock disposable pleated-paper water-filter element), to filter the fluid in the vicinity of the side-core hole (water-filled hole), or wash the borehole surface (dry hole) as needed, also reside in the control module, as does the differential pressure switch (adjustable 6-75 PSID, Custom Component Switch, model 604D2), which regulates the self-pressurization of the instrument to 6 PSI over the ambient external pressure. Two 10 PSI gas check valves allow depressurization and protect against overpressurizing the instrument. The top of the control module provides connections for the steel support cable and metal

tubing, used to orient the instrument in shallow applications.

Locking mechanism. The two structurally independent units each employ similar hole-locking mechanisms. These can be found in figures 3-4, 3-6, and 3-8. At each end of each unit two positioning pads, on the side facing the borehole wall to be sampled, locate the instrument against the surface of the borehole. Opposite the pads are a series of double-acting pneumatic cylinders (1.5-2.0" bore, 1.5" stroke, .625" shaft by Lynair Inc.), with pointed steel feet which extend under 100 PSI gas pressure against the wall, pushing the ends of each instrument unit against the positioning pads with a force between 800 and 1500 nt. This is more than sufficient force to support the instrument vertically in a dry hole. We have demonstrated that it is also adequate to maintain the stability necessary for holographic interferometry encompassing the drilling process.

Modifications for NTS experiments. To operate in the horizontal borehole provided for us at NTS, the stressmeter required some modifications to the design described above. Sliding its weight horizontally over the rock surface posed two serious problems. The first was simply the difficulty of moving the instrument. The second involved optical alignment difficulties due to the violence associated with positioning the instrument in the borehole. We installed steel ball casters to permit rolling the instrument, however, that limited it to facing only one orientation in the borehole.

Isolating the optics module proved more difficult in the horizontal borehole. We replaced the external cables with a nylon-webbed strap to electrically isolate the two aluminum housings, allowing us to determine contact between the units by electrical current flow between them. Conductive water flowing in the bottom 2 cm of the borehole at 50 l/m complicated this approach, but did allow us to determine if the units were touching and did not generate enough vibration to interfere with the interference holography. Thus we could observe continuously during the experiment sequence to determine if the drill module might be disrupting the stability of the optics.

Drilling with the sintered-diamond core drill also proved impossible in the ash-fall tuff at the tunnel site. We determined experimentally in the borehole that the water used to cool the core drill and remove the cuttings was reacting with the rock and causing the surface to deform to a greater extent than the deformations associated with strain relief. We suspect this was due to a component of montmorillonite clay in the tuff which swells as it readily absorbs water. Replacing the core-drill bit with a carbide-tipped spade drill and reducing the speed of rotation to 600 RPM permitted drilling the tuff without any coolant, thus eliminating the problem. However, a new vacuum system had to be installed to remove the drilling debris so it would not litter the surrounding wall preventing the interference holography from recording the displacements. We used a small pressure foot surrounding the carbide drill bit and pressing against the borehole wall to draw up the cuttings, depicted in figure 3-9. They were then

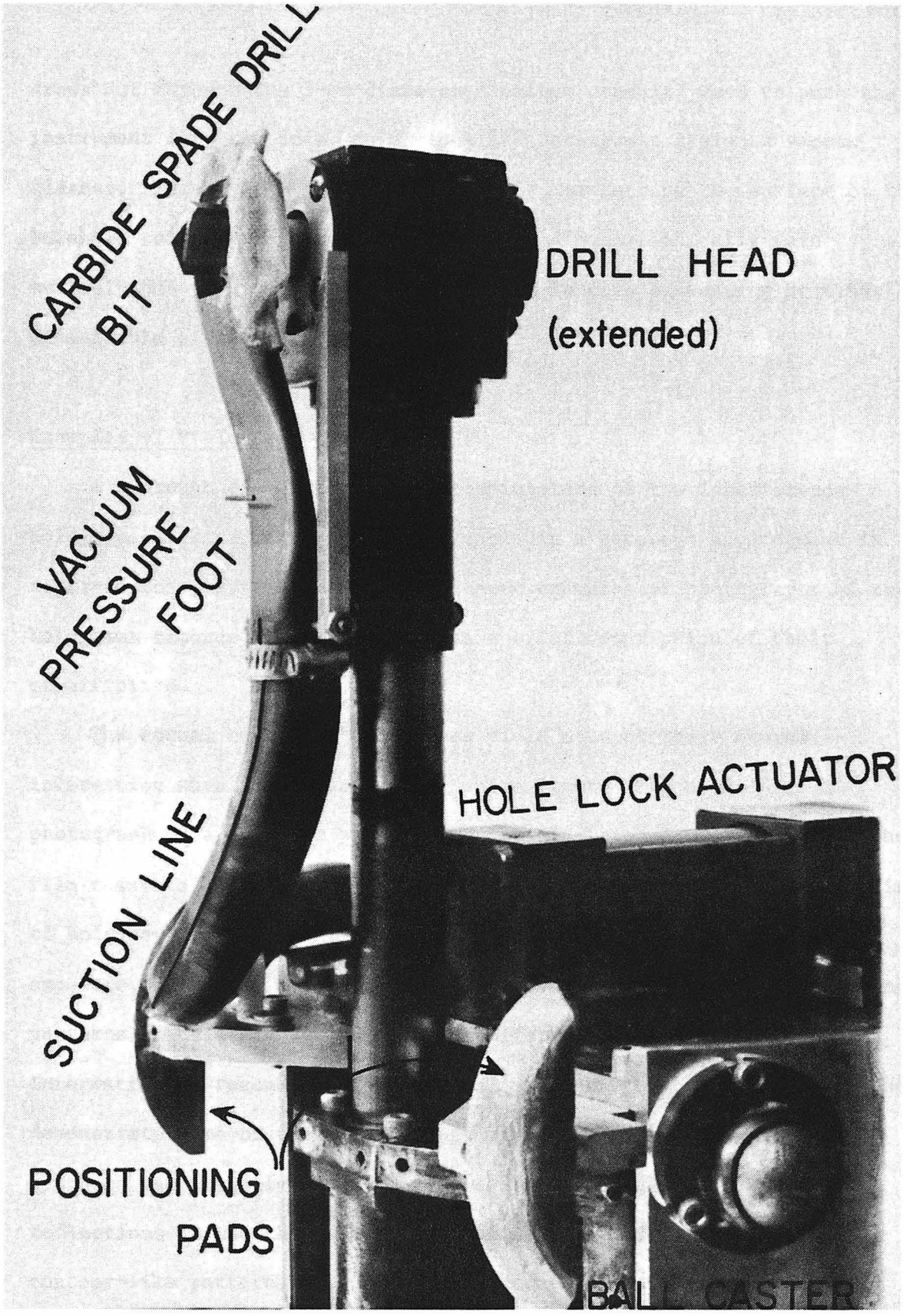

Figure 3-9 Drill module modified for deployment at NTS.

drawn out through the 5-cm diameter aluminum conduit, used to push the instrument into the hole, to a stock 1/2 horsepower canister vacuum cleaner. This system worked successfully, protecting the surface of the borehole so that the displacements recorded holographically were entirely due to strain-relief rather than induced by wetting or other undesirable effects.

Examples of Field Data

A thorough description and interpretation of the interference holograms obtained from the NTS borehole in a stressed environment is reserved for Chapter 4. Here we present examples of photographs of the holograms recorded in the field with a brief description of their significance.

The actual holograms themselves yield none of their stored information when illuminated under white light. Figure 3-10 is a photograph of a hologram produced in the NTS borehole U12n.14UG-1. The film cassette carries two side-by-side rolls of 70 mm film so this pair of holographic films represents all of the data recorded in this exposure. All that can be observed is several superimposed interference patterns. These are not even the interference patterns bearing the information to reconstruct the virtual image of the borehole, but rather demonstrate some of the shortcomings of the design of the recording system. The slightly curved horizontal lines originate as internal reflections in the thin glass front plate of the film holder. The contour-like patterns are from interference generated across the thin

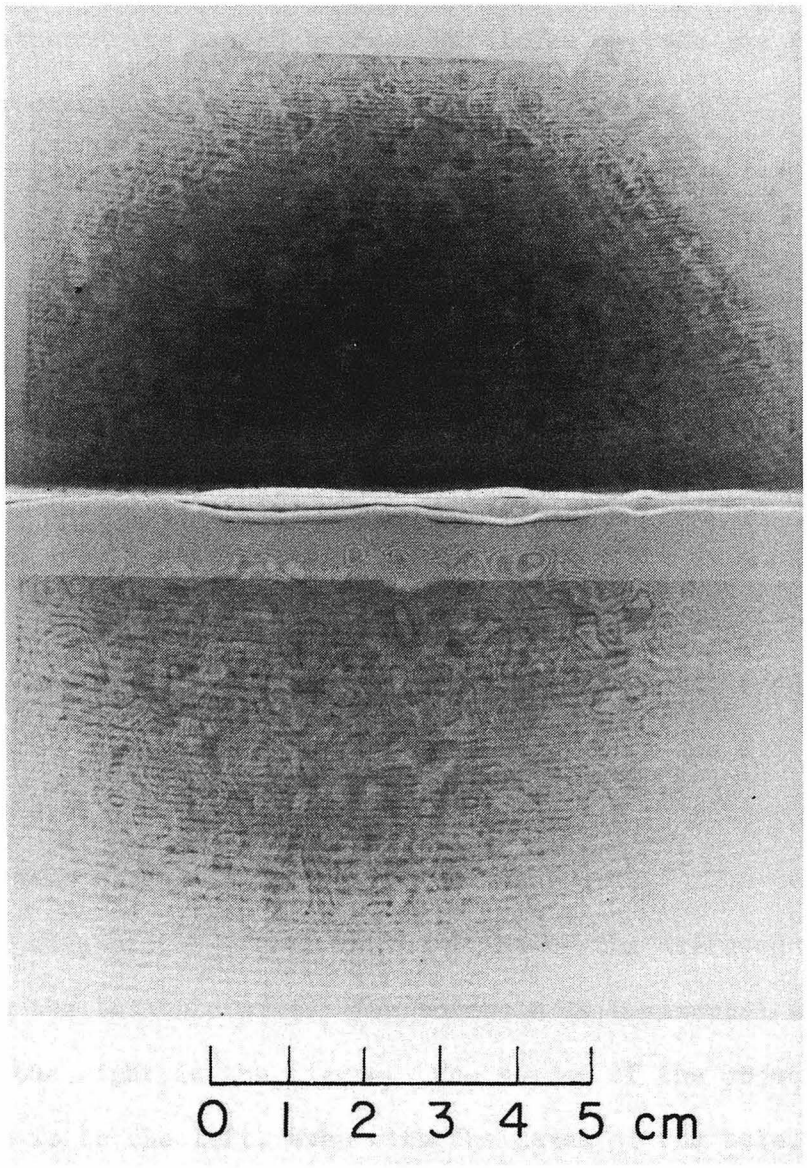

Figure 3-10 Two side-by-side processed 70-mm holograms, illuminated here in white light, comprise the total data recorded in a normal stress measurement.

air space between the film and front glass plate. And some of the remaining patterns are caused by dust particles on both the recording and reconstructing optical elements.

In reconstructing the holograms recorded with the stressmeter we employ a stronger laser than the one contained in the optics module, to produce a brighter image. The reconstruction laser (Spectra Physics He-Ne laser, model 125, operating at 17 mw) and optics are configured to produce a wavefront similar to the reference wave in the stressmeter optical system. Upon reconstruction of one of the two films recorded for each exposure, a single-exposure hologram appears as photographed in figure 3-11. It is a simple hologram of the borehole wall rock which is composed of bedded tuffs of the Miocene Tunnel bed subunit 4H. The hole centered in the picture is a strain-relief hole that was drilled prior to this exposure. The curved shadow at the top of the figure is the edge of the main window in the optics module housing. The curved shadow at the lower edge of the figure is the limit of the diffused object beam illuminating the borehole wall. The borehole is horizontal, so up in the earth is to the right in the figure. The source of the object beam illumination is to the left, even with the level of the hole, as can be seen by the pattern of the shadow in the hole. The surface is evidently fairly smooth. Much greater detail is found by examining the actual reconstructed hologram directly than from a photograph, but even from this reproduction based on a photograph one can identify individual grains, minor chips spalled off the surface at the edge of the side-core hole which obviously cannot produce fringes, and one can judge crudely

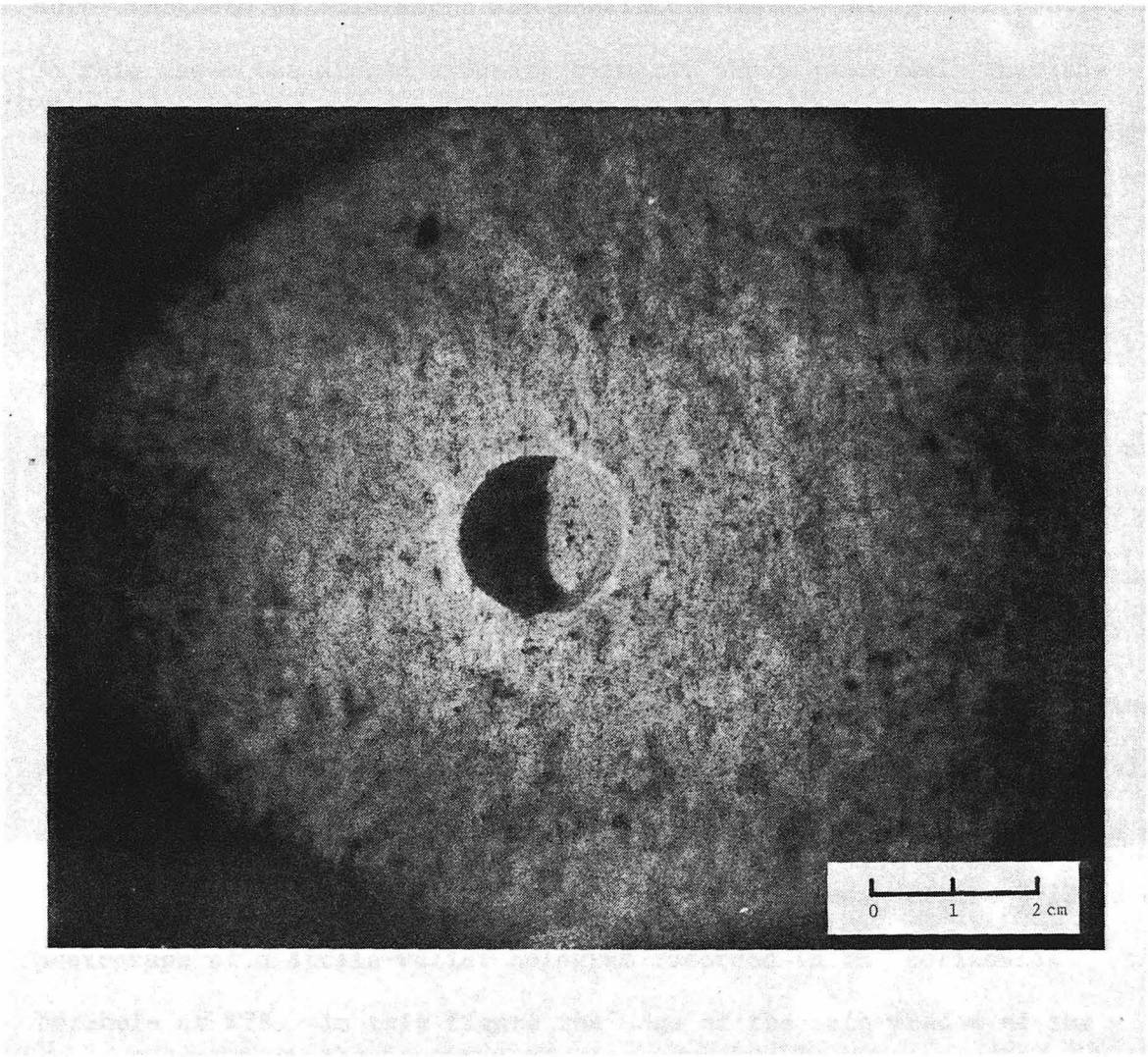

Figure 3-11 Photographic print of the holographically reconstructed virtual image from a single-exposure hologram of the borehole wall after drilling a side-core hole.

the depth of the hole. The actual reconstructed virtual image shows the same parallax that the real hole would display, so accurate determinations of hole depth are possible from the hologram directly. In this case, the single exposure hologram shows quite well that the surface is fairly homogeneous, without crosscutting fractures or bedding planes visible, features which might distort the stress field.

An interference hologram that encompasses the drilling of a strain-relief hole in a stressed borehole wall will display fringes corresponding to the displacement which occurred between the two exposures. It is quite difficult to take a sharp photograph of such a hologram because the fringes move depending on the observation point. With a finite-aperature camera lens the fringes will not have a distinct focal plane so it is difficult to photograph sharp images of the interference fringes. Our efforts at photographing strain-relief fringe patterns make disappointing comparisons to what an observer can actually see in a reconstructed interference hologram; however, it is possible to reproduce the photographic images, not the holograms. Figure 3-12 is a photograph of a strain-relief hologram recorded in the horizontal borehole at NTS. In this figure the edge of the main window of the optics module is better delineated, forming the semicircle at the top and sides of the image, than it is in figure 3-11. Notice that the side-core hole, indicated by the dashed circle, is barely visible and is also just visible in the reconstructed hologram. This occurs for the area of the hole because for this region only, the two exposures are of completely different scenes. In the first exposure the original surface

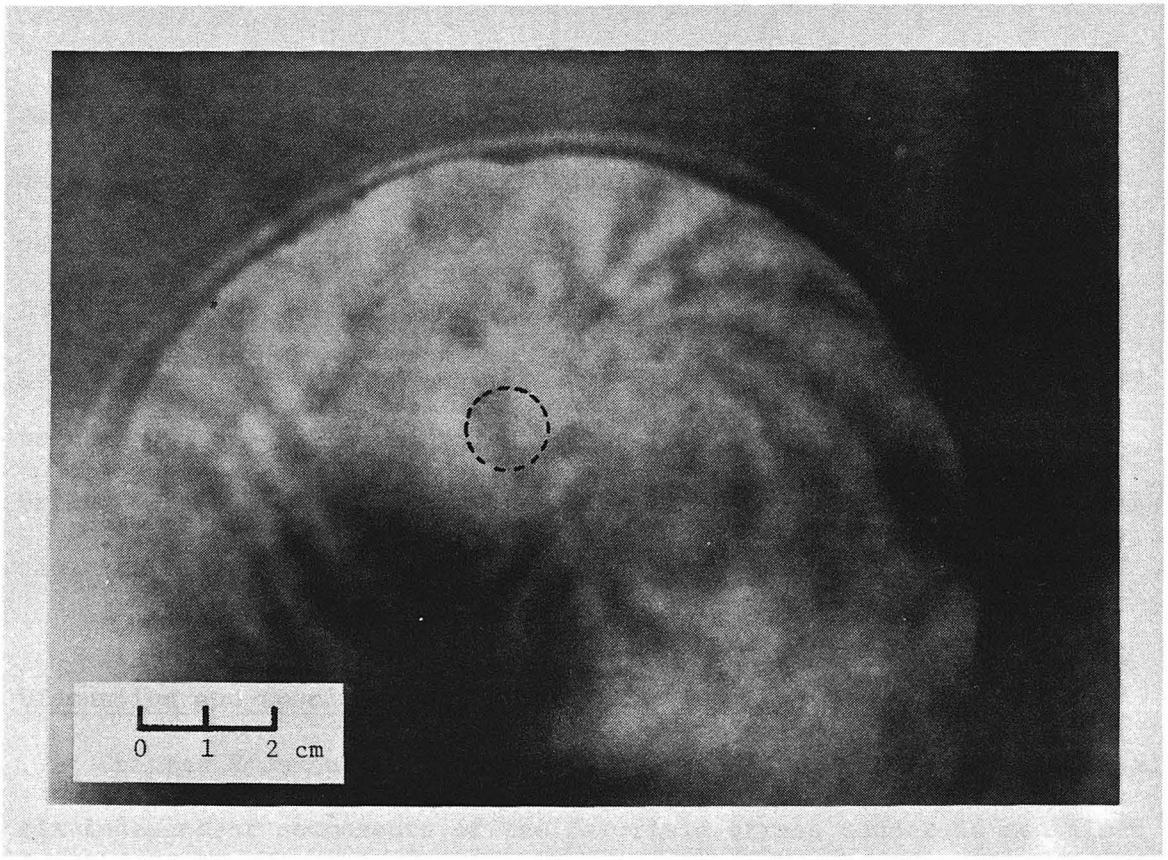

Figure 3-12 Two-lobed pattern of strain-relief fringes obtained in an interference hologram recording the displacements resulting from drilling a 1.3-cm-diameter side-core hole, 0.9 cm deep into the tuff lining the U12n.14UG-1 borehole. This pattern recurs in the interference holograms from several other trials conducted within one meter from this site.

was intact, while the hole existed during the second exposure. Upon reconstruction the two different virtual images obscure each other. Recording the dark lobed bands (the strain-relief fringes displayed radiating from the side-core hole), indicates that in this experiment adequate stability was maintained during the drilling. The lobed pattern is characteristic of symmetric motions directed toward (or away from) the side-core hole and results from the interaction of the geometry of the components of the holographic recording system and the pattern of the displacements on the surface. Interpretation of this fringe pattern in terms of surface displacements and the implied stress field is left to Chapter 4.

Discussion and Conclusions

Chapter 2 demonstrates that sufficient information to determine all six independent components of the far-field stress tensor is contained in nine plane stress components acting at the borehole surface, three each at three specific azimuths. This chapter describes how the holographic stressmeter records the strain-relief displacements at the borehole wall in terms of interference fringes on the reconstructed virtual image. Chapter 4 shows how the interference fringes from the holographic record of the strain-relief motions can be interpreted to discover what the actual displacements are and how they relate to the stresses acting at the borehole wall. Once the stresses at the borehole wall are known at the three required azimuths the far-field stress tensor, the object sought, can be determined. Consequently, a complete

determination of the far-field stress tensor requires conducting the measurement described above three times at three specific azimuths around the borehole.

A complete determination of the stress field by measuring the strain-relief displacements with the holographic stressmeter at three azimuths around a borehole has so far never been attempted. The reason it has never been attempted is that a horizontal borehole, such as U12n.14UG-1, where the successful strain-relief interference fringes were obtained, poses special deployment problems. The most serious of these is the ability to securely lock the two instrument units to the borehole wall. In a vertical orientation the weight of the instrument causes it to hang parallel to the borehole so that actuating the hole-locking mechanisms only shifts the instrument to the side until its positioning pads contact the borehole wall and properly align the two units. In the horizontal orientation the present field prototype of the holographic stressmeter becomes very heavy and clumsy. Its substantial weight tends to make it bind on the lower positioning pad and locking foot without ever aligning properly against the desired face of the borehole wall. If it fails to lock with both positioning pads under pressure the modules are much less mechanically stable. Furthermore, spaced away from the borehole wall, the 3-cm depth range of the drill advance mechanism is exhausted before it begins to cut into the wall and drill the strain-relieving hole.

Facing the instrument to drill directly down would work except for the small river (50 l/m) flowing out of U12n.14UG-1. Our solution was

to design a carriage with ball casters which permitted the instrument to roll, and positioned it to face the right horizon sufficiently snugly that it could successfully lock to the borehole in this single orientation. This proved adequate to conduct strain-relief measurements at this orientation only. Six were done successfully at various positions along the borehole, obtaining similar patterns of strain-relief fringes to those seen in figure 3-12. However, of the six, only in the case shown in figure 3-12 were the strain-relief fringes bold enough to photograph. In this particular case the side-core hole was drilled only 0.9 cm deep. The experiments with deeper side-core holes produced a greater density of finer fringes, presumably resulting from larger strain-relief displacements, which we could not photograph adequately for reproduction. We believe these successful experimental deployments, even if confined to a single azimuth in the borehole, demonstrate that the holographic recording of strain-relief displacements due to drilling a side-core hole is viable in the field borehole environment. This conclusion will be further substantiated in Chapter 4 where we analyze the interference fringe patterns in terms of reasonable values of stress.

Clearly the holographic stressmeter must be deployed at the several required azimuths to make a complete determination of the in-situ stress tensor to demonstrate whether this approach to measuring in-situ stress will work in a reliable and unambiguous way. Ideally these tests should be conducted in a region with a well-characterized stress field such as the tunnels at NTS. Nevertheless, the developments to date suggest that

the approach promises to be highly successful. If the stressmeter can measure the three stresses acting at the borehole wall in one orientation, it is but a modest step to deploy it at three different orientations.

CHAPTER 4

Experiments at the Nevada Test Site: Data and Interpretation

Introduction

We undertook this research to demonstrate that the interference holographic technique, upon which the holographic stressmeter is founded, is a viable approach for measuring in-situ stress. The previous chapter shows that the field prototype developed in the course of this project actually performs in the rugged borehole environment according to the underlying theory and expectations, proving that it is possible to make the desired measurements. In this chapter we intend to demonstrate that the data obtained during experimental deployment of the holographic stressmeter at the Nevada Test Site (NTS) represent, in fact, a measurement of stress and not some poorly-understood failure of the experimental technique. We cannot fully prove the assertion that the stressmeter measures the complete state of stress because the deployment required to determine the complete state of stress has not yet been attempted. However, if we can argue convincingly that the data resulting from the measurements we have made yield a reasonable determination of the components of stress which should theoretically be ascertainable from those measurements, then by logical extension to the case where complete measurements are made, we can confirm the holographic stressmeter as a valid approach to measuring the complete

state of in-situ stress. Unfortunately, for a variety of reasons to be discussed, mostly a consequence of shortcomings of the experimental deployments to date, we will fall somewhat short of this goal. Nevertheless, based on the data and interpretation in the discussion to follow, we conclude that our experimental deployments do substantiate the holographic stressmeter as a promising method for determining in-situ stress, and that the steps ultimately required to prove its performance, while significant, will be readily achieved. In addition, by modelling the data expected for a variety of stress states we show what kinds of stress states we anticipate distinguishing with high-quality data obtained using the measurement technique employed by the holographic stressmeter.

In this chapter we discuss the experimental deployment in a borehole drilled from a tunnel at NTS and present examples of the resulting data. Then we explore approaches to interpreting and modelling the recorded holographic data. Specifically, we use the analog of a stressed, infinite, elastic plate containing a through-going hole to calculate the displacements resulting from drilling the strain-relieving side-core hole into the borehole wall. Using this model to calculate the displacements we generate synthetic interference fringe patterns to compare to the patterns observed in the recorded interference holograms, in light of the expected values of in-situ stress based on other measurements of in-situ stress in the vicinity of our experimental deployment. We consider the issue of the instrument's ultimate sensitivity and alternate approaches to the quantification and

interpretation of the data it records. We also introduce the results of related laboratory experiments to explore the possibility of unanticipated effects interfering with the stress measurements, and discuss the expected impact on the holographic stressmeter's measurements in situations where peculiar rock properties, such as residual stress, are important.

Site Description

All of the successful efforts to obtain strain-relief interference fringes resulting from drilling a side-core hole into the wall of a borehole were conducted in a borehole in n-tunnel at NTS. N-tunnel is carved several kilometers into the thick section of volcanic, ash-fall tuffs of Rainier Mesa, Nye County, Nevada (Gibbons et al., 1963). The location of Rainier Mesa is indicated in figure 4-1 along with the most significant young tectonic features.

Rainier Mesa lies in the middle of the Basin and Range at the southern end of the Belted Range. The normal fault bounding the western edge of the range indicates more than 600 m displacement in the Tertiary (Cornwall, 1972). The fault, shown in figure 4-1, strikes between N 20^{o} E at the southern end to north-south at the northern end. It is probably the best geologic evidence of recent tectonic processes which might reflect or influence the stress field existing today at Rainier Mesa.

Almost one kilometer of Tertiary ash-fall and occasionally welded siliceous volcanic tuffs, lying unconformably on deformed Precambrian

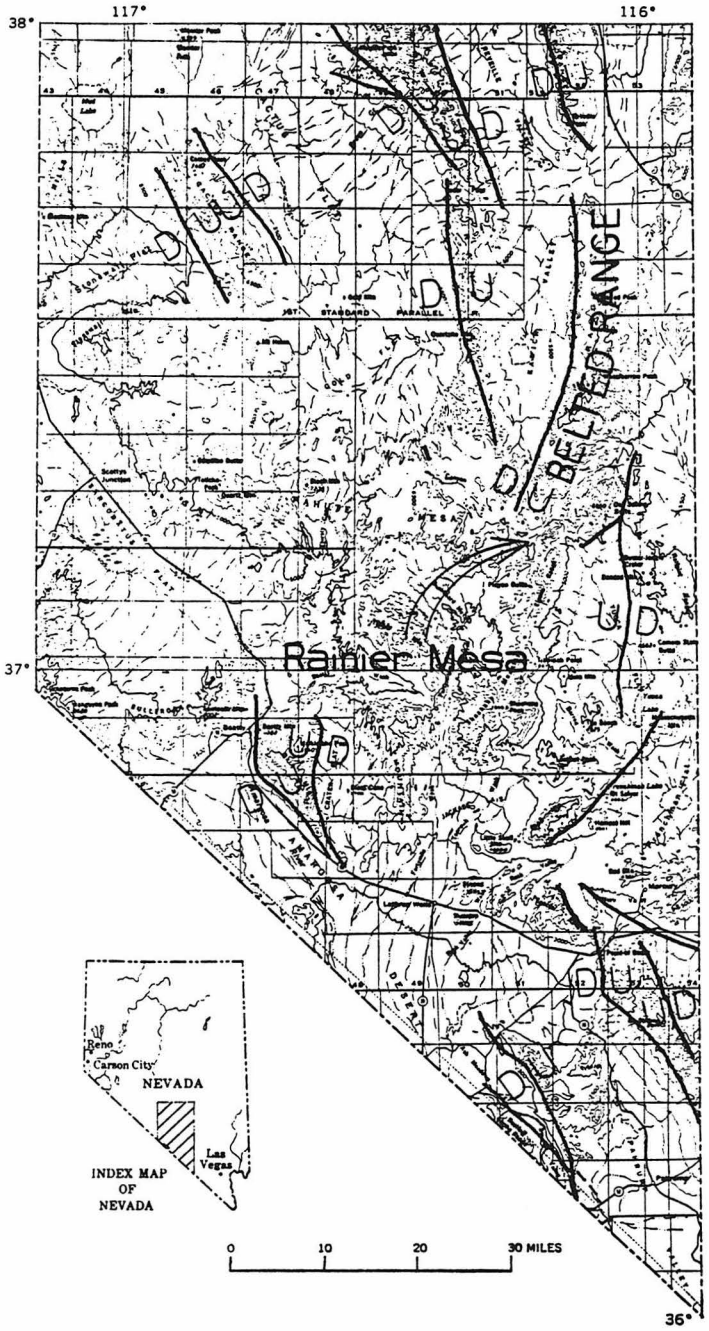

Figure 4-1 Index map of southern Nye County, Nevada showing faults active during the Tertiary. (From Cornwall, 1972.)

and Paleozoic basement, compose Rainier Mesa. The tuffs are predominantly rhyolitic, and mostly zeolitized, with a locally-variable minor component altered to montmorillonite clays. The tuff beds are gently folded into a northeast trending syncline in the vicinity of n-tunnel (Gibbons et al., 1963; Cornwall, 1972; Ege et al., 1980).

Figure 4-2 depicts a crossection of Rainier Mesa (no vertical exaggeration), through n-tunnel and our experiment site. Approximately 375 m of bedded volcanic tuffs overlie the tunnel level. Integrating the average bulk density, estimated at 1.85 g/cm^3 (Ege et al., 1980), overlying the experiment site yields an expected vertical stress of 68 bars resulting from the lithostatic load. It was with this figure in mind that we decided to design the holographic stressmeter carriage to drill in the horizontal direction, as the stress concentration factor of between 2 and 3 guaranteed a substantial stress component at the borehole wall to measure.

The borehole in which we deployed the holographic stressmeter, U12n.14UG-1, is indicated on a map of n-tunnel, shown in figure 4-3. The borehole is drilled 638 m, at a diameter of approximately 8 cm, inclined slightly to the horizontal and striking S 55^o W. The first 15 m are reamed out to 30 cm diameter to accommodate the stressmeter. It is drilled at the center of the end of a small alcove, U12n.14 main, adjacent to the U12n.10 bypass drift where Fairer and Townsend (1979) conducted extensive lithologic and physical-properties studies of the exposed tuff units.

The tuff encountered over the section of U12n.14UG-1 in which we

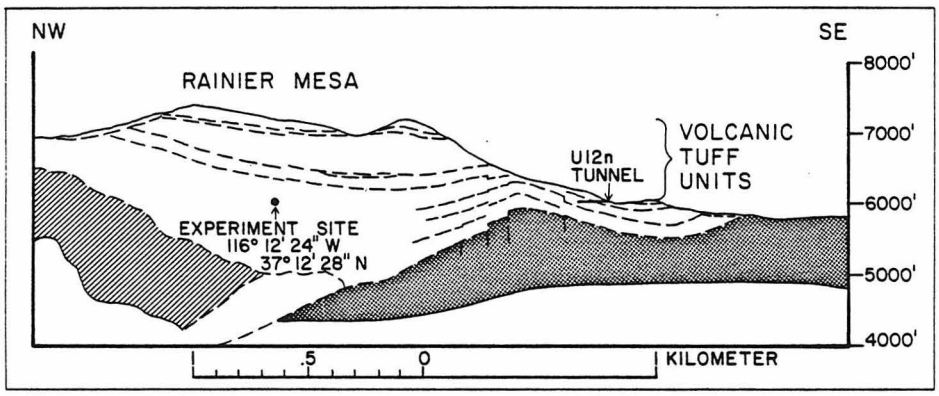

Figure 4-2 Northwest to southeast geologic crossection of Rainier Mesa, in the vicinity of n-tunnel. (After Gibbons et al., 1963.)

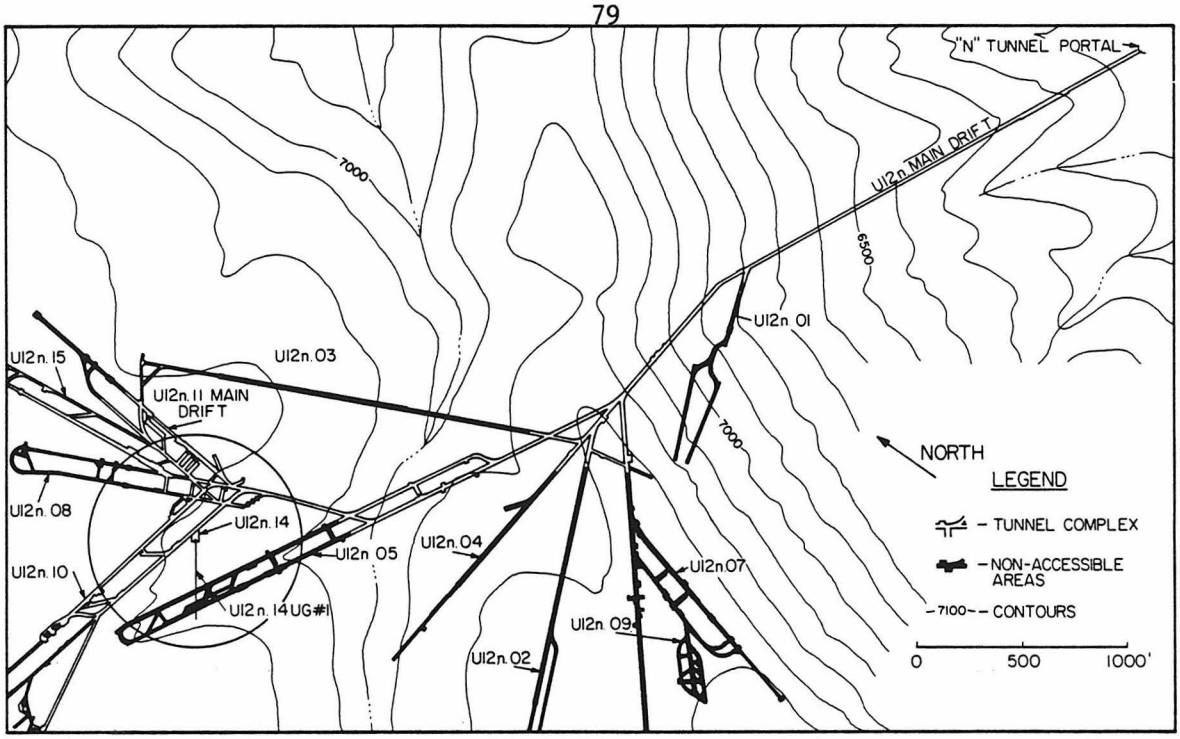

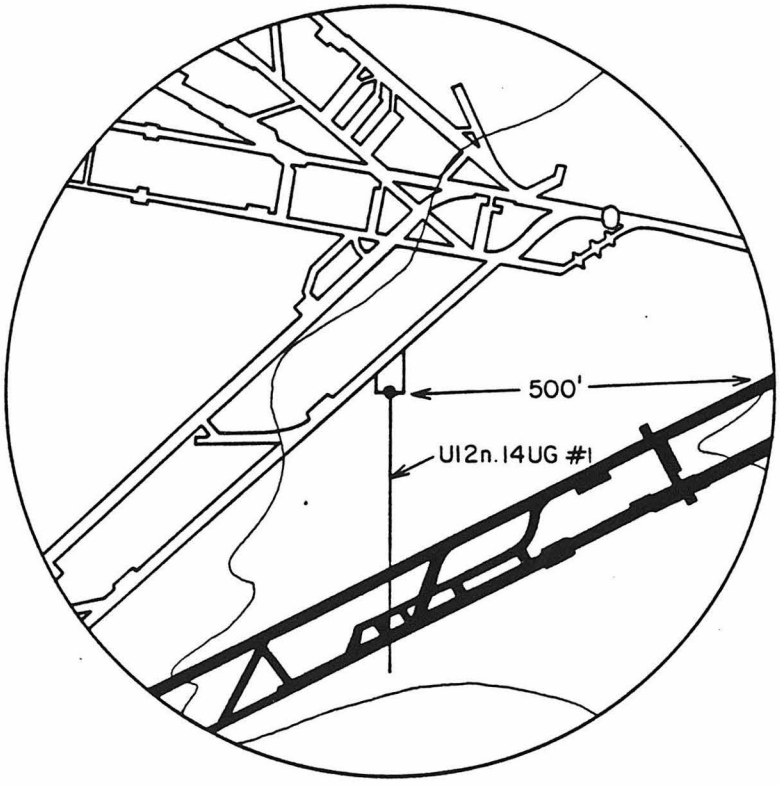

Figure 4-3 Plan view of n-tunnel excavations and the experiment site in U12n.14UG-1.

conducted our trials is identified as Tunnel bed, unit 4H, characterized by Dean Townsend (written communication, 1982) as follows:

> Tuff, calc-alkaline ash fall and thin beds of peralkaline ash fall. Calc-alkaline ash fall, light brown, medium-grained, zeolitized; 40-60% pale-yellow pumice, 4-15 mm, rarely up to 50 mm, and rare orange pumice, 5-10 mm; 5% fragments of welded tuff, 4-8 mm. Peralkaline ash fall, pale-green, coarse-grained, zeolitized; 80-85% pale-yellow-green pumice, 5-25 mm; 10-15% fragments of welded tuff, 5-15 mm.

The accuracy of in-situ stress measurements by the holographic stressmeter depends critically upon the elastic properties of the rock at the surface of the borehole wall. This results from the sensitivity of the strain-relief displacements to the elastic moduli, not from the stress concentration at the borehole wall which is independent of Young's modulus, and, except for one component, independent

TABLE 4-1
Elastic Moduli of U12n Tunnel Bed 4

	Uniaxial Secant Young's Modulus [kbar]	Dynamic Young's Modulus [kbar]	Unconfined Poisson's Ratio	Dynamic Poisson's Ratio
Number of samples	4	142	4	142
Minimum value	29.00	12.79	0.16	0.06
Mean value	43.98	98.63	0.23	0.33
Maximum value	66.90	264.87	0.26	0.46
Standard deviation	17.50	48.81	0.04	0.08

(From Brethauer et al., 1980)

of Poisson's ratio as well. Ultimately the stressmeter should itself measure the elastic moduli of the exposed rock in situ, but for the present we must rely on other measurements of the elastic properties. Many determinations of the physical properties of the tunnel beds have been made in the course of excavation and nuclear testing. We reproduce in table 4-1 a selection of values from a statistical survey of the physical properties of the rocks in the vicinity of our trial site by Brethauer et al. (1980). The actual bed in which we conducted our tests is Tunnel bed 4H. However, only a few measurements have been made of the properties of this unit, so we quote, instead, average values of each property for all of the reported measurements of that property in the units comprising Tunnel bed 4.

Stresses Predicted in Borehole U12n.14UG-1

The purpose behind conducting the experimental deployment of the stressmeter at NTS was to test the instrument's operation in a region where the stress field is relatively well known. Knowledge of the stress field comes from several sources. The vertical stress due to lithostatic loading at the borehole site is 68 bars. Ellis and Magner (1980) and Ellis (1979), report results of measuring in-situ stress with the U.S.B.M. deformation gauge at the tunnel level. Haimson et al. (1974), made numerous in-situ stress determinations employing hydrofracture in several orthogonal boreholes and determined values for the in-situ stress which are close, but not in perfect agreement with those based on the U.S.B.M. deformation gauge. We have adopted

Haimson's values to represent the stress state at our experiment site. This is somewhat arbitrary, perhaps, but hydrofracture is its most reliable when applied in several orthogonal holes, and as it is a direct measurement of stress it presents advantages over strain-relief measurements which rely on determinations of the elastic moduli of the surrounding rock.

Haimson (1974), reports the following values to represent the average principal stresses and their directions for n-tunnel: the intermediate stress is oriented vertically with the value 70 bars; the maximum compressive stress is 88 bars, oriented N 35° E; and the minimum principal compressive stress is 35 bars oriented N 55° W. It was assumed in analyzing the data, as it usually is in interpreting hydrofracture data, that one of the principal directions coincides with the borehole, thus the results were constrained to have one of the principal directions oriented vertically. Nevertheless, Haimson makes a favorable comparison of his results to those by Hooker et al. (1971), based on measurement with the U.S.B.M. deformation gauge. His determinations compare less well to those compiled by Ellis and Magner (1980), but even these indicate the intermediate stress is more nearly vertical than the maximum and minimum principal stresses and the maximum horizontal stress is oriented between N 37° E and N 53° E for three of four measurements in n-tunnel. These stresses are in agreement with the least principal stress oriented WNW-ESE through most of the Basin and Range province (Zoback and Zoback, 1980), and as the least principal stress is substantially less than the other two principal

stresses, which are quite similar and may switch with increasing depth, they are consistent and presumably related to the strike-slip, oblique-slip and normal faulting characteristic of the Basin and Range (Zoback and Zoback, 1980).

We have assumed Haimson's reported values are appropriate for comparing to the data obtained using the holographic stressmeter. As we have not made the measurements necessary for a complete determination of the in-situ stress state it is impossible for us to comment on the accuracy of these values or directions. Furthermore, since interpretation of data recorded by the holographic stressmeter requires confident knowledge of the elastic properties of the rock sampled, and these are not known precisely and vary widely among the tuff units and also within units, as discussed above, it would be inappropriate to conclude more than consistency apparent between the stressmeter data and other in-situ stress determinations. Our intent is simply to show that the stressmeter is measuring stress, in situ, in rock. We also adopt these values as representative values of in-situ stress for various calculations of simulated fringe patterns, to be presented below. We discuss in Chapter 5 a solution to the problem of determining the elastic properties by modifying the stressmeter to measure the elastic moduli, in situ, using the same holographic techniques employed to record strain-relief displacements.

Figure 4-4 sketches the relationship between the borehole U12n.14UG-1 and the stress field adopted from Haimson. Since the borehole is oriented S 55^{o} W, it is only 20^{o} off the bearing of the

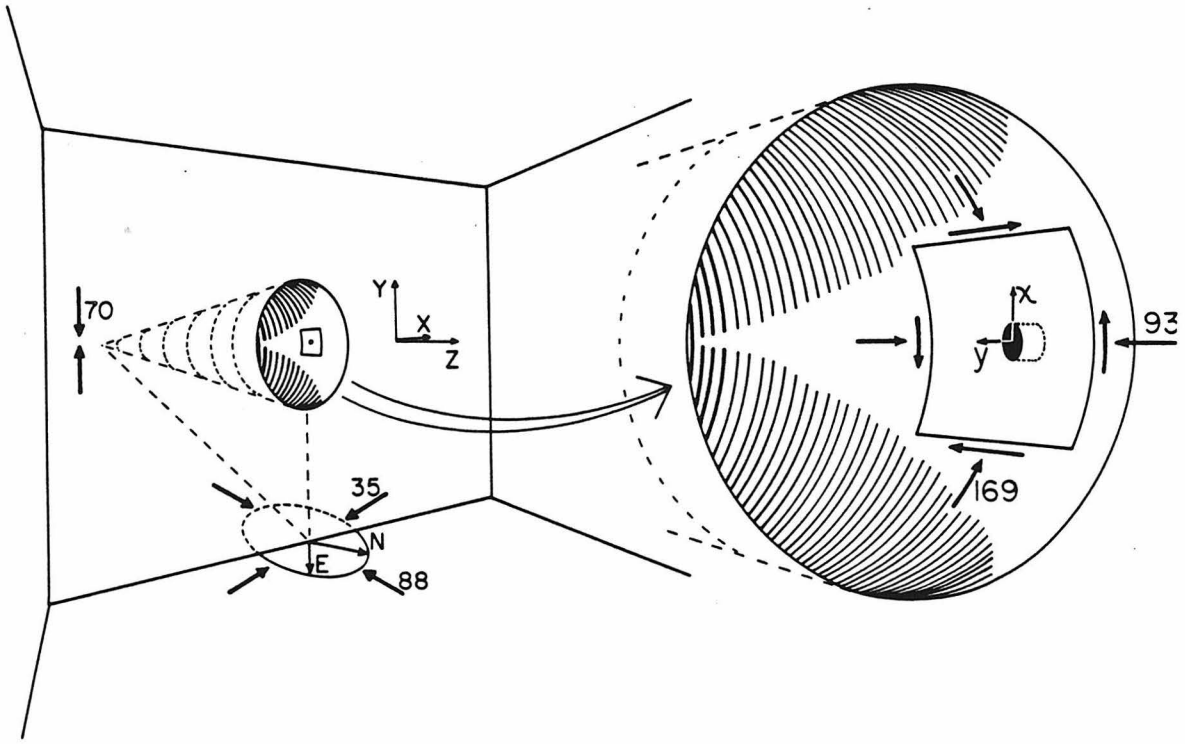

Figure 4-4 Diagrammatic sketch of U12n.14UG-1 borehole collar. The stress configuration drawn beneath the collar represents the far-field stress field reported by Haimson et al. (1974). The two-dimensional stress configuration, shown in the enlargement of the borehole, corresponds to the stresses calculated assuming Haimson's far-field stresses act on an infinite borehole. The side-core hole shown indicates correctly the orientation of our deployments in the borehole.

maximum principal stress axis. At the site of our tests it is also inclined 2^{o} to the horizontal, rising away from the collar. The horizontal principal stresses and axes are indicated in the circle drawn beneath the borehole collar. The consequence of this close alignment is vanishing shear stresses on the borehole wall, as explained in Chapter 2. Using the usual tensor transformation laws, the stresses of Haimson et al. (1974), take the following form in the borehole cartesian coordinate system: σ_x=41.2, σ_y=70.0, σ_z=81.8, τ_{xy}=0.6, τ_{xz}=-17.0, τ_{yz}=-0.4 . The enlarged sketch of the open end of the borehole shows the side-core hole cartesian coordinate system defined in Chapter 2. The two non-vanishing normal stresses, calculated from the assumed stresses transformed to the borehole coordinate system and equations 2-3, act at the point on the borehole wall indicated by the side-core hole, assuming the point is away from the ends of an effectively-infinite borehole. Thus the stresses at the borehole wall are S_{zz}=93 bars acting along the axis of the borehole and $S_{\theta\theta}$=169 bars, acting circumferentially. The shear stress effectively vanishes due to the close alignment of Haimson's principal stress axes with the borehole cartesian coordinate axes. Notice that in the core-hole cartesian coordinate system, y is oriented in the -Z direction, that is down the borehole. All photographs of strain-relief holograms recorded in the borehole and all computer-simulated fringe patterns are presented with y up and x directed to the right. Keep in mind that x, to the right in the fringe patterns, is up in the earth, for the horizontal borehole.

Our ultimate goal is to determine the far-field stresses, which can

be found, via equations 2-6, from the stresses acting at three azimuths on the borehole wall. The stresses $S_{\theta\theta}$, S_{zz}, and $S_{\theta z}$ desired at each azimuth correspond to 169 bars, 93 bars, and 0 in figure 4-4, for the particular side-core hole positioned at the right horizon. Figure 4-5 shows the relationship between the various stresses and coordinate systems when placed in the framework of a stressed thin plate with a hole, representing the segment of the borehole wall adjacent to the side-core hole. The figure is properly oriented for a vertical borehole.

The holographic stressmeter records the displacements resulting from drilling the strain-relieving side-core hole. We seek the stresses $S_{\theta\theta}$, S_{zz}, and $S_{\theta z}$ acting at the point of each of the three required side-core holes. Hence we must examine the relationship between the strain-relief displacements, the elastic properties of the rock, and the stresses acting at a point on the borehole wall.

Displacements Due to Strain-Relief Hole

We model the deformation due to drilling a strain-relief hole by employing the analytic solution for the motions resulting from introducing a through-going hole into a stressed thin plate under the assumption of plane stress. This is an approximation to the physical situation, and as we will show, it is not a particularly good one, but it offers the advantage that its analytic solution permits inexpensive calculations.

The actual geometry of the strain-relief configuration is a shallow

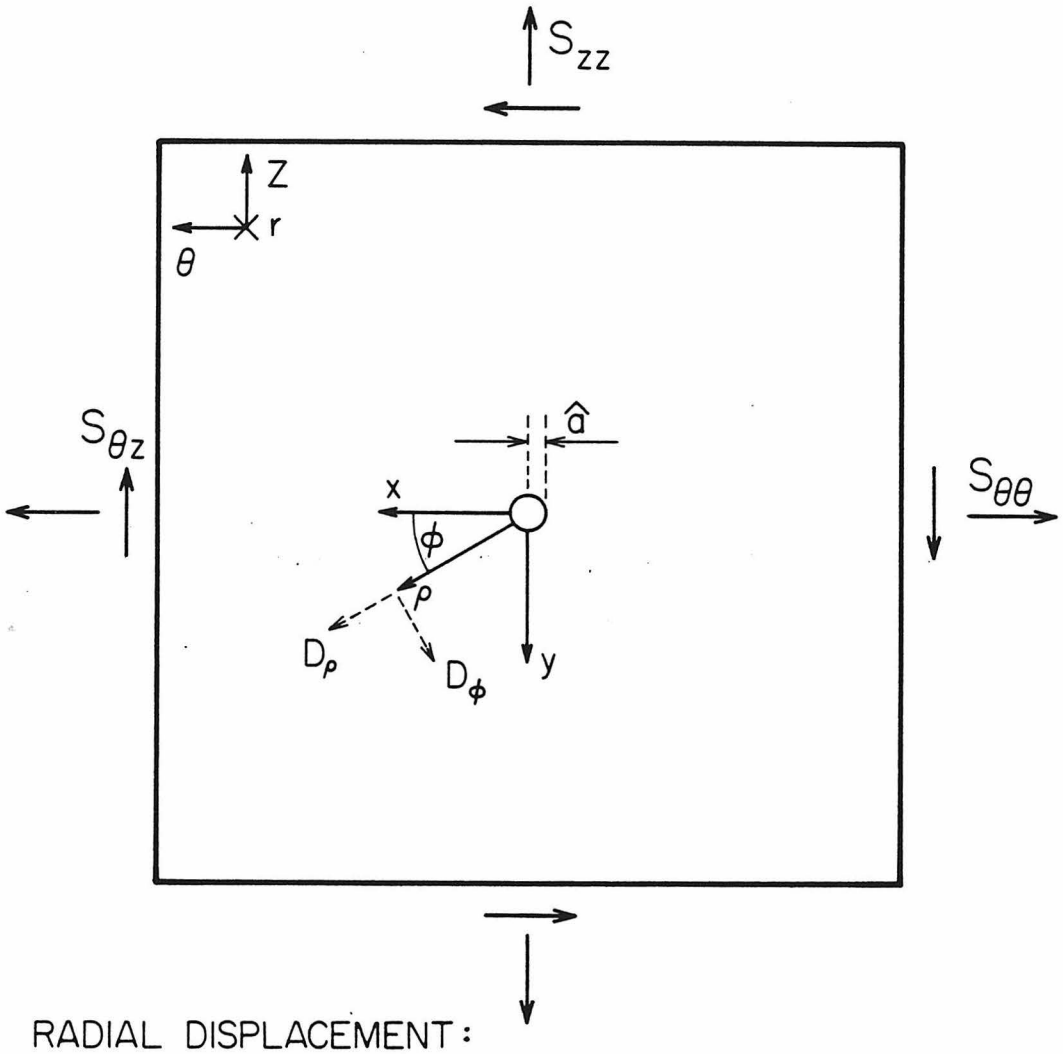

RADIAL DISPLACEMENT:

$$D_\rho = \frac{1}{2E}\left[(S_{\theta\theta}+S_{zz})\alpha+(S_{\theta\theta}-S_{zz})\beta\cos 2\phi - S_{\theta z}\beta\sin 2\phi\right]$$

TANGENTIAL DISPLACEMENT:

$$D_\phi = \frac{-\gamma}{2E}\left[(S_{\theta\theta}-S_{zz})\sin 2\phi + S_{\theta z}\cos 2\phi\right]$$

WHERE:

$$\alpha = (1+\nu)\frac{\hat{a}^2}{\rho},\quad \beta = 4\frac{\hat{a}^2}{\rho} - (1+\nu)\frac{\hat{a}^4}{\rho^3}$$

$$\gamma = (1+\nu)\frac{\hat{a}^4}{\rho^3} + (1-\nu)\frac{2\hat{a}^2}{\rho}$$

Figure 4-5 Diagram of an elastic plate with a through-going hole. This analog is employed to model the displacements resulting from drilling strain-relief holes. (See text.)

hole (the side-core hole) drilled into the wall of a cylindrical borehole. Furthermore, the stresses are varying both as a function of azimuth and radius. Hence the actual geometry is complex and difficult to model exactly. Some simplifying approximations must be incorporated to reduce this complexity and make modelling practical. To model the geometry as a homogeneously stressed semi-infinite space into which a shallow hole is drilled we introduce three principal approximations: 1) the cylindrical section of the borehole wall surrounding the side-core hole can be approximated as planar, 2) the stress is adequately represented as independent of depth, 3) the stress is sufficiently homogeneous in the region surrounding the side-core hole to be considered invariant.

The first approximation constrains the angle subtended by the field of view used for interpretation to be small compared to the borehole circumference. The field of view in the prototype stressmeter is less than 10 cm in a 30 cm diameter borehole. The maximum deviation of the cylindrical surface from the tangent plane occurs at the periphery, amounting to less than 1 cm, justifying the application of a half-space model.

The second approximation requires the stress to vary minimally over the depth of the side-core hole. Figure 2-4 shows that in the worst case possible for the stress state at the NTS trial site, one stress component varies by 25% over the depth of the side-core hole (indicated by the vertical dashed line.)

The third approximation originates in our desire to determine the

stress state at individual points on the borehole wall. Consequently, our measurements are meaningful only if the stress state at the borehole wall is effectively constant on the scale of the diameter of the side-core hole. If we neglect shear stresses (i.e. assume alignment of the borehole with a principal axis), then the component of stress varying most rapidly with azimuth at the borehole wall is $S_{\theta\theta}$, defined in equation 2-2a. We define $\hat{a}$ to be the radius of the side-core hole, shown in figure 4-5, and $\Delta\theta=\hat{a}/a$, half the angle subtended by the side-core hole. The fractional variation in stress $S_{\theta\theta}$ is given by expression 4-1, which is derived from equation 2-2a.

$$\frac{\Delta S_{\theta\theta}}{S_{\theta\theta}} = - \frac{4\ (\sigma_x - \sigma_y)\ \sin(2\Delta\theta)\sin(2\theta)}{\sigma_x + \sigma_y - 2(\sigma_x - \sigma_y)\cos(2\theta)} \qquad (4\text{-}1)$$

Thus to neglect the variation of $S_{\theta\theta}$ on the scale of the diameter of the side-core hole, we require $8\Delta\theta<<1$. Notice that for most reasonable states of in-situ stress the denominator of expression 4-1 will always be greater than 1. With the prototype instrument configuration in our trials with the holographic stressmeter $\Delta\theta=.042$. Consequently, at certain locations, indicated by equation 4-1, the variation may be larger than desirable.

Thus under the constraint that the ratios of the side-core hole depth and diameter to the borehole diameter are small, a shallow hole in a stressed half-space is suitable for modelling the strain-relief displacements.

We have gone further, approximating a shallow hole in a stressed

half-space as a through-going hole in thin plate under plane stress. To justify this model we compare the solution for a thin plate with a hole to a finite-element calculation of a shallow hole in a thick plate to determine how the finiteness of the side-core hole influences the strain-relief displacements.

As we will show, the analogy to a flat plate with a through-going hole breaks down at a radius of several diameters from the center of the side-core hole, but it has a well-known analytic solution and is thus well adapted for a first effort at modelling the strain-relief displacements. The elastostatic problem is discussed by Timoshenko and Goodier (1934) (who credit Kirsh with the original solution in 1898), and also Jaeger and Cook (1979), among others. The problem separates into solving for the displacements in a thin plate with a through-going hole, uniaxially stressed at infinity. Then by superposition the displacements due to any plane stress state may be determined. In our case we are interested only in the displacements resulting from drilling the side-core hole. Thus we consider only the difference between the displacements in a plate containing a hole and the displacements in a continuous plate, both subject to the same state of far-field stress. The solution to this problem in the side-core hole cylindrical coordinates, for a general plane stress field, is given in eqations 4-2 and shown in figure 4-5.

$$D_\rho = \frac{1}{2E}\left[(S_{\theta\theta} + S_{zz})\,\alpha + (S_{\theta\theta} - S_{zz})\,\beta\cos 2\phi - S_{\theta z}\,\beta\sin 2\phi\right] \qquad (4\text{-}2a)$$

$$D_\phi = \frac{-\gamma}{2E}\left[(S_{\theta\theta} - S_{zz})\ \sin 2\phi + S_{\theta z}\ \cos 2\phi\right] \qquad (4\text{-}2b)$$

where:

$$\alpha = (1 + \nu)\ \frac{\hat{a}^2}{\rho},\ \beta = 4\ \frac{\hat{a}^2}{\rho} - (1 + \nu)\ \frac{\hat{a}^4}{\rho^3} \qquad (4\text{-}2c)$$

$$\gamma = (1 + \nu)\ \frac{\hat{a}^4}{\rho^3} + (1 - \nu)\ \frac{2\hat{a}^2}{\rho}$$

D_ρ and D_ϕ are the radial and tangential components of displacement, respectively, due to creating a through-going hole of radius $\hat{a}$ in a stressed plate. Notice that positive $S_{\theta z}$, indicated in the figure, corresponds to negative shear in the x-y reference frame (side-core cartesian coordinate system). Hence the sign reversal for the shear components in equations 4-2a,b, when compared to the usual solution.

An important property of equations 4-2 is that the displacements die off as $1/\rho$, the radius from the center of the side-core hole. This suggests one of the inherent advantages of the measurement approach of the holographic stressmeter. It measures displacements which decay as $1/\rho$ rather than strains which decay as $1/\rho^2$. Therefore it can sample the strain-relief further from the edge of the strain-relief hole than it could if it measured strain directly. This reduces the complications associated with anelastic deformation and the effects of residual strains on individual grains, near the side-core hole. Furthermore, sampling the whole displacement field provides more information about

the strain relief than point measurements such as metal-foil strain gauges. Another desirable property of the displacements is that they scale as the square of the hole radius $\hat{a}$. This allows you to adjust the sensitivity of the stressmeter over a substantial range simply by changing the diameter of the side-core drill bit.

To test the validity of the plate-with-a-hole model we compared the calculated displacements due to the strain-relief hole, using the solutions for the plate model, with the calculated displacements for a finite-depth hole in a thick plate determined by the finite-element method. (Brad Hager performed the finite-element calculations.) All of the finite-element results apply only to axisymmetric stress in a thick plate with a finite hole. The ratio of plate thickness to hole radius is 16 to closely approximate a half-space.

The finite-element displacements, in the plane of the surface, calculated for a through-going hole compare within 3% to the results of the analytic solutions for the plane-stress plate-with-a-hole model.

However, for the case of a shallow hole, the depth of the hole influences the displacements and the comparison indicates the magnitude of the error involved in using the plate-with-a-hole model to calculate the displacements for a shallow hole. The case we tested is a hole 1 diameter deep, subjected to axisymmetric compression at infinity. The divergence between the displacements calculated for the shallow hole using finite elements and those for the analogous thin-plate-with-a-hole model defines the region where the plate model yields acceptable results. We will consider both the in-plane and normal motions as a

function of radius from the axis of the hole, measured in radii of the hole. Figure 4-6 compares the displacements calculated using the thin-plate-with-a-hole model to the results of finite element calculations for a shallow hole in a half-space, both subject to axisymmetric compression.

The thin-plate solution does not yield motions normal to the surface. Since the holographic stressmeter is approximately 2-3 times more sensitive to normal motions, depending on position, it is important to identify normal motions which might influence the fringe patterns even though they are but a small component of the displacement. The magnitude of the normal motions depends on Poisson's ratio. ν=0.2 was used for these calculations. The finite-element calculations show that the normal motions range from 20-30% of the in-plane motions at distances between 1 and 3 radii. Beyond 3 radii the ratio of normal to in-plane displacements decays from 20% to 0. Hence we conclude that the fringes within a 1 diameter anulus around the side-core hole are heavily influenced by normal displacements not modelled by the plate calculations.

In contrast, the plate model correctly predicts the magnitude of in-plane displacements at the edge of the side-core hole, but does progressively worse at greater distances. Between 1 and 3 radii it agrees with the finite-element results within 25%, but by 5 radii they differ by a factor of two, as shown in figure 4-6 As expected, the plate model overestimates the displacements since it is essentially correct for an infinitely deep hole, not a finite hole. This comparison implies

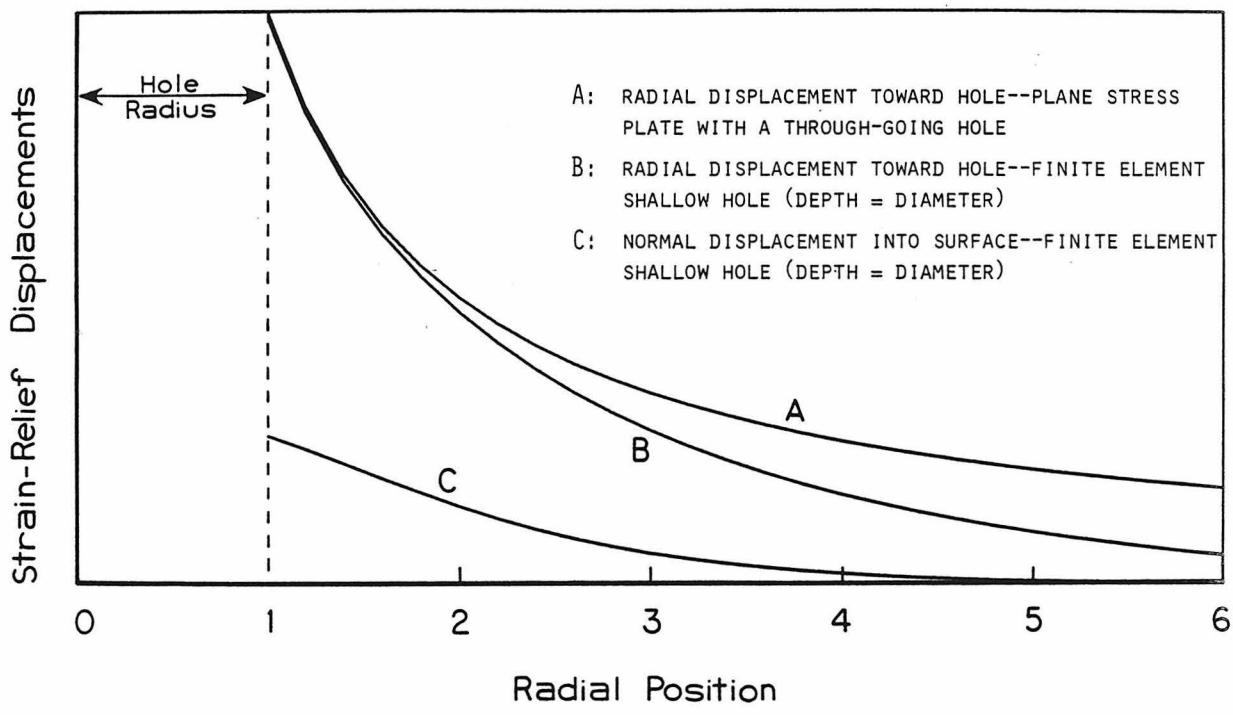

Figure 4-6 Comparison of calculated displacements of the surface surrounding a cylindrical hole introduced into a stressed elastic medium, for two models. Both models assume axisymmetric compression of a material with Poisson's ratio, 0.2. Curve A is determined from the plane-stress plate-with-a-hole model, equations 4-2. (The thin-plate assumption precludes motions normal to the surface.) Curves B and C were calculated using finite elements for a stressed half-space with a hole the same diameter as adopted to calculate A, but only one diameter deep.

that the side-core hole should be substantially deeper than its diameter if the plate-with-a-hole model is to be used to calculate fringe patterns as the finite-element results show that increasing the depth of the side-core hole both decreases the normal displacements and improves the fit between the the displacements and the thin-plate model.

Clearly a detailed examination of the failings of the plate-with-a-hole model must be rigorously explored before quantitative analysis of in-situ stress data can be attempted. However, at this stage, our progress is limited by the quality of the holographic images recorded. We consider this analysis adequate for the data we have obtained.

Simulated Fringe Patterns

All of the computer simulated fringe patterns presented below represent calculation of displacements on a point-by-point basis using the plane-stress plate-with-a-hole model. The displacements are then applied to equation 3-1 yielding the synthetic fringe patterns. The pattern generated is what an observer or camera lens, at a particular observation point, would see superimposed on the reconstructed virtual image of the strain-relieved borehole wall. Although the approximation improves with increasing hole depth, the approximations inherent in the plate model result in a 60% overestimation of the magnitude of displacement at the radius of 2 side-core hole diameters, when the hole is 1 diameter deep, well inside the boundaries of the synthetic fringe patterns displayed in the next few figures.

The variety of fringe patterns is substantial. While the geometry of the holographic recording system imposes constraints on the patterns which can form, the constraints are small compared to the wide range of patterns resulting from conceivable surface displacement fields. Figure 4-7 depicts the range of possible simulated interference fringe patterns for nine different specified displacement fields. The first four correspond to uniform .0025 mm motions of the surface with respect to the holographic recording system. In the top row where, respectively from left to right, the four-wavelength motions are to the right, inclined 45^{o}, and towards the top, the resulting pattern is a series of almost linear parallel fringes perpendicular to the direction of motion. Four wavelengths of motion normal to the surface produces the fourth fringe pattern. The roughly circular fringes are centered upon the projection from the surface to the source of diffused illumination. The fringe order is much higher than in the previous examples, indicating greater sensitivity to vertical motions than the horizontal motions of the first three cases.

Relative rotations between the instrument and target are also possible. The fifth fringe pattern corresponds to a relative rotation of 100 microradians about the axis of the side-core hole. None of these simple motions can produce a circular pattern centered on the side-core hole. The significance of this observation will become apparent in arguments presented below.

The remaining four fringe patterns in figure 4-7 are the result of strain-relief displacement fields for simple stress configurations,

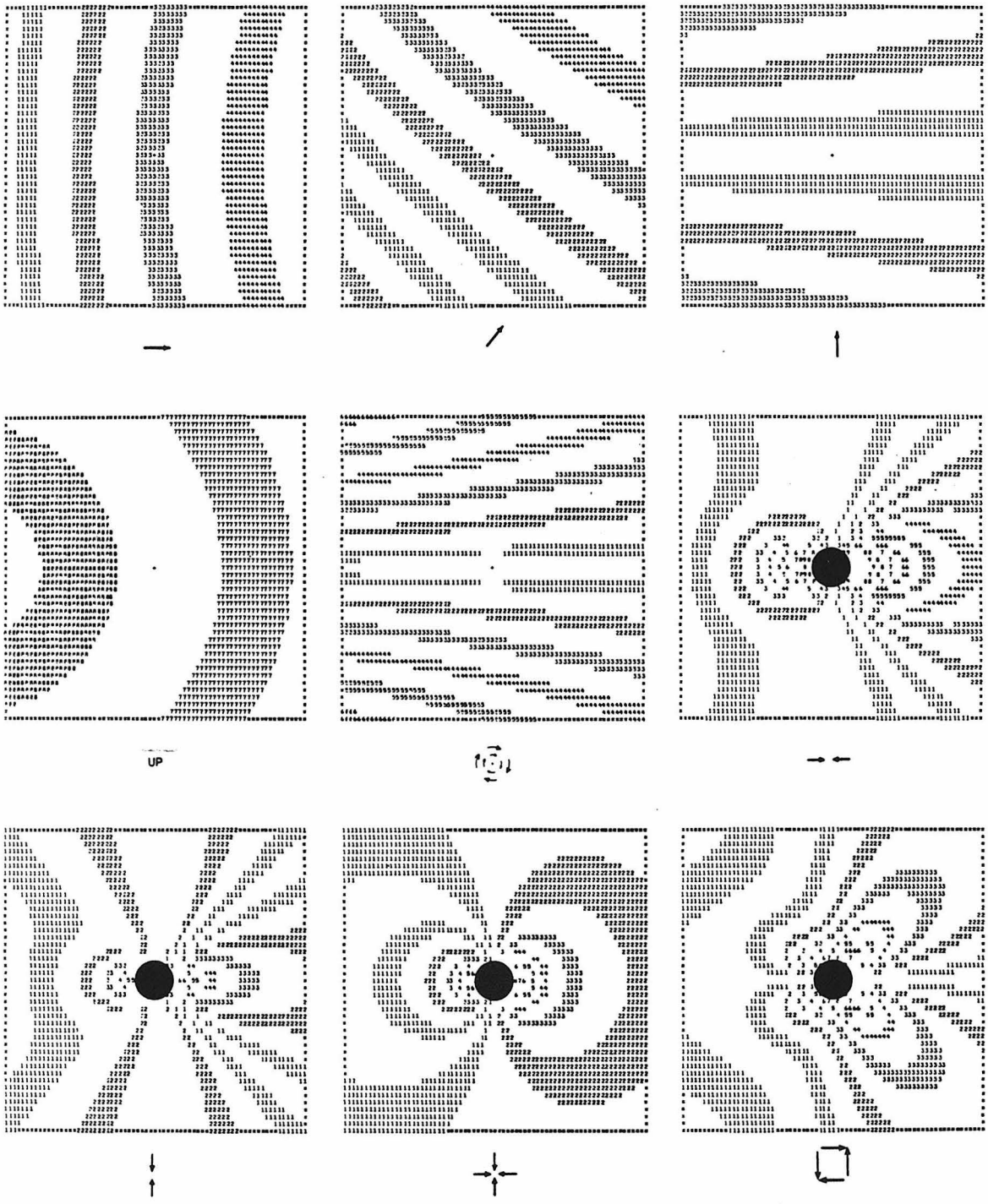

Figure 4-7 Examples of the range of interference fringe patterns produced by simple motions. The first five are displacements or rotations as indicated. The last four result from strain-relief displacements calculated with the plate-with-a-hole model, for the plane stress states shown.

calculated using the plane-stress, plate-with-a-hole model. They represent, in order, horizontal uniaxial compression, vertical uniaxial compression, isotropic compression, and pure shear.

Each of the nine fringe patterns is reproduced as an observer would see it from along the axis of the side-core hole, 25 cm from the virtual image of the surface. The vertical symmetry results from observing along an axis which is contained in both the symmetry plane for the recording system and a symmetry plane in the displacement fields (except for the second pattern). (Note that since the interference holographic technique is insensitive to the sign of vector motion, pure-shear and rotation yield effectively symmetric displacements.) Substantially more information is stored in a holgraphically reconstructed virtual image and its superimposed interference fringe pattern than is represented by the fringe pattern as seen from a single observation point. We will address below a method of using this additional information to invert the interference fringe pattern and determine the actual displacements.

Analysis of Strain-Relief Fringes

The middle row in figure 4-8 displays a photograph of a reconstructed strain-relief hologram from an in-situ stress measurement attempt 193 cm from the collar in U12n.14UG-1. The 1.3-cm-diameter side-core hole, indicated by the dashed circle, was drilled horizontally, in the northwest direction (to the right when facing down the hole), to a depth of 0.9 cm between the two holographic exposures. This interference hologram is atypical of the six strain-relief

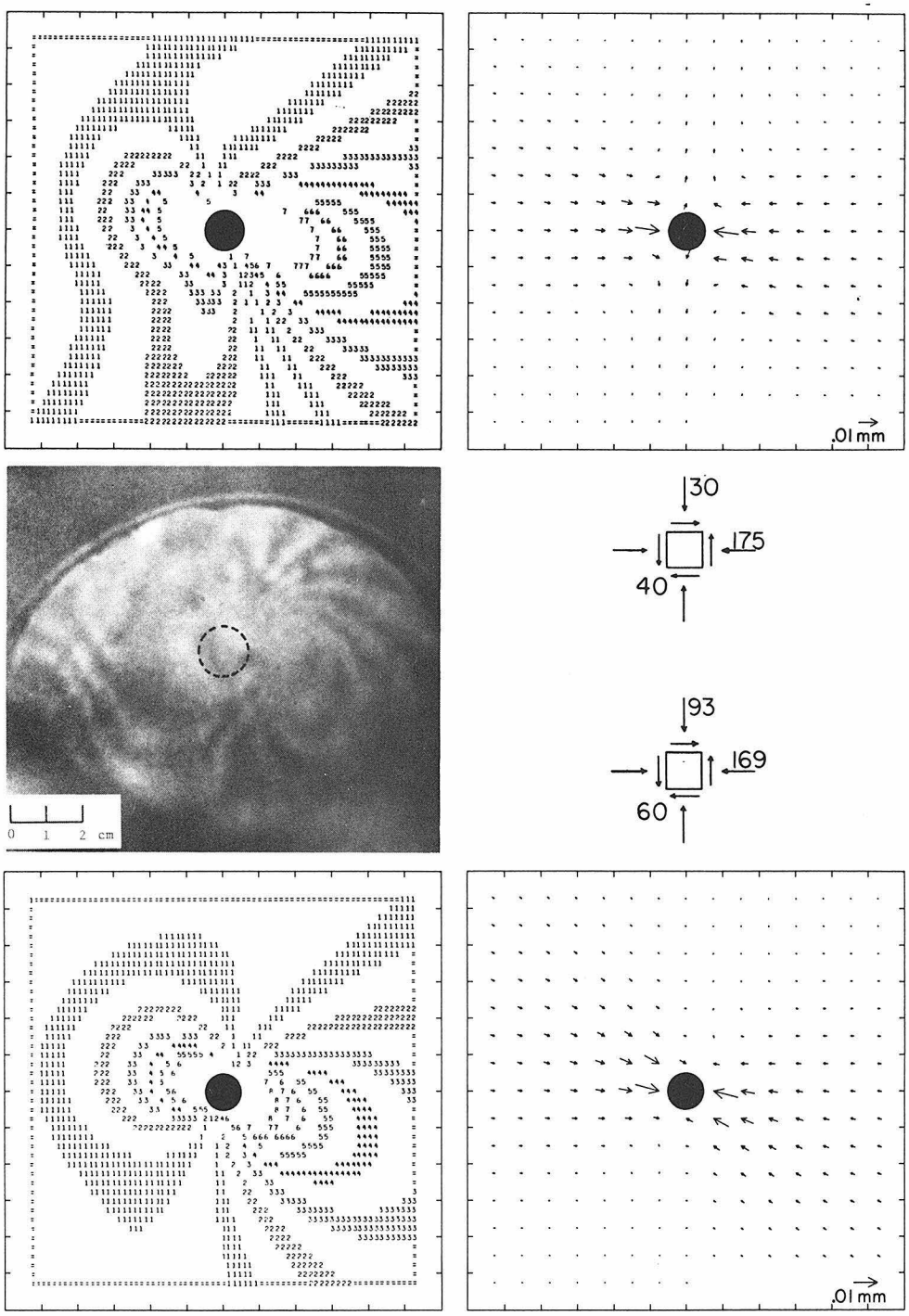

Figure 4-8 Photograph of interference fringes recorded in U12n.14UG-1 borehole, in the middle row, compared to calculated displacements and fringe patterns for the two stress states indicated.

holograms in which mechanical and optical stability was successfully maintained during drilling, permitting interference fringes to form in response to strain-relief displacements. It is the only one with sufficiently distinct fringes that we could photograph them adequately for printed reproduction. The fringes are more distinct in this example because the side-core hole was only drilled to 0.9 cm depth so that a second strain-relief measurement could capture the strain relief due to drilling from 0.9 cm to 2.3 cm depth. Both of the resulting interference holograms display remarkably similar fringe patterns implying that the second phase of drilling produced further strain-relief displacements in the same directions as the original phase. Hence in the first phase of this sequence, the displacements were smaller than in the other tests, where the side-core holes were drilled to the maximum possible depth. Consequently, it yielded a lower density of fringes and more distinct fringes which are easier to photograph. Clearly, at this combination of stress level and elastic modulus a smaller diameter side-core drill bit would be appropriate, as would any improvements to the recording system which yielded clearer fringe definition. However, failing that, the fringes are readily observed in the reconstructed holograms even if difficult to capture photographically.

A visual comparison of the holographic reconstructions of this example and a test conducted 222 cm from the collar in U12n.14UG-1, in which the 1.3-cm-diameter side-core hole was drilled 1.7 cm into the borehole wall, shows a very similar pattern of fringes to those in

figure 4-8. The primary difference is that in the latter case each fringe is finer and there are approximately twice as many of them, spaced closer together. The two sites, though near to the end of the borehole, are so close (29 cm apart), that they should be sampling identical states of stress. The similarity of the two fringe patterns and the increased fringe density in the test expected to produce greater strain relief implies that the stressmeter is making at least qualitatively consistent measurements.

In several of the figures to follow we will show simulated interference fringe patterns calculated for assumed states of stress and elastic properties. Ideally we would like to base our choice of values of elastic moduli on in-situ determinations appropriate for the rock lining the borehole wall. However, as we did not measure the elastic moduli in situ we are left with a choice between the averages of the scattered values for the particular geologic unit, tunnel bed 4H, or arbitrarily selected values. Opting for the latter, we have made all of our calculations assuming ν, Poisson's ratio, is 0.2. E, Young's modulus, is taken to be 150 kbar for figure 4-8 and 200 kbar for figures 4-11, 4-12, and 4-13. Brethauer et al. (1980) report 142 values of dynamic Young's modulus for Tunnel bed 4 ranging in value between 12.8 and 264.8, averaging 98.6, as shown in table 4-1. Until we develop the capacity to determine an appropriate value for the elastic moduli in situ our arbitrary selection is probably justified. However, simple examination of expressions 4-2 shows that while the displacements are only somewhat sensitive to the value of Poisson's ratio, they scale

inversely with the value of Young's modulus. Hence halving the value of Young's modulus doubles the calculated displacements which doubles the interference fringe density.

To the right of the photograph of the strain-relief fringes, in figure 4-8, are two two-dimensional stress configurations corresponding to the simulated displacements and fringes in the top and bottom rows of the figure. The origin of these values relates to the assumed stress field and the underlying geometry. The stresses corresponding to the upper row of the figure are based on assuming that the stress acting along the borehole axis is substantially released because the site is only 193 cm from the end of the alcove U12n.14 main (see figure 4-4). Consequently, the hoop stress $S_{\theta\theta}$, or σ_x in the side-core coordinate system, resulting from the lithostatic-loading stress concentrated by the borehole, is large, and S_{zz} (which is also σ_y), is fairly small. The value for τ_{xy}, the shear stress corresponding to $-S_{\theta z}$ was adjusted to reproduce as much as possible the features of the observed strain-relief fringe pattern. The plot on the right side of the top row in figure 4-8 depicts the displacements calculated with equations 4-2 for a 10 cm square grid of points on the surface of a plate with a through-going hole. Each arrow indicates the vector displacement of the point located at the head of the arrow, scaled to the .01 mm vector drawn in the lower right side of the figure. The filled circle marks the side-core hole. The figure in the upper-left-hand corner shows the interference fringe pattern resulting from applying equation 3-1 to the displacement field shown. The printed symbols in the simulated fringe

pattern correspond to the order of the fringe, or the absolute value of n in equation 3-1. Notice that the outer-most fringe is first order and the order increases toward the side-core hole. This is true in general for the strain-relief fringes as the displacements tend toward zero with increasing radius from the axis of the hole. Comparison of the calculated fringe pattern to the observed fringe pattern shows some similarity, but also some significant differences, suggesting that the selected stress state is not very close to the actual stresses affecting the borehole wall at this site. The bottom row shows two similar plots for another possible stress state.

The stress state corresponding to the plots in the bottom row of figure 4-8, depicted in the lower of the two stress configurations, is closer to the predictions of equations 2-3 for our assumed far-field stress state. The values for the normal stress, $S_{\theta\theta}$=169 bars and S_{zz}=93 bars are calculated directly from equations 2-3. This represents a much larger value for S_{zz}, the stress acting along the borehole axis, than in the example in the top row. However, although the stress-measurement site was only 193 cm from the face of the end of the alcove, suggesting reduction of the axial stress, the distance is approximately the half-width of the alcove. Considering the stress concentration equations 2-1b and 2-1c, plotted in figure 2-4, as a crude approximation to the stress perturbation due to the alcove, we infer that at a distance of one radius (or half-width) from the alcove end wall (as is the measurement site), the stresses are not badly misrepresented by equations 2-3. Hence the two normal stresses are

justified.

The value for the shear stress in the lower stress state in diagram 4-8 was selected to produce the best likeness to the observed interference fringe pattern. Clearly this simulated fringe pattern is a better approximation to the observed pattern than the one above. The origin of the shear stress is hard to explain. The high value of shear stress is required to reproduce the fringe lobes to the right of the side-core hole so that they droop to the right, one of the principal features in the fringe pattern reproduced in figure 4-8. This characteristic pattern also occurs in other strain-relief holograms from adjacent trials. Two explanations are possible, assuming that the high value of shear stress is real. First, that the proximity of the free surface at the end of the borehole to the measurement site so perturbs the stress field that high shear stresses appear. Second, the assumed far-field state of stress is incorrect. Equation 2-2c shows that shear stresses can appear only if there are far-field shear stresses τ_{xz} or τ_{yz} (as represented in the borehole cartesian coordinate system). τ_{xz} vanishes if either the X or Z axis is a principal axis and τ_{yz} vanishes if either the Y or Z axis is a principal axis. Hence we can conclude immediately that the Z axis of the borehole must not be a principal axis of the far-field stress, nor as close to a principal axis as it is to the axes of the assumed stress state. Furthermore, since the side-core hole was drilled horizontally, $\theta=0$, so for $S_{\theta z}$ not to vanish, τ_{yz} must be non-zero. Thus the borehole Y axis, oriented almost directly up, must also not be a principal axis. Both of these

constraints are acceptable, although both are incompatible with the assumed stress field, but without further information such as the strain-relief fringe patterns for the two other azimuths required for a complete stress determination, it is not possible to draw further conclusions. Ellis and Magner (1980) report that two of the three stress measurements made in the U12n.10 tunnels using the U.S.B.M. overcore method had all of their principal axes oriented at least 40^{o} from the vertical, but not in a consistent fashion. Thus there is reasonable evidence that the stress field measured by Haimson et al. (1974) may not adequately represent the stress state at our trial site. This may be due to spatial variations in the stress field, or perhaps temporal changes possibly due to the nuclear testing itself.

The photograph of the recorded fringe pattern shows a greater number of fringes than the lower simulated fringe pattern. The fringe density in the calculated patterns depends strongly on the chosen value of Young's modulus. In this case we used 150 kbars. If this were reduced to 100 kbars, approximately the average value for the rocks in the particular geologic unit, it would increase the fringe density in the calculated pattern to a level greater than the level observed in the reconstructed hologram. However, as described above, it is also clear that the 0.9-cm-deep side-core hole did not completely relieve the stored strain in the wall rock surrounding the hole. Thus the calculated displacements overestimate the actual displacements by some unknown factor, reflecting the limitations of the plate-with-a-hole model. Both of these unknown factors must be quantified before

confident interpretation of the strain-relief fringe patterns is possible. Nevertheless, it appears that the strain-relief patterns recorded by the stressmeter imply stresses of at least the correct order of magnitude for the particular test site.

Potential Non-Strain-Relief Displacements

We have presented above the argument proposing that the measurements recorded by the holographic stressmeter reflect the stresses acting upon the rocks comprising the borehole wall. An alternate approach is to show that the deformations recorded cannot be due to any other effects. One way to make this case is to conduct control experiments. In this case a control experiment amounts to conducting a stress measurement under conditions where stresses, if they exist, will not contribute to the displacement field, but where extraneous effects might. It must be demonstrated that no other effects are dominating the motions which we have attributed to strain relaxation in the preceding discussions.

Several mechanisms pose an obvious potential for producing motions on the surface of the borehole wall during the interval between the two exposures of the interference hologram. One of these is heat. Thermal expansion of the rock, or possibly thermally driven desiccation could lead to deformations of the surface. The principal heat source is likely the frictional heating generated by the drilling process itself, particularly with our deployment at NTS where the drill bit cuts without coolant. Another possibility is that the vibration and stresses

produced by the drilling procedure propagates microcracks in the region surrounding the side-core hole. These growing cracks would have associated strains which could contribute to the total deformation observed on the surface. If the rock behaves anelastically, perhaps relaxing by some visco-elastic mechanism or time-dependent crack propagation, it might be important to the determination of stress exactly when the second exposure of the double-exposure hologram is recorded as the deformation might continue for a substantial period of time. Still another possibility is that the rock stores residual elastic stress which relaxes due to the drilling of the strain-relief hole, either as an equilibrium adjustment to the freshly-created free surface, or due to alteration of the mechanical properties of the elements storing the residual stress, by propagation of cracks, for example. In this case, we will consider as residual stress any non-zero stress which is mechanically self-equilibrated on some local scale.

The deformations associated with each of these mechanisms, and possibly others not considered, could conceivably be misinterpreted as strain relief reflecting the far-field state of stress. Therefore, it is critical to evaluate how, if at all, these non-strain-relief mechanisms influence the measurements made by the holographic stressmeter. Two approaches are possible here, one based on theoretical analyses, which depends on guessing on the important processes to study, the other on empirical tests. We have opted, for the present, to make empirical tests, effectively control experiments, under the appropriate conditions to test the significance of extraneous effects contaminating

the stressmeter measurements.

Figure 4-9 displays the reconstructed interference fringes for one such experiment conducted in U12n.14UG-1 at NTS. The two exposures of this interference hologram encompassed a five-minute interval beginning three minutes after the completion of drilling a 2-cm-deep strain-relieving side-core hole, indicated by the dashed circle. The record of fringes assures that adequate stability of the recording system was maintained. The second 70 mm film from this exposure shows fringes parallel to those shown in figure 4-9, but two to three times more densely spaced. Thus we infer that the parallel fringes originate by creeping of the film, which is held under tension in the film cassette. The important observation to note here is that the fringes approach and pass by the strain-relief hole without distortion. This implies that there are no time-dependent deformations active during this time window. It also suggests that any drill induced heating, if it occurred, had either diffused prior to the onset of the first exposure, or produces such slow motions that they aren't detectable over this five-minute interval.

A more conclusive test, conducted in the laboratory, is represented in figure 4-10. The photograph in the upper half of the figure shows the reconstructed double-exposure hologram of the cut face of a 7.5 by 7.5 by 2.5 cm block of tuff from the tunnel U12n.10 bypass near the junction of U12n.14 main. By visual examination the sample is indistinguishable from the tuff exposed in U12n.14UG-1. It was cemented with epoxy to a steel block in the appropriate position so that the

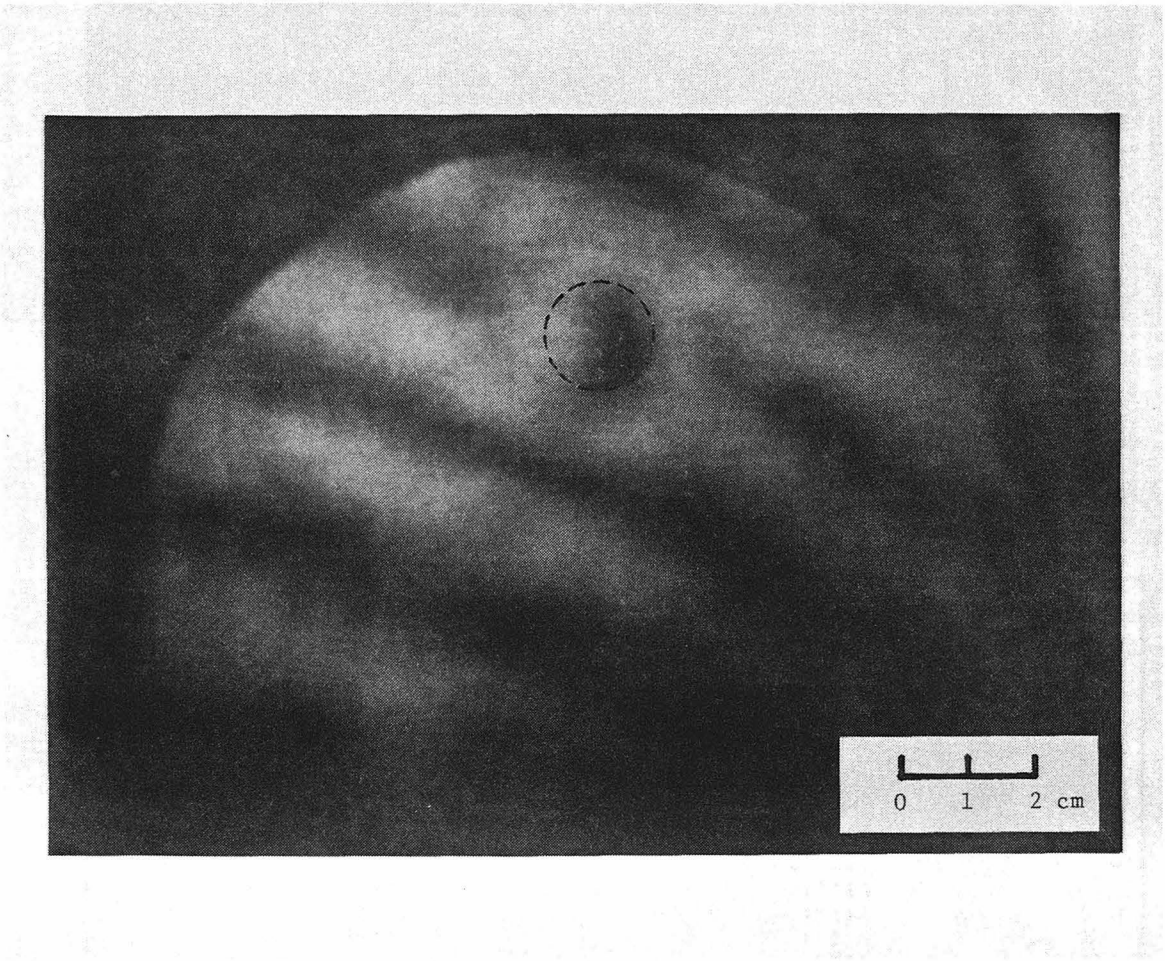

Figure 4-9 Interference hologram showing linear displacement fringes resulting from motion during the 5-minute interval between the two 7-second exposures. The motion is presumably due to creep of the film in the film carrier as the other hologram from this exposure (other 70 mm piece of film), shows parallel fringes closer together, implying the other film moved in the same direction, only further. The circle indicates the location of a side-core hole completed 3 minutes prior to the first exposure of this hologram. Time-dependent deformations which would distort the fringes are notably absent.

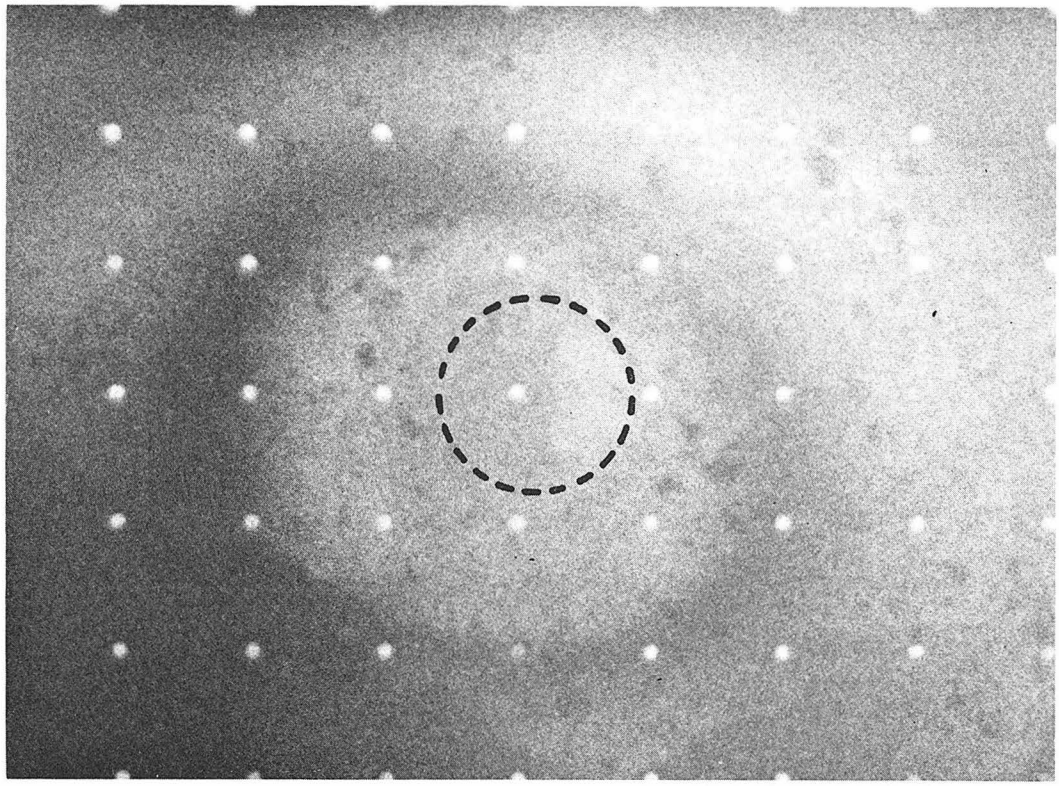

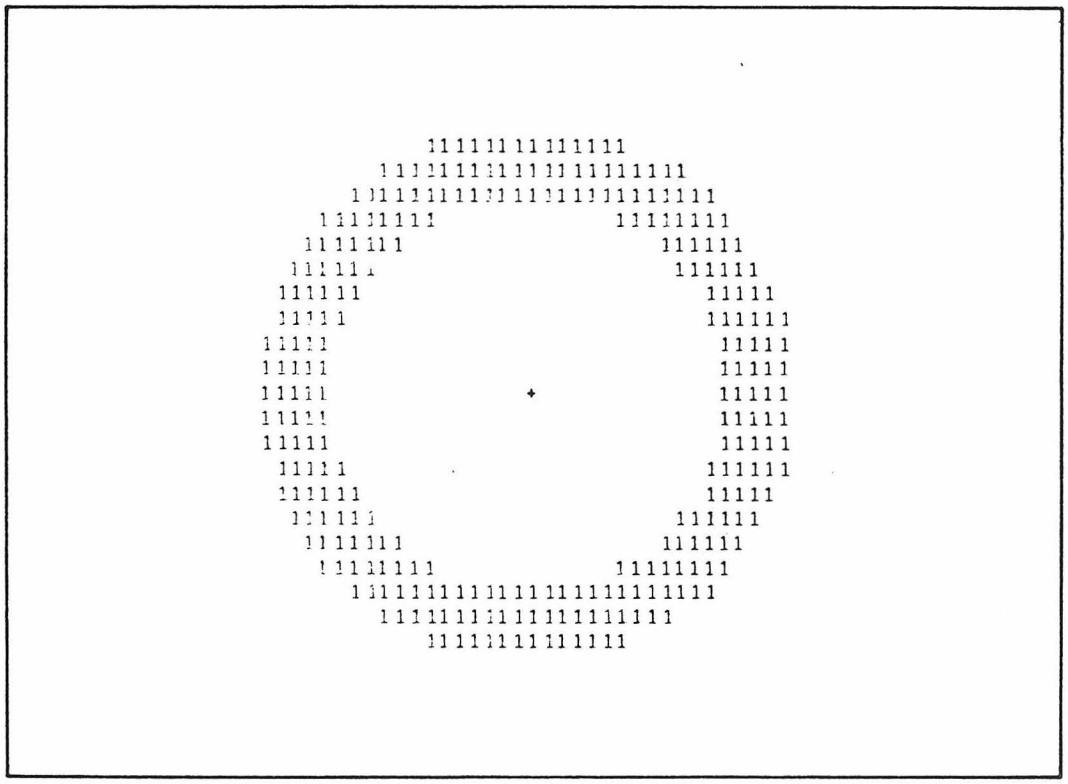

Figure 4-10 Photographed fringe pattern from laboratory strain-relief experiment on unstressed tuff. Motions are vertical and less than .0005 mm. A calculated fringe pattern is shown underneath for comparison.

holographic stressmeter could drill a strain-relieving hole into the rock, replicating the configuration of the borehole tests. As the sample block was unstressed along its boundaries, we intended that this test would separate the deformations associated with the far-field stresses acting on the rock, in situ, on the borehole wall from deformations due to all other possible sources.

The experiment was conducted as much as possible the way tests in the U12n.14UG-1 borehole had been conducted. The drilling was accomplished over a similar time period and the usual vacuum system was employed to remove the drill cuttings. The side-core hole was drilled with the same 1.3-cm-diameter drill bit (recently resharpened), that was used for the measurement shown in figure 4-8, and the hole was drilled to 1.2 cm depth between the two exposures. Thus the laboratory experiment should be directly comparable to the tests done in the borehole at NTS.

The resulting reconstructed interference hologram, shown in the upper part of figure 4-10, displays a single circular fringe. The very existence of the fringe implies that optical stability was successfully maintained. The array of white spots, generated in the photographic process, is located in the plane of the rock surface. They are spaced on a 1 cm grid for reference in analyzing the photograph.

One property of the circular fringe shown in figure 4-10, but not visible in a photograph, is that the location of the fringe is highly insensitive to the position of the observer. Recall, from the discussion of figure 3-1, that fringes due to predominantly vertical

motions are insensitive to the location of the observer. Thus we can infer that the circular fringe is due to motions normal to the surface. In addition, recall that in the discussion of figure 4-7 we pointed out that a circular fringe centered on the side-core hole could not form by any simple displacement of the surface or deformation of the surface by a plane state of stress. Some other process is responsible for producing the displacements this feature represents.

At this point we have not identified what this process might be. However, the motions which it produced are easily determined and modelled since they are constrained to be primarily normal to the surface. To simplify the following discussion assume for the moment that both the illumination beam ($\vec{L}$ in figure 3-1), and the observer beam ($\vec{O}$ in figure 3-1), travel normal to the deforming surface. This is in fact not strictly true, but as the relevant factor scales as the cosine of inclination of these beams to the normal (a small angle), for motions normal to the surface, this is a useful approximation. A phase shift of 1/2 wavelength is required to produce a first-order interference fringe. If the surface displacement is parallel to the incoming and reflected beams ($\vec{L}$ and $\vec{O}$), this only requires a displacement of 1/4 wavelength, either toward or away from the film. The second-order fringe develops with a path-length change of 3/2 wavelength, or a displacement of 3/4 wavelength. The photograph of the interference hologram shows only one fringe so the motions must be less than 3/4 wavelength or .00047 mm. At the points where the fringe appears, the motion is .00016 mm.

The simplest form to assume for these motions is that they are

largest at the edge of the side-core hole and decay linearly with increasing radial distance. In fact, the optical recording geometry is not quite as simple as assumed above. The calculation to produce the simulated fringe pattern in the lower part of figure 4-10 accounted for the actual geometry. To generate the simulated fringe pattern the motions were defined to be one wavelength at the center of the side-core hole, decaying linearly to zero at 2.5 cm radius. Obviously no fringes can form within the 0.64 cm radius of the hole. The resulting fringe pattern replicates the observed fringe fairly well. Furthermore, experimentaion with various displacement fields showed that the observed fringe must be first order, otherwise additional fringes would be observed, so the motions are very well constrained. Perhaps the decay is not linear, but only at the points on the surface indicated by the fringe can the motions be approximately 1/4 wavelength. Inside and outside the circular fringe the motions must either be less than this or fall between 1/4 and 3/4 wavelengths. It is logical to assume that the disturbance, whatever its origin, is greatest at the edge of the side-core hole and tends to zero at large distances.

It is possible that frictional heating generated by drilling induced this localized swelling. Alternatively, it is possible that small cracks parallel to the surface opened in response to the vibration of the drilling. It is even possible that the surface depressed, rather than rising, but a promising mechanism is lacking. What is important is that the motions that did occur are so small, much smaller, by an order of magnitude, than the motions observed in the trials conducted in the

U12n.14UG-1 borehole. This implies that the motions recorded by the stressmeter, in the borehole, are indications of the far-field stress rather than anything else.

We cannot conclude from this that residual stresses might not pose a problem for interpreting the data from in-situ stress measurements made with the holographic stressmeter, but this test does demonstrate that residual stresses are not important in the case of the particular volcanic tuff with which we worked. In general, residual stresses which are locally self-equilibrated on the scale of the diameter of the side-core hole should not interfere with measurements using the approach of the holographic stressmeter because it records the whole displacement field over a region five to ten side-core-hole diameters in dimension. This is a distinct advantage that this technique offers over point strain measurements, as they are affected by small-scale residual stresses. However, larger-scale residual stresses, where they occur, would complicate the interpretation of the displacement field in terms of far-field stress, as it would for point strain measurements as well.

Theoretical Sensitivity of the Stressmeter

Suppose that all of the instrumental limitations and bugs could be worked out of the holographic stressmeter. If it then flawlessly recorded the interference holograms of strain-relief displacements, what far-field stress fields could it distinguish? The next three figures (figures 4-11, 4-12, and 4-13) and the associated text address this question.

Since the holographic stressmeter is intended to operate in a vertical hole, the obvious way to access stresses deep in the crust from the surface, we will only consider the situation from this point of view. Also, we adopt the stress field determined by Haimson et al. (1974) for N-tunnel: 70 bar vertical principal stress, and 35 and 88 bar horizontal principal stresses, as a representative state of stress. This stress state happens to share a principal direction with the Z axis of a vertical borehole, but as equation 2-4 indicates, this is not required for the interpretation of measurements made with the holographic stressmeter. The alignment produces zero shear stresses at the borehole wall, however, as shown in figure 4-8, shear stresses are identifiable by the rotation of the symmetry observed in the fringe patterns. Hence arbitrarily oriented far-field principal stresses can be fully constrained. This alignment just reduces the range of possible fringe patterns and the number of free parameters to consider in these examples.

Although determination of the far-field stress tensor requires measurements at only three select azimuths, it is not clear that this is the optimal way to operate in a borehole. Figure 4-11 shows the expected stresses, displacement fields, and resulting fringe patterns for four different azimuths, equally spaced at 30^{o} intervals around the borehole. The top of the center column depicts the far-field stress field and borehole coordinate system. In each of the four rows the center column displays a view of the borehole and a sketch of the location of the side-core hole around the circumference of the borehole.

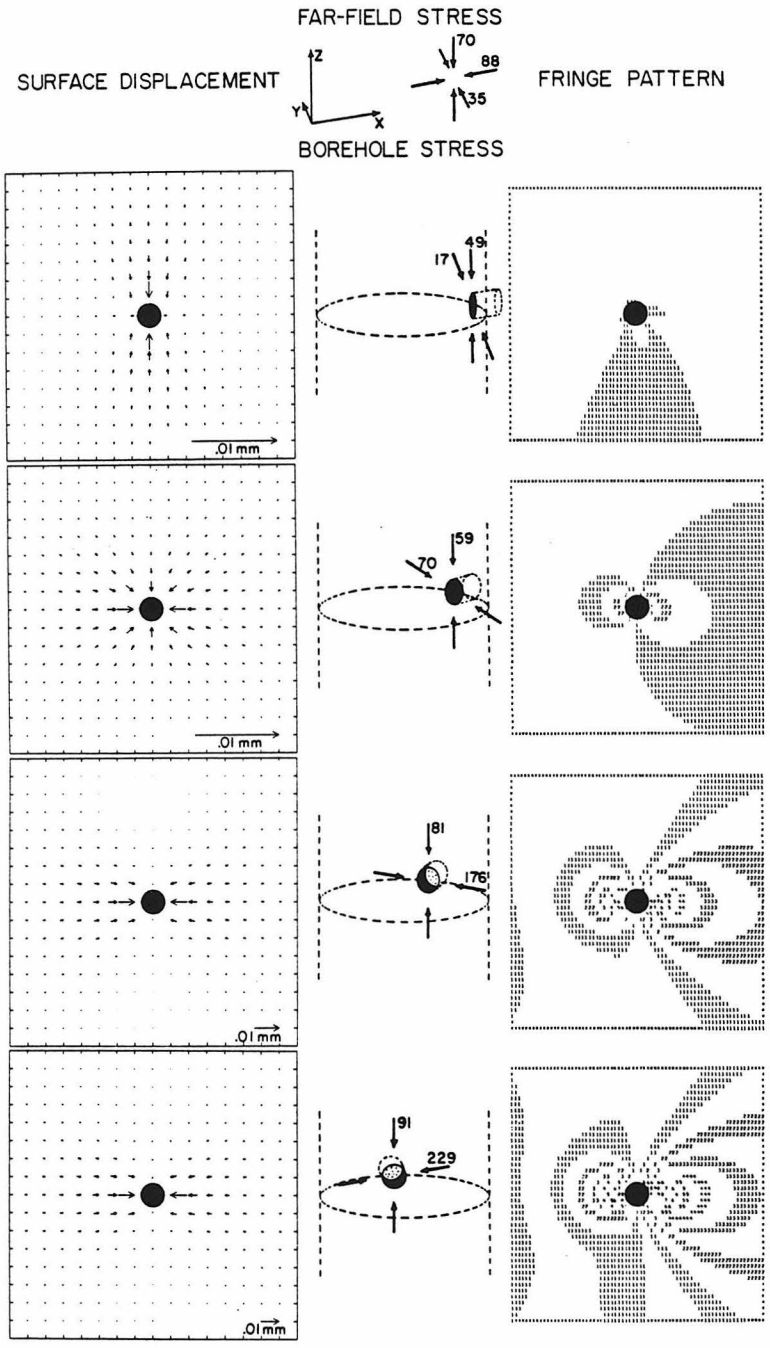

Figure 4-11 Calculated displacement fields and fringe patterns for strain-relief measurements at four azimuths in a vertical borehole. The far-field stresses are indicated by the figure at the top. The values in the center column indicate the plane-stress state prior to drilling the side-core hole, for each azimuth.

The magnitudes of the two normal stresses acting in the vicinity of the side-core hole are also indicated. We show the corresponding displacement field, calculated for the plate-with-a-hole model, in the left column for a 14-cm-square grid of points. A .01 mm displacement vector, plotted in each figure, indicates the scale. In the right column we show the fringe pattern produced from the displacement field, for each row, again for a 14-cm-square surface centered on the side-core hole. (Note that to orient the displacement field and fringe pattern properly in the borehole they must be rotated 180^{o} about the side-core hole axis.) The substantial variation in the stresses acting on the borehole wall at the various azimuths yields readily distinguishable fringe patterns, as illustrated, demonstrating the sensitivity of the stressmeter measurements to azimuth relative to the horizontal principal stresses.

The next two figures are based on the framework of figure 4-11, with a few modifications. Each row in figures 4-12 and 4-13 corresponds to the azimuth indicated in the center column of the corresponding row in figure 4-11. The fringe patterns in each column are calculated for the far-field stress state defined in the stress figure above the column. Only the calculated interference fringe patterns are shown, and these are for a 10 cm square surface centered on the side-core hole. In the lower left corner of each fringe pattern is a plane-stress configuration indicating the actual stresses acting on the borehole wall which were employed to calculate the displacements using the plate-with-a-hole model. (The parameters employed are as follows:

Poisson's ratio, 0.2; Young's modulus, 200 kbar; hole diameter, 1.3 cm.)

Figure 4-12 illustrates the impact of exchanging the magnitudes of the principal stresses, keeping the principal axes fixed, to demonstrate what kinds of stress fields the stressmeter ought to distinguish. The left column is identical to the right column of figure 4-11, except for the size of the region depicted. Each column of four fringe patterns represents a possible data set for a complete measurement to determine the far-field stress tensor at some level in a borehole. As each column is distinct from the other two, the stressmeter measuring approach should be able to distinguish these three stress states when deployed in a borehole.

It is difficult to quote a precise sensitivity to be expected from the stressmeter operating under ideal conditions. Several factors contribute to the ultimate sensitivity. Since the holographic recording technique detects displacements, the side-core hole size, which affects the displacements as a function of the square of its radius, influences the sensitivity. The larger the hole size, the greater the sensitivity; however, as there are finite limits to the displacements which can be recorded due to the resolvability of the fringes, this yields a sensitivity proportional to the absolute stress level. In other words, at 50 bars ambient stress the sensitivity might be 10 bars, while at 500 bars it would be 100 bars. Furthermore, the modulus of the rock affects the stressmeter's sensitivity. Equations 4-2 show that the displacements are inversely related to the modulus of elasticity (E,

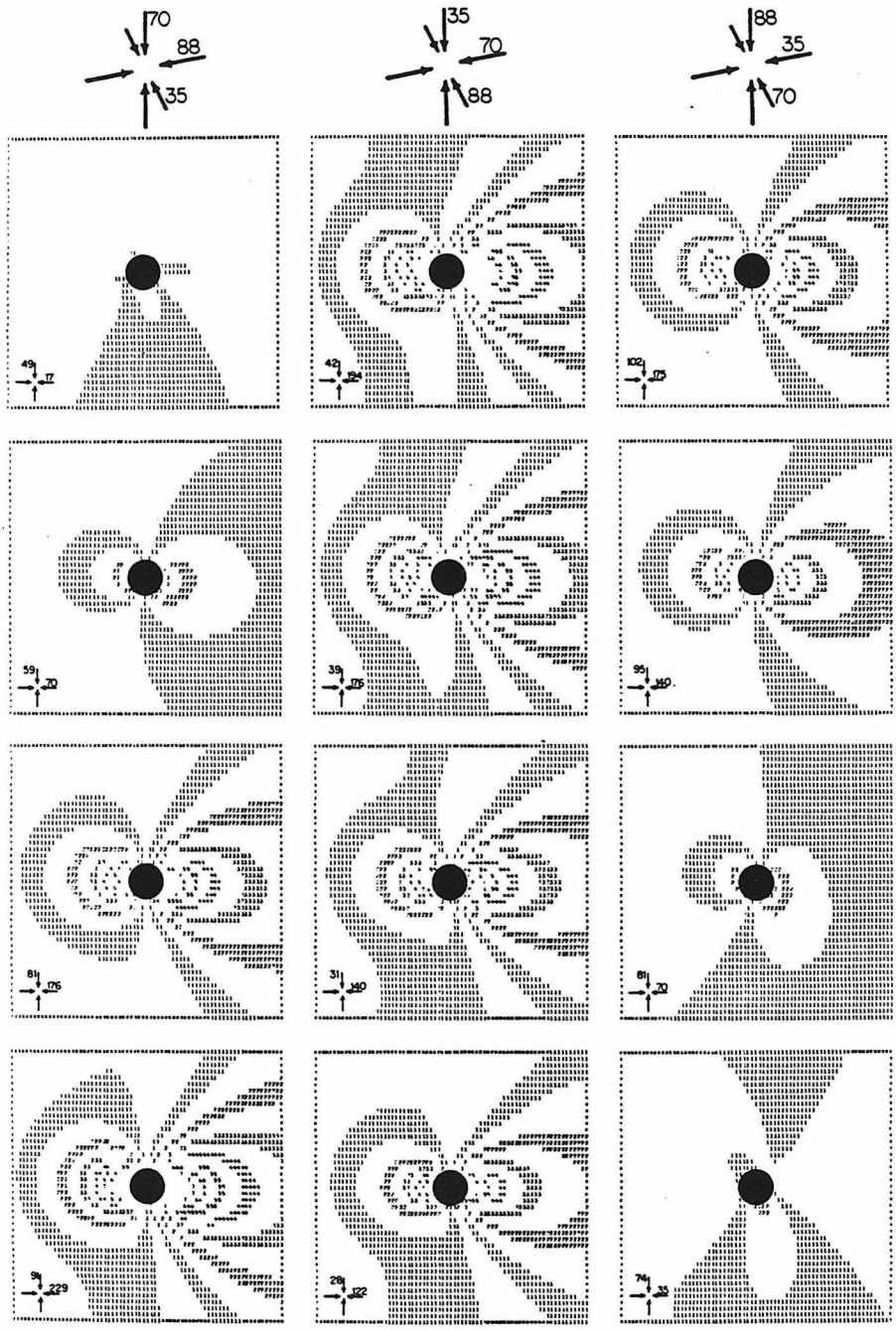

Figure 4-12 Fringe patterns for the four azimuths of figure 4-10, for three stress states related by permutations of the principal stresses. The stress states are shown at the top of the figure.

Young's modulus). However, within the limits of acceptable side-core hole diameters, one can compensate for the stiffness of the rock by adjusting the size of the side-core hole. This presumes that the elastic properties and the magnitudes of the stresses are known, at least approximately, prior to the stress measurement.

While tempered by the concepts described in the preceding paragraph, figure 4-13 presents a rough illustration of the sensitivity expected for the holographic stressmeter. The center column shows the fringe patterns for the standard stress state again, as they were shown in the preceding two figures. The left column depicts the fringe patterns for the case where the maximum principal stress is increased 20 bars relative to the standard. The right column illustrates the fringe patterns if all of the principal stresses are increased 20 bars above the standard values. While some of the individual fringe patterns among the three columns are quite similar, largely because of similarity among the resulting plane stress states at the borehole wall, the three columns, each taken as a whole, are readily distinguished. Hence we conclude that the instrument is likely to determine the magnitudes of the principal stresses with a precision of about 20 percent of their values. The accuracy will of course depend upon the accuracy of the determination of the elastic moduli and on the modelling used to interpret the displacements, as, for example, the plate-with-a-hole model which obviously overestimates the deformation associated with the side-core hole.

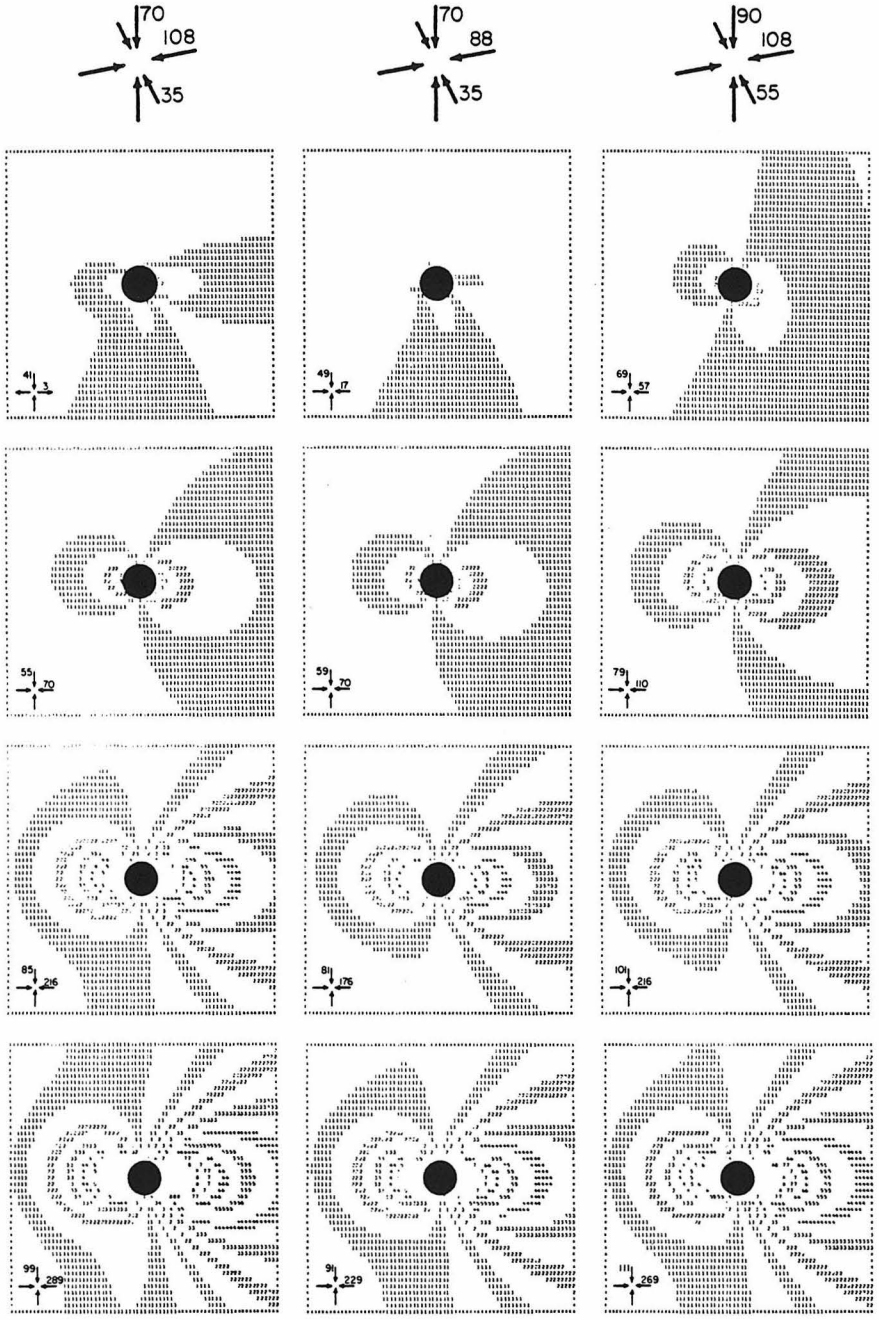

Figure 4-13 Same as figure 4-11 except that the reference state is perturbed by 20 bar increments to demonstrate the stressmeter's sensitivity.

Inverting Fringes for Displacements

Up to this point our discussion of interpreting recorded interference fringe patterns has focused on comparing observed or photographed fringes to patterns calculated from displacement fields resulting from likely states of stress. Such an approach is adequate where the fringes are indistinct, but evident to the unaided eye. Furthermore, it is appealing because an observer can actually view the fringe pattern in the holographically reconstructed virtual image. However, inverting the fringes observed directly for the displacement vectors, for various points on the deformed surface, offers specific advantages. We will show below that the fringes recorded contain enough information to uniquely determine the three-dimensional vector displacement, except for the sign of the motion, for every point on the deformed surface located within approximately 5 cm of the axis of the main recording window. Usually this window is centered over the side-core hole so the displacements can be determined for a radius of 5 cm around the side-core hole. The virtue of this approach is that determining the stresses acting on the borehole wall reduces to fitting calculated displacement fields to a number of measured displacements, a task well suited to computer analysis. Since the fringe patterns change with the observation point, to convert equivalent information to computer accessible form starting from fringe patterns would require digitizing many photographs of the fringe pattern taken from various angles, and that doesn't even consider the problem of relating fringes from one vantage point to the same fringes recorded from another.

Furthermore, this approach has the desirable feature that poor holograms that do not photograph well, but which do produce interference fringes that are visible to the eye, can still be interpreted. We have not actually used this analysis, except to test it on simple cases with linear fringes, as it isn't warranted by the data we have collected. However, we discuss it here because it provides a framework to examine what information is retrievable from the interference holograms.

The approach to determining the displacements of various points directly from the reconstructed interference hologram requires one to change perspective back to the framework of figure 3-1. In that discussion we considered how a single point appeared, viewed from many observation points rather than the subsequent analysis which focused on viewing all of the points on the surface from a single observation point, as a reconstructed hologram is actually viewed.

Figure 4-14 depicts a view of a point P located near the edge of the side-core hole. The unit vectors $\vec{L}$ and $\vec{O}$ are directed from P toward the source of laser illumination and the observation point on the film plane, respectively. Hence this is a three-dimensional analog to the two-dimensional example shown in figure 3-1. To simplify the example, assume that the displacement of point P, $\vec{\Delta}$, lies in the plane of the surface. Clearly changing the observation point only changes the unit vector $\vec{O}$. An interference fringe denotes a locus, either of points on the surface, or points of observation, for which the change in path length due to the deformation is constant. All that is required to conserve the change in path length due to displacement $\vec{\Delta}$ of a point P

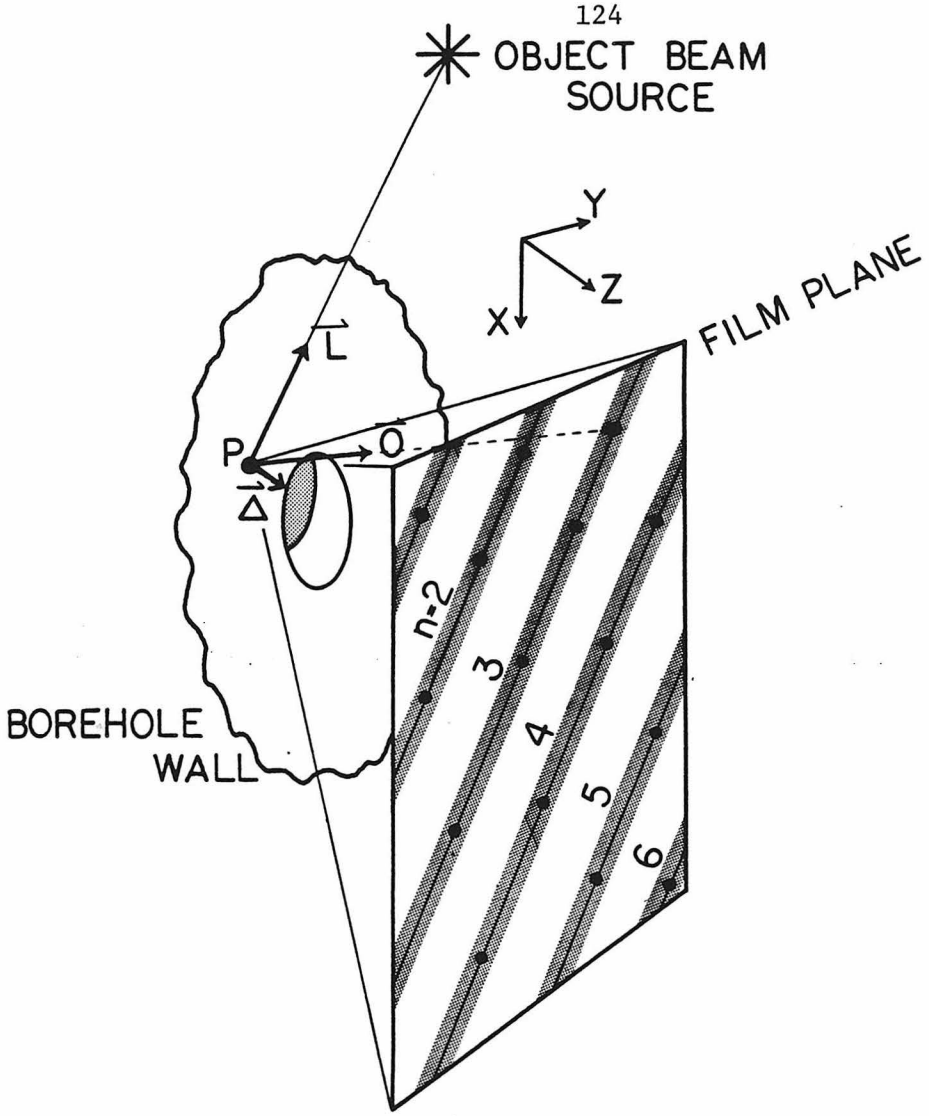

$$\vec{\Delta} \equiv (dx, dy, dz)$$

$$\vec{\Delta} \cdot (\vec{L} + \vec{O}) = \frac{2n-1}{2} \lambda \Rightarrow \text{FRINGE}$$

$$dx(L_x + O_x)_i + dy(L_y + O_y)_i + dz(L_z + O_z)_i = \frac{2n_i - 1}{2} \lambda$$

Figure 4-14 Mapping onto the film plane of all fringes occurring at point P on the deformed surface, as seen from all observation points on the film plane. This leads to an approach to inverting fringes for vector displacements, discussed in the text.

for a set of observation points is to require that the dot product of $\vec{\Delta}$ and $\vec{O}$ be constant for those points. Thus the angle between $\vec{\Delta}$ and $\vec{O}$ must be constant, constraining the points with constant change of path length to lie on the intersection of the film plane with a family of conical surfaces originating at P with central axis $\vec{\Delta}$. Each order of fringe corresponds to a different conical surface. By simple geometric arguments these curves will be perpendicular to the direction of dispacement $\vec{\Delta}$ at their closest approach to P thus yielding the direction of displacement. Since the geometry of the recording system constrains $\vec{O}$ to be steeply inclined to the surface, the loci of points which have the same change in path length is almost a straight line on the film plane. (The axial angle of the conical surfaces is close to 180^{o}.) Consequently these lines of constant change in path length are approximately perpendicular to $\vec{\Delta}$ everywhere. Figure 4-14 shows six such lines labeled according to the order of the fringe represented. The hologram never appears this way. It is effectively a mapping onto the film plane of all of the observation points from which particular fringes are seen at point P.

One approach to actually extracting this information from a hologram is to place an acetate overlay on the film while it is illuminated by the reconstructing laser and reproducing the virtual image. Then, perhaps with a felt-tipped marker, one marks all of the locations on the acetate where a fringe is seen at the particular point in the scene. The order of the fringe is determined by counting in toward the side-core hole from the first-order fringe which will always

be the outermost fringe. This yields a pattern like the one shown on the film plane in figure 4-14. The virtue of this approach is that the fringes need only be sufficiently distinct to see with the unaided eye. How efficient this process might be has yet to be determined, but it shouldn't be necessary to apply it to more than ten well-chosen points to adequately constrain the displacement field.

Once the data are converted into the form of fringes mapped onto the film plane, shown in figure 4-14, solution for the displacement vector $\vec{\Delta}$ is straightforward. Two strategies are possible. If it is reasonable to assume that the displacement is primarily in the plane of the surface, then its direction is perpendicular to the mapped fringe lines, presumably directed toward the side-core hole in a compressive stress regime. The spacing of the mapped fringes indicates the magnitude of the displacement. (This occurs because the derivative with respect to the angle between $\vec{\Delta}$ and $\vec{O}$ of the dot product of $\vec{\Delta}$ and $\vec{O}$ is proportional to the magnitude of $\vec{\Delta}$.) Alternatively, if the displacements are assumed to have non-zero normal components we can treat the problem more formally by the method of least squares. The data could be in the form of the points indicated by dots on the mapped fringe lines in figure 4-14. At each point $\vec{L}$, $\vec{O}$, and n are known. We want to determine the three components, (d_x, d_y, d_z), of the displacement $\vec{\Delta}$. The problem is defined by equation 4-3.

$$d_x (L_x + O_x)_i + d_y (L_y + O_y)_i + d_z (L_z + O_z)_i = \frac{2 n_i - 1}{2} \lambda \qquad (4\text{-}3)$$

Equation 4-3 is easily solved, by the method of least squares, for the desired components of displacement in terms of our observation points. Again, we assume under compressive stress that all displacements are toward the side-core hole and thus select the sign of n appropriately, removing the only ambiguity in the determination. Hence we can determine the three-dimensional vector displacements for as many individual points on the surface surrounding the side-core hole as we desire.

The next step is to determine the plane stress field which best reproduces the measured strain-relief displacements. This is probably best done by computer modelling and inversion and is not treated here as we have not yet obtained data to warrant such a complete analysis.

Discussion and Conclusions

In the course of developing a new instrument to measure some physical property in a manner different from existing techniques, two issues come into focus. The first is whether or not the measuring strategy, as realized in the prototype instrument, actually results in measuring the desired property. The second asks at what sensitivity can the particular measurement approach operate. We have addressed both of these concepts in the context of the holographic stressmeter.

Interference holograms obtained from trials of the stressmeter in a borehole drilled from n-tunnel into the ash-fall tuffs of Rainier Mesa, Nevada Test Site, display complex lobed patterns of interference fringes. We show by comparison of these data to computer simulated

fringe patterns that these cannot result from simple motions of the instrument or other forms of instability. By modelling the displacements on the surface of the borehole using the analog of a thin plate containing a through-going hole under a state of plane stress, we demonstrate that the observed interference fringes can be approximately replicated by computer simulated patterns for reasonable values of stress and elastic properties. We did not measure the relevant elastic properties in situ, but applying realistic values, the stresses expected on the borehole wall from other determinations of the in-situ stress in the vicinity of our test site yield good fits to our observed data. We have not made the three measurements distributed azimuthally around the borehole that are required to determine the complete far field stress tensor. However, demonstrating that the stressmeter successfully measures the stress at one azimuth implies that with three measurements it should yield all six independent components of the desired far-field stress.

We show with a laboratory experiment on an unstressed specimen of the tuff from the n-tunnel borehole site that there is no evidence of any other phenomena, besides the in-situ stress, causing the strain-relief displacements that we recorded in the trial borehole. Thus we have eliminated residual stresses, induced thermal stresses, and other imaginable or unknown processes that might conceivably have produced the effects we have attributed to the far-field stress state that we sought to record. From this we conclude that the instrument is actually recording data which can be interpreted in terms of the

far-field stress.

Comparing computer simulated interference fringe patterns for a variety of stress states and perturbations therof, we anticipate that the stressmeter should ultimately measure stress values with a precision of about 20 percent of the value determined. The accuracy, however, will be influenced by the accuracy to which the elastic properties are known, and will depend on how well one knows the factor relating the calculated values for the displacements to the actual displacements due to strain relief.

The development of the holographic stressmeter is presently at an intermediate stage. It has not yet attained the status of a field logging instrument ready to be employed to measure stress, yet it is more than an experimental concept. The discussion in this chapter demonstrates that the measurement approach can be physically realized in a borehole instrument, and with some further development, the expected capabilities promise to yield a productive geophysical tool.

CHAPTER 5

Discussion and Future Approaches

Introduction

The next step in developing the holographic stressmeter is to design a smaller and lighter prototype which incorporates some desirable features the current instrument lacks. We discuss below some of the limitations inherent in the design of the holographic stressmeter and suggest potential improvements in the instrument yet to be exploited. These constraints and new possibilities will presumably guide the design and fabrication of a new holographic stressmeter prototype aimed at reducing the acceptable borehole diameter to $\sim$15 cm, enabling measurement of stress in a variety of existing boreholes available for such experiments.

Physical Constraints on the Stressmeter Design

One approach to miniaturizing the instrument is simply to scale down each of the physical components by some factor. However, proper scaling of the experiment implies scaling the wavelength of the laser used for the holographic recording. This is impossible without abandoning the visible region of the spectrum and the holographic technology upon which the technique relies. Substituting a shorter wavelength laser, an argon laser for example, would gain only small improvements in sensitivity. An argon laser operating at 0.5145 micron

wavelength (blue-green) would increase the sensitivity approximately 20% compared to the He-Ne laser the prototype currently employs. If we assume that a scaled version of the instrument will nevertheless employ a He-Ne laser for the holographic system, we must consider the limitations this imposes on miniaturization.

Ultimately sensitivity trades off against the physical size of the instrument. The minimum displacement of points surrounding the side-core hole required to produce a first-order fringe provides a rough estimate of the sensitivity. This minimum value varies as a function of the position on the surface, the direction of displacement, and the location of the observer. (Figures 4-8 and 4-11 illustrate this variable sensitivity.) However, based on numerical experiments equivalent to those shown in figure 4-7, the displacements must be of the order of .001 mm if they are confined to be in the plane of the surface, .0003 cm if they are normal to the surface. In-plane displacements dominate, particularly at larger distances from the side-core hole, as indicated by finite-element calculations discussed in Chapter 4, so the .001 mm figure is a better guide. The stresses at the borehole wall are independent of the borehole diameter, as shown in equations 2-1, so changing the borehole diameter produces no direct effect. The strain-relief displacements at any particular point scale as the square of the diameter of the side-core hole (equations 4-1). Consequently, reducing the diameter of the side-core hole rapidly reduces the displacements at any particular location. We generally observe a halo surrounding the side-core hole in which interference

fringes do not form. This may result from excessive motions or some unidentified process. It is possible, even likely that the size of the halo is proportional to the diameter of the side-core hole. If this is true, the sensitivity will actually scale linearly with the diameter of the side-core hole rather than as the diameter squared. This occurs because one can determine the displacements of points at the same scale distance from the edge of the side-core hole, in other words, at smaller absolute radial distance for smaller side-core holes. The limits due to visual resolution of the interference fringes would eventually introduce the next practical limit. We have not yet approached this limit in the field trials. However, in laboratory experiments a density of 4 fringes/cm has been easily resolved and photographed. The ultimate limit is at least twice this density.

The diameter of the side-core hole is constrained from both above and below. It must be sufficiently large for the particular stress conditions at the borehole wall to generate displacements which produce at least a first-order fringe (n=1 in equation 3-1), and it must also be at least several times the characteristic grain size to avoid violating assumptions of homogeneity. On the other hand, too large a diameter for the side-core hole violates the simplifying assumptions used in interpretation of the displacements, as discussed in Chapter 4.

Suppose for a moment that the instrument operated in a 15-cm diameter borehole and drilled a 0.6-cm diameter side-core hole. This would preserve the same ratio we employed in our trials in U12n.14UG-1. Since the strain-relief displacements recorded in those trials were

somewhat too high for the recording scheme, assume that a 0.6-cm diameter side-core hole would have been more appropriate. Suppose also that we were to deploy the stressmeter in a fine-grained granite with a 1.0 megabar Young's modulus, approximately five times the modulus of the tuff in n-tunnel. Then the corresponding strain-relief displacements would occur at four to five times the stress, or four to five times the depth of the NTS experiments. That implies depths between one and two kilometers. Thus the measurement approach will function at depths of this order with an instrument designed to operate in a 15-cm diameter borehole. Adjustment of the sensitivity of a 15-cm instrument by varying the size of the coring bit will still accommodate a substantial range of stresses and elastic moduli without violating the limits discussed above. However, halving the dimensions again poses substantial difficulties, even if it could be physically realized. The borehole diameter would be 8 cm and the side-core hole only 0.3 cm in diameter. This approaches the grainsize of many crystalline rocks and is only several grain diameters for a coarse sandstone. Two potentially serious problems arise. First, the areal extent of substantial strain-relief displacements becomes so small that the interference fringes may no longer be resolvable. Second, the assumption of homogeneity fails. Third, residual stresses, which are commonly observed on the scale of the grainsize, threaten increasing importance (Friedman, 1972). Thus at this size residual stresses are more likely to complicate interpretation in terms of the local stress field. Consequently, the rock properties may impose a practical limit to the

miniaturization desirable in addition to the physical constraints on miniaturizing the constituent components.

At the scale considered, none of the individual components present serious obstacles to miniaturization. I do not, however, mean to belittle the task. It will require much ingenuity, particularly in engineering the drilling module and in designing the holographic optical chassis to permit alignment without disassembly of the entire unit.

Potential Improvements to the Stressmeter

Reliance on external measurements of the elastic properties of the rock exposed at the borehole wall poses a severe limitation on the accuracy of the holographic stressmeter and all other stress measurement techniques that rely on strain relieving the host rock. Laboratory measurements test samples whose physical properties may have been altered by environmental changes from the in-situ state, by efforts required to obtain the test samples, coring or blasting for example, or by physical changes induced by relieving the in-situ stress acting on the rock in its original location, perhaps by causing microcracks to open or propagate. Thus it would be highly desirable to measure the elastic properties of the rock involved in a particular measurement right in the borehole.

Several approaches to measuring elastic properties of rock in a borehole are possible. Acoustic logging tools most commonly serve this function, however, while they offer a reliable measurement, it is not actually the desired measurement. Since the dynamic measurements

obtained with acoustic techiques essentially provide the derivative of the stress-strain relationship, any departure from linear-elastic behavior will result in a divergence between the dynamic elastic moduli and the static moduli which are appropriate for interpreting strain-relief displacement data. Hence, an alternate approach would be preferable.

One possible scheme could be easily incorporated into the holographic stressmeter. Employing the same field of view and the same holographic recording technique, displacements of points on the borehole wall due to an applied load could be measured directly. Hence, incorporating some mechanism for placing a known load or traction on the borehole wall, at the site of the future strain-relieving side-core hole, would enable the stressmeter to record holographically the displacements resulting from the application of the known force. If the force were applied normal to the borehole wall this could be approximated by the classical Boussinesq problem in elastostatics, that of a point force applied at the surface of a semi-infinite solid (Timoshenko and Goodier, 1934, p. 398). The solution for the surface displacements occurring under this loading configuration are shown in equations 5-1. These expressions are valid only for the region outside a small radius around the origin as the stresses and displacements are unbounded at the origin in the elastic solution.

Radial displacement:

$$U_{z=0} = \frac{-(1-2\nu)(1+\nu)\ P}{2\pi E r} \qquad (5\text{-}1a)$$

Normal displacement:

$$W_{z=0} = \frac{(1-\nu^2)\ P}{\pi E r} \qquad (5\text{-}1b)$$

The displacements depend upon both Young's modulus and Poisson's ratio, although the dependence on the latter is substantially weaker than on the former. Furthermore, the normal and radial displacements depend upon a different algebraic combination of the two elastic constants so that both could be determined, in principle, with sufficiently high quality displacement data. More likely one would be forced to either measure Poisson's ratio by some other method, or assume an appropriate value. Such an approach is better than it might appear as both the solution to the Boussinesq problem and the solutions to the elastic problems discussed in association with the foregoing analysis are only weakly sensitive to the value of Poisson's ratio, while the strain-relief displacements on the borehole wall are inversely proportional to Young's modulus.

Incorporating a loading device which can act with a specific force in the same space occupied by the drilling head when it is extended to drill the side-core hole will require ingenuity. The procedure for measuring stress would change only to the extent that two double exposure holograms would be recorded at each point, the first to measure the elastic moduli, the second to measure the strain relief due to the

side-core hole. This would increase the time for a complete stress measurement by two to six minutes, depending on whether the elastic moduli were measured at each azimuth or only once at each level in a borehole. If accomplished, this strategy would relieve the principal source of inaccuracy limiting this approach to measuring in-situ stress.

Many of the boreholes of geophysical interest are filled with water, hydrocarbons, or drilling mud. We have demonstrated that the instrument functions in a dry borehole and Schmidt et al. (1974) showed that the measurement strategy performs in a water-flooded environment created in the laboratory. Designing the holographic stressmeter to work in a mud or oil filled borehole is a serious challenge, if it is possible.

As the recording system is fundamentally an optical system, any fluid between the instrument windows and the borehole wall must be almost perfectly transparent. A water-flooded environment requires a system for clearing the water of all rock flour generated by the side-core hole drilling process. In the laboratory we found water with suspended core-drilling debris was cleared adequately by exchanging it in five cycles through a fine paper filter (Ultipor 0.2 micron, disposable). If the fluid in the hole contains other suspended particles, these too must either be removed, or the volume of fluid replaced with water. This latter approach is probably the only satisfactory method of working in a mud-filled borehole. However, it requires a system to isolate, in as small a volume as possible, the windows and the region on the borehole wall surrounding the side-core

hole to minimize the amount of fluid required to flush the volume clear. Since water and mud are not likely to materially influence the nature of the strain-relief displacements, just complicate the experimental technique, incorporating such systems and attempting to operate in hostile environments are realistically appropriate only after the holographic stressmeter is fully proved in dry holes free of these difficulties.

Conclusions

The holographic stressmeter is still an experimental technique for measuring in-situ stress in crustal rocks. Theoretically it can be expected to measure all six components of the far-field or virgin-rock stress tensor, perhaps without requiring independently determined values for the elastic properties of the rock if the suggested, on-board moduli-measuring system is incorporated. We have shown that the measurement technique functions in a borehole environment and yields at least qualitatively consistent data based on the stress state expected at the trial location. Our laboratory control experiments demonstrate that other effects, besides the applied stress, such as induced heating or residual stress, produce much smaller contributions to the displacement field than were observed in our borehole trials, implying that the deformation observed in the field resulted primarily from the in-situ stress field. This conclusion is further supported by modelling of the observed fringe patterns by a stress system which is reasonably consistent with the measured state of stress as determined by other

techniques. Thus we conclude that the holographic stressmeter does in fact measure the in-situ stress field. Modelling of possible fringe patterns suggests an ultimate precision of approximately 20%. Constraints imposed by the field borehole trial site prevented deploying the stressmeter at the three azimuths required for a complete determination of all components of the in-situ stress tensor, but as the three measurements are virtually identical, except for the varying stresses encountered at different azimuths around the borehole, measuring the complete state of stress is possible with the current prototype in a borehole with the right characteristics. In summary, the holographic stressmeter offers the promise of evolving into an efficient and desirable geophysical tool. However, substantial refinements and modifications are necessary to attain that objective.

APPENDIX A

Fundamentals of Holography

Introduction

This appendix provides a basic description of the principles of optical holography, generically known as wavefront reconstruction. As the holographic stressmeter relies entirely on holography for recording the minute (<.005 mm) displacements resulting from drilling the strain relieving side-core holes, it is critical that the reader either understand the physics underlying holography or accept its capacities on faith. This discussion is intended to be sufficiently simple and complete that the latter is unnecessary, although sufficient for understanding the formation of the interference fringes upon which this stress-measuring approach is based.

While conventional photography and holography are fundamentally different processes, they both record optical information via a photosensitive emulsion. The recording medium for both techniques is a thin photosensitive layer, the emulsion, which reacts to exposure to light, supported on a sheet of transparent film or glass. All of the photographic and holographic emulsions used in the course of this research are based on silver chemistry and, upon standard processing, are transparent where unexposed to light and tend increasingly toward opacity with increasing total exposure to light, ideally with a linear relationship between exposure and inverse transmittance of the processed

emulsion. In practice the relationship between exposure and inverse transmittance is approximately linear over a finite range of exposure, and one tries to operate within this range. It is important to point out that the photosensitive emulsions are sensitive only to the intensity of light, not its phase. Over the range of linear response they react in proportion to the total light energy absorbed, that is, the integral of intensity over the time of exposure.

Photography, of which the simplest example is a pinhole camera, forms a real two-dimensional image of the illuminated scene and records the intensity of the image over the area covered by the emulsion. All that is recorded is the intensity of this image as a function of position. Information about the phase of the light radiating from the scene is lost. Holography, on the other hand, records the amplitude and phase of the light wave radiated by the scene and permits the reconstruction of that light wave with the correct amplitude and phase at some later time. Consequently, to an observer, the reconstructed wave appears as a three-dimensional virtual image and is indistinguishable from the original scene.

The discussion which follows will concentrate on the principles, technical requirements, and actual procedures for making holograms. As all that is presented here is elementary the reader is referred to Erf (1974), and Robertson and Harvey (1970) for more comprehensive treatments.

Superposition of Coherent Wavefronts

A brief discussion of the meaning of coherence must precede any discussion of the wavefront superposition required to form a hologram. If one experiments with a small solid angle of light rays radiating from a conventional light source, a tungsten filament for instance, one finds that no particular phase relationship persists between the light waves at any two fixed points separated spatially (by millimeters), either parallel or transverse to the beam, for any significant period of time (i.e. nanoseconds). The critical properties of a beam of laser light which make holography practical are that it is monochromatic, and both axially and transversely coherent. Axial coherence means that along a particular ray there is a specific relationship, maintained over time, between the light phase at two separated fixed points. For example, the lasers used in this work have axial coherence of approximately 15 cm. Transverse coherence refers to rays in different parts of the crossection of the laser beam maintaining constant phase relationships with each other. It is the axial and transverse coherence of the laser light source enabling stable constructive and destructive interference of converging wavefronts which is essential to producing a hologram.

Consider the simple example of two converging plane waves. Coherence implies that individual wave fronts, crests and troughs in the analogy to water waves, superimpose to reinforce where they are in phase and cancel when they are one-half cycle out of phase. Figure A-1 shows a sectional view of the case where two coherent plane waves of light impinge upon a very small region of photographic emulsion which is

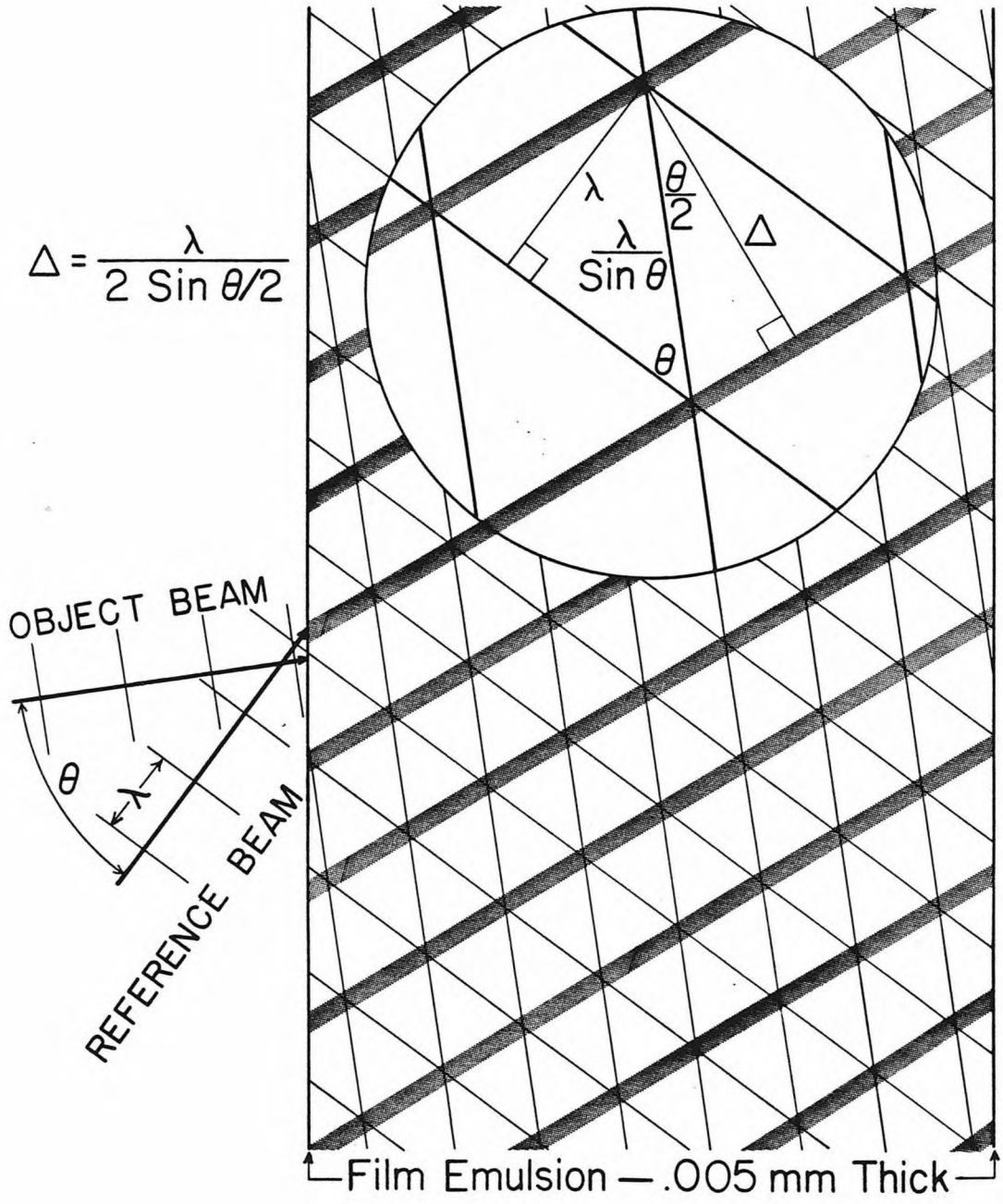

Figure A-1 Microscopic view of reference and object wavefronts interfering in a crossection of the holographic film, yielding the interference fringes shown by crosshatched lines. The geometry of the holographic recording system in the stressmeter requires film resolution of at least 1500 lines/mm.

itself transparent. Notice that the emulsion is shown to be 0.005 mm thick, a standard thickness for holographic films, and the wavelength is 0.0006328 mm, the characteristic wavelength of light produced by a He-Ne laser like the one employed in the holographic stressmeter. Thus the emulsion is about eight wavelengths thick. While in photography the emulsion performs an areal information storage service, in holography it stores information within a volume. We will now consider the volume resolution required to actually record a hologram.

Within the boundaries of the emulsion, in figure A-1, two sets of parallel lines mark the wavefronts on the two converging plane waves. Two converging wavefronts are essential to the process of making a hologram, but we will delay discussion of their roles for the moment. Both plane waves are traveling from left to right through the emulsion. The heavy cross-hatched lines indicate loci of points where the two wave fields are in phase and reinforce. Midway between these cross-hatched lines the two wave fields are one-half cycle out of phase and consequently cancel. Thus the cross-hatched lines indicate the zones of greatest intensity and the sites where there will be the least transmittance after processing. Often these are identified as interference fringes. We will use that term here, but warn the reader that the same term will be used in Chapter 3 to describe what is essentially a different phenomenon, the physically much larger fringes generated in interference holography.

At issue is how close together the interference fringes lie and whether they are sufficiently spaced that the emulsion may resolve them.

By the geometric construction shown in the enlargement in figure A-1 the spacing between fringes is defined by equation A-1, known as Bragg's law, where θ is the inter-ray angle.

$$\Delta = \frac{\lambda}{2 \sin (\theta/2)} \qquad \text{(A-1)}$$

Deferring discussion of the significance of θ, for the moment, consider that the holographic stressmeter optical geometry results in θ approximately equal to 60^{o}, on average. Substituting into equation A-1 yields an inter-fringe spacing equal to the wavelength, or 0.00063 mm. This requires of the holographic emulsion resolving power greater than 1500 lines/mm. It is on this scale that the information recorded in a hologram is stored. Figure 3-9, a photograph of a processed hologram made during a field test of the stressmeter shows that very little information can be recovered by simply examining the hologram in ordinary white light.

Leith-Upatnieks Holography

There exist many different geometries for recording a hologram, but one of the most convenient is the geometry for a Leith-Upatnieks hologram (Leith and Upatnieks, 1964). This technique, shown schematically in figure A-2, is employed in the holographic stressmeter. The left and right halves of the figure show schematic layouts for exposure and reconstruction of the hologram respectively.

To record a Leith-Upatnieks hologram the coherent laser beam is

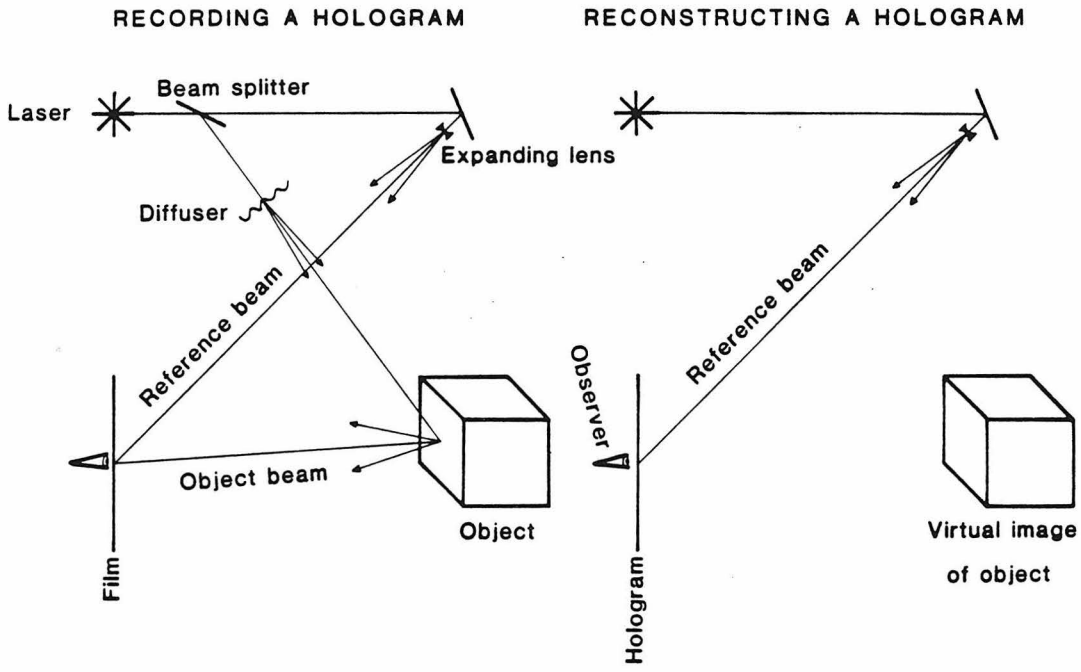

Figure A-2 Schematic diagram depicting the recording and reconstruction of a Leith-Upatnieks hologram. The significant property is that an observer cannot distinguish between seeing the object and seeing its holographically-reconstructed virtual image.

divided, by means of a beam splitter, into two beams. One, which is called the reference beam and represents about 5 percent of the power of the input beam, is optically expanded with a lens and guided by a series of front-surface mirrors to strike the film emulsion directly. The second beam, called the object beam, composes the remaining 95 percent of the power. It is directed by mirrors to an optical diffuser so that it illuminates the scene, such that some of the light scattered by the object falls on the film. The relative intensities of the reference beam and the object beam are adjusted so that the intensity of light striking the film after being scattered from the scene is approximately the same as the intensity of the reference beam. This way when the two wavefronts interact, destructive interference causes complete cancelation.

Clearly there are two conditions which must be met for the formation of the hologram. First, the light reaching the film emulsion in the reference beam must be coherent with the light arriving from the scene, otherwise there will by no interference. This requires careful design of the optical system so that the paths taken by the reference beam to the film plane and the object beam to the scene to the film plane are the same length to within the axial coherence length of the input laser beam. Obviously this limits the size and depth of a scene to be recorded in a single hologram. However, an axial coherence length of 15 cm allows substantial latitude. Second, the interference fringes which form within the film emulsion due to the interaction of the reference beam and light scattered from the scene (figure A-1) must not

move as much as one-half wavelength during the exposure. This implies that phase shifts of as little as one-half cycle during the exposure, in either the reference beam or the object beam, cannot be tolerated. Consequently, the path lengths between the beam splitter and the film for both the object beam and the reference beam must be stable to better than one-fourth wavelength or 0.00016 mm. Thus during the course of exposure, usually several seconds, the film and the object cannot be permitted to move, thermally induced deformation of the optical chassis must be prevented, and motions in any gas or fluid through which either beam passes must be minimized to eliminate path length changes due to temporally varying density. These are substantial constraints on the design of any holographic instrument.

Hologram Reconstruction

The right half of figure A-2 shows the layout for reconstructing a Leith-Upatnieks hologram after it has been chemically processed. All that is required is to illuminate the hologram with the same reference beam used in creating it. Reconstruction produces a three-dimensional virtual image of the scene located exactly where the scene was relative to the film plane when the hologram was made. Since the hologram reconstructs the actual wavefront radiated by the scene, the reconstructed three-dimensional virtual image is indistinguishable to the observer (a camera or one's eye) from the original scene. It displays parallax as one moves the observation point to see around objects in the foreground and it has real depth of field, meaning that

one can focus on the virtual image of the scene at different depths with a camera just as with the actual scene.

It is not self-evident that illumination of the processed hologram with the reference beam should yield the original wavefront. Two separate lines of reasoning will help to demonstrate that this, in fact, occurs. The first is a simple arithmetic argument (Lehmann, 1970). At any point in space a stable and continuous ray of monochromatic light may be described by its amplitude and phase. We are not concerned with its direction of propagation, simply its disturbance at a single point. Since the photographic emulsion is sensitive only to the intensity, or energy density, if we represent the ampitude and phase of the light at the particular point by a complex number, then the intensity is simply the product of this number and its complex conjugate. Allowing R to be the complex value associated with the reference beam and 0 to be the corresponding value for the object beam, each a function of space, the intensity in the film at any point will be I_f as shown in equation A-2.

$$I_f = (R + 0)\cdot(R + 0)^* \qquad \text{(A-2)}$$

Multiplying and expanding this expression yields:

$$I_f = R\cdot R^* + 0\cdot 0^* + R\cdot 0^* + 0\cdot R^* \quad . \qquad \text{(A-3)}$$

The first two terms on the right-hand side are simply the reference and object beam intensities and will be indicated by I_r and I_o

respectively, yielding expression A-4.

$$I_f = I_r + I_o + R \cdot O^* + O \cdot R^* \qquad (A-4)$$

Expression A-4 describes the information stored at each point in the volume of the photographic emulsion comprising the hologram. With the negative photographic process used to record the hologram I_f is the inverse transmittance. However, examination of figure A-1 shows that shifting the relative phase of the two incoming waves by one-half wavelength would exchange the fringes with the transparent zones of the processed emulsion. This leads to the result that it is immaterial whether the hologram is recorded with a positive or negative process as the results are identical so long as the emulsion's exposure response is reasonably linear. Thus in the ensuing discussion we will assume that I_f represents the transmittance function rather than the inverse transmittance.

Illuminating the processed hologram with the reference beam is equivalent to multiplying I_f by R, in this arithmetic construct, yielding expression A-5 for the transmitted wave T.

$$T = R \cdot I_f = R \cdot I_o + R \cdot I_r + R \cdot R \cdot O^* + R \cdot R^* \cdot O \qquad (A-5)$$

The first two terms on the right-hand side are simply the reference beam adjusted by the intensity of the object and reference beams had they been recorded separately. In other words, they are just wavefronts

identical to the reference beam except in amplitude, transmitted through the film. The third term forms what is referred to as the pseudoscopic or conjugate image, usually a real image (light actually passes through the image), but not of importance here. Of greatest interest is the last term which can be reexpressed as $I_r \cdot O$. This is the desired original object beam adjusted by the intensity of the reference beam. Thus the amplitude and phase of the object beam are reproduced at each point in the emulsion volume and form the three-dimensional virtual image (light does not pass through the image) of the original scene. One of the key advantages to the Leith-Upatnieks recording geometry is that these two images represented by the latter terms in expression A-5 are physically separated in space upon reconstruction. This permits working exclusively with the desired virtual image without interference by the conjugate image.

An alternate and perhaps more intuitive explanation for the reconstruction of the original wavefield can be found in a construction based on Huygen's principle. The upper half of figure A-3 shows an expanded laser wavefield illuminating the photographic emulsion directly as a reference beam, and illuminating the scene, in this case a single point in space, as an object beam. The point scatterer reradiates in phase with the illuminating source so that the two wavefields interact within the film emulsion. Assume for simplicity that the reference beam and the object beam reflected from the point scatterer are equal in amplitude so that sharp fringes occur where there is constructive interference, and destructive interference yields net cancelation. The

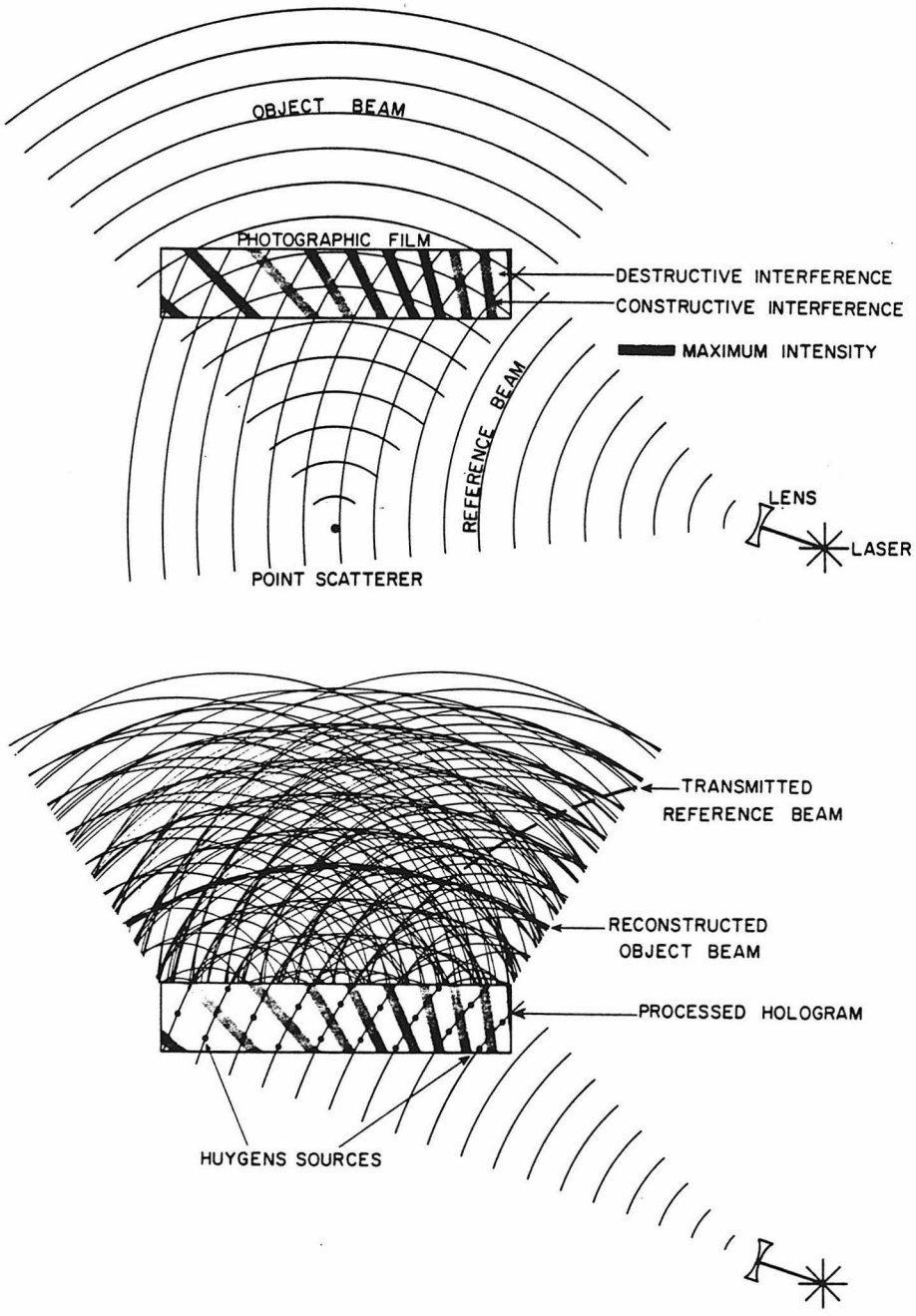

Figure A-3 Recording and reconstructing a hologram of a single point scatterer intuitively demonstrated by employing Huygen's principle. Crosshatched lines indicate decreased transmittance. Huygen's sources are placed in phase with the illuminating reference beam. Huygen's wavelets superimpose to reproduce the desired original object wavefront.

crosshatched lines indicate where constructive interference occurs. Upon processing these become the fringes, the most dense zones in the hologram.

The lower half of figure A-3 shows the processed film illuminated by the same reference beam used to generate it. Placing Huygen's sources in phase with the illuminating reference beam, between the dense zones and drawing the radiated wavelets from each source results in the complex of arcs above the film plane. Notice that these arcs systematically come into phase for two wavefields. The first is the transmitted reference beam, indicated on the figure. The second is a perfect rendition of the original object wave field except that it is shifted by one-half wavelength. This is the same shift discussed above, originating by using negative rather than positive photosensitive emulsion. It has no impact on the wavefield reconstruction.

If neither of these discussions satisfies your curiosity about how a hologram reconstructs a three-dimensional virtual image which is indistinguishable from the original wavefield radiated by a scene, pursue one of the two references given at the beginning of this appendix. Alternatively, find someone to demonstrate a holographically reconstructed wavefield. In any case, to understand the concepts of holographic interferometry discussed in Chapter 3, one need only accept that the holographic process does actually reproduce the optical wavefield radiated by the scene from which it was made.

One further property of holographic wavefront reconstruction is of interest. Notice that any subarea of the hologram is capable of

reproducing the entire scene. Unlike a photographic negative in which each region bears information related only to the corresponding part of the scene, each subarea of the hologram reproduces the entire scene. However, since each subregion only reproduces the scene as observed from its particular point of view, the information is not redundant.

REFERENCES

Ahrens, T. J., J. L. Jacoby, P. G. Bhuta (1975). A holographic instrument for in-situ stress measurement in deep boreholes, Trans. Am. Geophys. U., 56, 244.

Alexandrov, E. B. and A. M. Bonch-Bruevich (1967). Investigation of surface strains by the hologram technique, Soviet Phys. Tech. Phys., 12, 258-65.

Birch, F. (1966). Compressibility; elastic constants, in: S. P. Clark, Jr., ed., Handbook of Physical Constants, Memoir 97, The Geol. Soc. Amer. Inc., New York.

Brethauer, G. E., J. E. Magner, D. R. Miller (1980). Statistical evaluation of physical properties in Area 12, Nevada Test Site, using the USGS/DNA storage and retrieval system, U. S. Geol. Surv. Rept. USGS-474-309, 96 p., available only from U. S. Dept. of Commerce, NTIS, Springfield, VA 22161.

Broch, E. and B. Nilsen (1979). Comparison of calculated, measured and observed stresses of the Ortfjell open pit, Norway, in: Proc. 4th Int. Soc. Rock Mech., 2, 49-56.

Brown, G. M., R. M. Grant, G. W. Stroke (1969). Theory of holographic interferometry, J. Acoust. Soc. Amer., 45, 1166-79.

Cornwall, H. R. (1972). Geology and mineral deposits of southern Nye County, Nevada, Nevada Bureau of Mines and Geology, Bulletin, 77, 1-49.

Dhar, B. B., B. S. Verma, S. Ratan (1979). Fracture growth around openings in rock models and their effect on the design of stable openings, in: Proc. 4th Int. Congr. Rock Mech., Int. Soc. Rock Mech., 2, 99-104.

Ege, J. R., R. D. Carroll, J. E. Magner, D. R. Cunningham (1980). U. S. Geological Survey investigations in the U12n.03 drift, Rainier Mesa, Area 12, Nevada Test Site, U. S. Geol. Surv. Open File Report, 80-1074, 29 p.

Ellis, W. L. (1979). In situ stress investigations, in: U. S. Geological Survey investigations in connection with Mighty Epic event, U12n.10 tunnel, Nevada Test Site, U. S. Geol. Surv. Rept. USGS-474-228, 167-189, available only from U. S. Dept. of Commerce, NTIS, Springfield, VA 22161.

Ellis, W. L. and J. E. Magner (1980). Compilation of results of three-dimensional stress determinations made in Rainier and Aqueduct Mesas, Nevada Test Site, Nevada, U. S. Geol. Surv. Open File Report, 80-1098, 27 p.

Erf, R. K., ed. (1974). Holographic Nondestructive testing, Academic Press, Inc., New York, London.

Fairer, G. M. and D. R. Townsend (1979). Geologic investigations, in: U. S. Geological Survey investigations in connection with Mighty Epic event, U12n.10 tunnel, Nevada Test Site, U. S. Geol. Surv. Rept. USGS-474-228, 1-64, available only from U. S. Dept. of Commerce, NTIS, Springfield, VA 22161.

Friedman, M. (1972). Residual elastic strain in rocks, Tectonophysics, 15, 297-330.

Gibbons, A. B., E. N. Hinrichs, W. R. Hansen, R. W. Lemke (1963). Geology of the Rainier Mesa quadrangle, Nye County, Nevada, Map GQ-215, Scale 1:24,000, U. S. Geol. Surv., Washington, D. C. .

Hager, B. H. and R. J. O'Connell (1981). A simple global model of plate dynamics and mantle convection, J. Geophys. Res., 86, 4843-67.

Haimson, B. and C. Fairhurst (1970). In-situ stress determination at great depth by means of hydraulic fracturing, in: W. H. Somerton, ed. Rock Mechanics-Theory and Practice, Proc. 11th Symp. Rock Mech., AIME, New York, 559-84.

Haimson, B. C., J. LaComb, A. H. Jones, S. J. Green (1974). Deep stress measurements in tuff at the Nevada Test Site, In: Adv. Rock Mech. Proc. 3rd Congr. Int. Soc. Rock Mech., II-A, 557-62.

Haines, K. A. and B. P. Hildebrand (1966). Surface deformation measurements using the wavefront reconstruction technique, Appl. Opt., 5, 595-602.

Hansen, M. E. and R. J. Shaffer (1979). Some results from continuum mechanics analysis of the hydraulic fracturing process, in: Symp. on low-permeability gas reservoirs, Soc. Pet.Eng.-AIME, 297-306.

Hardy, M. P., C. M. St. John, G. Hocking (1979). Numerical modeling of the geomechanical response of a rock mass to a radioactive waste repository, in: Proc. 4th Int. Congr. Rock Mech., Int. Soc. Rock Mech., 1, 161-8.

Heflinger, L. O., R. F. Wuerker, H. Spetzler (1973). Thermal expansion coefficient measurement of diffusely reflecting samples by holographic interferometry, Rev. Sci. Instrum., 44, 629-33.

Hiltscher, R., J. Martna, L. Strindell (1979). The measurement of triaxial rock stresses in deep boreholes and the use of rock stress measurements in the design and construction of rock openings, in: Proc. 4th Int. Congr. Rock Mech., Int. Soc. Rock Mech., 2, 227-234.

Hiramatsu, Y. and Y. Oka (1962). Stress around a shaft or level excavated in ground with a three-dimensional stress state, Mem. Fac. Engng., Kyoto Univ., 24, 56-76.

Hood, M. (1979). Some results from a field investigation of thermo-mechanical loading of a rock mass when heater canisters are emplaced in the rock, in: Proc. 20th U. S. Symp. Rock Mech., Austin, Texas, 429-37.

Hooker, V. E., J. R. Aggson, D. L. Bickel (1974). Improvements in the three-component borehole deformation gage and overcoring techniques, U. S. Bur. Mines Rep. Invest. 7894, 29 p.

Hooker, V. E., J. R. Aggson, D. L. Bickel (1971). In situ determination of stresses in Rainier Mesa, Nevada Test Site, U. S. Bureau of Mines Report.

Hottman, C. E., J. H. Smith, W. R. Purcell (1979). Relationship among earth stresses, pore pressure, and drilling problems offshore Gulf of Alaska, J. Pet. Technol., 31, 1477-1484.

Hubbert, M. K. and D. G. Willis (1957). Mechanics of hydraulic fracturing, J. Pet. Technol., 9, 153-168.

Jaeger, J. C. and N. G. W. Cook (1979). Fundamentals of rock mechanics, 3rd edition, Chapman and Hall, London.

Kehle, R. O. (1964). The determination of tectonic stresses through analysis of hydraulic well fracturing, J. Geophys. Res., 69, 259-73.

Lee, F. T., D. R. Miller, T. C. Nichols, Jr. (1979). Relation of stresses in granite and gneiss near Mount Waldo, Maine, to structure, topography, and rockbursts, in: Proc. 20th U.S. Symp. Rock Mech., Austin, Texas, 663-673.

Leeman, E. R. (1969). The "doorstopper" and triaxial rock stress measuring instruments developed by the C. S. I. R., J. S. Afr. Inst. Min. Metall., 69, 305-39.

Leeman, E. R. and D. J. Hayes (1966). A technique for determining the complete state of stress in rock using a single borehole, Proc. 1st Congr. Int. Soc. Rock Mech., 2, 17-24.

Lehmann, M. (1970). Holography technique and practice, in Engineering uses of holography, E. R. Robertson, J. M. Harvey, eds., Cambridge University Press, London, New York.

Leith, E. N. and J. Upatnieks (1964). Wavefront reconstruction with diffused illumination and three-dimensional objects, J. Opt. Soc. Amer., 54, 1295-1301.

McGarr, A. and N. C. Gay (1978). State of stress in the earth's crust, Ann. Rev. Earth Planet. Sci., 6, 405-436.

Murphy, H. D., J. W. Tester, C. O. Grigsby, R. M. Potter (1981). Energy extraction from fractured geothermal reservoirs in low-permeability crystalline rock, J. Geophys. Res., 86, 7145-58.

Myrvang, A. M. (1979). Practical use of rock stress and deformation measurements in the Norwegian mining industry, in: Proc. 4th Int. Cong. Rock Mech., Int. Soc. Rock Mech., 2, 459-465.

Pincus, H. J., J. Handin, W. R. Judd, T. Engelder (1982). Rock mechanics research requirements for resource recovery, construction, and earthquake hazard reduction, Trans. Amer. Geophys. Union, 63, 545-47.

Pratt, H., T. Schrauf, W. Hustrulid, E. Simonson (1979). A large scale in-situ study to determine temperature, deformation and stress fields associated with heater experiments in crystalline rock, in: Proc. 4th Int. Congr. Rock Mech., Int. Soc. Rock Mech., 2, 539-44.

Raleigh, C. B., J. H. Healy, J. D. Bredehoeft (1972). Faulting and crustal stress at Rangely, Colorado, Amer. Geophys. Union, Geophys. Mono. Series, 16, 275-84.

Ranalli, G. (1975). Geotectonic relevance of rock-stress determinations, Tectonophysics, 29, 49-58.

Richardson, R. M., S. C. Solomon, N. H. Sleep (1979). Tectonic stress in the plates, Rev. Geophys. Space Phys., 17, 981-1019.

Richardson, R. M., S. C. Solomon, N. H. Sleep (1976). Intraplate stress as an indicator of plate tectonic driving forces, J. Geophys. Res., 81, 1847-56.

Robertson, E. R. and J. M. Harvey, eds. (1970). Engineering uses of holography, Cambridge University Press, London, New York.

Schmidt, J. L., T. J. Ahrens, D. R. Tomren, D. A. Evensen, P. G. Bhuta (1974). An optical instrument for in-situ stress measurement in rocks, TRW Report AT-SVD-TR-74-6.

Smith, M. B., G. B. Holman, C. R. Fast, R. J. Covlin (1978). The azimuth of deep, penetrating fractures in the Wattenberg field, J. Pet. Technol., 30, 185-193.

Solomon, S. C., R. M. Richardson, E. A. Bergman (1980). Tectonic stress: models and magnitudes, J. Geophys. Res., 85, 6086-92.

Timoshenko, S. P. and J. N. Goodier (1934). Theory of Elasticity, McGraw-Hill Book Co., New York.

Zoback, M. D. and S. H. Hickman (1982). In-situ study of the physical mechanisms controlling induced seismicity at Monticello Reservoir, South Carolina, J. Geophys. Res., 87, 6959-74.

Zoback, M. D. and D. D. Pollard (1978). Hydraulic fracture propagation and the interpretation of pressure-time records for in-situ stress determinations, in: Proc. 19th U. S. Symp. Rock Mech., Lake Tahoe, Calif., 14-22.

Zoback, M. L. and M. D. Zoback (1980). State of stress in the coterminous United States, J. Geophys. Res., 85, 6113-56.